Semi-automatic quantitative assessment of cancer-cell invasion *in vitro*: An image-processing approach

A thesis submitted in partial fulfilment of the requirements for the degree of

Doctor of Philosophy

May 2009

Samuel Hägglund

Department of Computing, Information Systems and Mathematics

Kingston University London

Kingston University London

Abstract

In western countries at least one third of the population develops cancer. The main cause of death in cancer patients is metastasis and there is no effective treatment for this complication. The situation can be improved by a better understanding of the cancer invasion process. In order to reveal new aspects of this dynamic process, a novel image-processing-based direct viewing cancer-cell invasion assay was developed and used with inverted wide-field microscopy. The combination of high-resolution 3D image-processing approaches with a custom-made flow chamber system enabled the quantification of the sarcoma-cell invasion process through a monolayer of endothelial cells *in vitro*.

The image processing entailed the separation of positive cell signal from background noise and blur, which are inherent in 3D wide-field microscopy. The preparation and cell signal segmentation of wide-field images prior to quantification featured stochastic as well as deterministic techniques. The stochastic approach was based on a Gaussian Mixture Model to separate noise and background signal characteristics from positive cell signal which performed well in conditions with high signal-to-noise ratios. The deterministic segmentation approach was based on linear diffusion and performed well despite low signal-to-noise ratios as it assessed the diffusion rates of cell signal over multiple convolutions.

The image-processing-based assay included the definition of two new parameters to quantify the invasion: Relative Invasion (RI) and Opening Rate of the Endothelial Monolayer ($OREM$). The first parameter RI measured the invasion as the percentage of sarcoma cell signal below the reconstructed monolayer surface. The second parameter $OREM$ evaluated the speed at which the sarcoma cells disassemble the monolayer in their strive to exit the flow channel.

This assay was applied to metastatic rat sarcoma cells where the cells invaded monolayers of rat endothelial cells. After adhesion, the sarcoma cells initially invaded significantly faster under flow conditions compared

to situations without shear stress. Later, however, the rate of invasion under flow decreased and the sarcoma cells without shear stress achieved significantly higher levels of invasion. These observations thus revealed the non-linear modulation of a tumour-cell invasion process by shear flow, demonstrating that tumour cells can respond to flow by enhancement of invasiveness in a similar way to white blood cells.

In summary, the newly developed direct viewing assay provides a quantitative image-processing-based approach to assessing cancer invasion dynamics, which should lead to a better understanding of the mechanisms involved in cancer invasion and metastasis.

Declaration of originality

I hereby declare that the research recorded in this thesis and the thesis itself was composed and originated entirely by myself in the Department of Computing, Information Systems and Mathematics at Kingston University London.

The extended Glycotech chamber (section 3.1), the Open chamber (3.2), cell culture (7.1.1) and cell labelling (7.1.2) were developed at the Light Microscopy Unit, Cancer Research UK London Research Institute.

Samuel Hägglund

Acknowledgements

Done at last... After some time I have finally completed this thesis. It has been a challenge which is now complete. I would like to thank my supervisors Andreas Hoppe and Daniel Zicha, both of whom I have learned a lot from. I thank you for your excellent guidance and supervision. Things would not have been possible without you.

Thanks also to Peter Jordan, Deborah Aubyn, Tamara Cavanna, Alastair Nicol and Colin Gray at CRUK for help with microscopes and other related things. Your generosity is appreciated. I thank Gordon Hunter for providing advice regarding Radial Basis Functions and Paul Kuo for proof reading, general comments and advice. I give thanks to Almighty God, the Lord Jesus Christ who has been my guardian and source of strength and hope during this time. Appreciation also to Beatrice who has sacrificially put up with me all this time.

The support of EPSRC (Grant GR/S34250/01) and *Cancer Research UK London Research Institute* is gratefully acknowledged.

Collaborating establishments

LONDON RESEARCH INSTITUTE
LINCOLN'S INN FIELDS

Light Microscopy Unit, Cancer Research UK London Research Institute, Lincoln's Inn Fields Laboratories, London WC2A 3PX, UK

List of publications

1. S. Hägglund, A. Hoppe, D. Zicha, "Direct viewing of cancer cell transmigration through monolayer of endothelial cells in a flow chamber with automatic detection of cancer cells," *16th International Microscopy Congress*, Sapporo, Japan, Sept, 2006
2. S. Hägglund, A. Hoppe, D. Aubyn, T. Cavanna, P. Jordan, and D. Zicha, "Novel shear flow assay provides evidence for non-linear modulation of cancer invasion," *Front Biosci*, vol. 14, pp. 3085–3093, 2009

Contents

1 Introduction **1**

1.1 The problem domain 1

1.2 Aims 2

1.3 Contribution 2

1.4 Thesis overview 3

2 Background **5**

2.1 Cancer-cell invasion 5

2.2 Assessment of cancer-cell invasion 11

2.3 Imaging modalities in microscopy 14

2.3.1 Point Spread Function 15

2.3.2 Wide-field Fluorescent Microscopy 16

2.3.3 Confocal microscopy 20

2.4 Image-processing techniques 22

2.4.1 Gaussian Mixture Models 22

2.4.2 Principal Components Analysis 26

2.4.3 Linear diffusion 29

2.4.4 Numerical interpolation 30

3 Direct viewing flow chamber system **32**

3.1 GlycoTech flow chamber system 32

3.2 The open chamber 35

3.3 Microscopy and image acquisition 37

3.3.1 Experimental set-up with the GlycoTech chamber system . . . 37

3.3.2 Acquisition with the Open chamber 41

3.4 Quantitative measurements 43

3.4.1 Relative Invasion (RI) 43

3.4.2 Opening Rate of the Endothelial Monolayer 46
3.4.3 Relative spreading 49

4 Surface reconstruction of endothelial monolayers 51
4.1 Finding the upper surface 52
4.1.1 Maximum intensity 52
4.1.2 Maximum gradient 55
4.1.3 Correlation 58
4.2 Identification of unreliable monolayer regions 59
4.2.1 Gaussian Mixture Model 63
4.2.2 Principal Components Analysis 68
4.2.3 Linear Diffusion 74
4.3 Surface interpolation 79
4.3.1 Least-squares fitting 81
4.3.2 Image inpainting 83
4.3.3 Radial basis function for surface interpolation 88

5 Image segmentation of sarcoma cells 92
5.1 Histogram-based segmentation 94
5.2 Diffusion-based segmentation 96
5.2.1 Linear diffusion applied to tumour cells 97
5.2.2 Thresholding diffusion rates 98

6 Validation of image-processing procedures 105
6.1 Validation data set 106
6.2 Validation of the recovery of the upper surface using maximum gradient 109
6.3 Validation of surface interpolation 117
6.4 Validation of tumour-cell image segmentation 119
6.5 Validation of Relative Invasion parameter 126

7 Experimental results 128
7.1 Experimental set-up 129
7.1.1 Cell culture 129
7.1.2 Cell labelling 130
7.2 Results 132
7.2.1 Novel flow chamber assay with image-processing-based quantitation 132

7.2.2 Metastatic sarcoma cells invade the monolayer of endothelial cells by creating openings between endothelial cells while non-metastatic sarcoma cells do not 133
7.2.3 Non-linear invasion response to shear flow 136

8 Conclusion and future work **146**
8.1 Summary of achievements 146
8.2 Discussion 148
8.3 Future work 150
8.4 Final words 152

References **169**

List of Figures

2.1 **Diagram of the metastatic cascade illustrating the importance of active cell migration through the endothelium.** A subset of tumour cells leaves the primary tumour (A) and intravasates (B) into the blood circulation system (C). Some of those cells adhere to the vessel wall at a remote site and extravasate (D) into the surrounding tissue. Proliferation occurs once the transmigration through the endothelial cells is complete and forms the basis of a secondary tumour metastasis (E). 6

2.2 **Example of an XZ-projection of an acquired Point Spread Function (PSF).** A single point influences its neighbouring points in a manner described by the PSF. The surrounding voxels are affected, mainly in Z-direction but also in XY. This behaviour is due to asymmetry of the optics. A black pixel in the image represents no influence from the point source and white represents heavy influence. **(a)** XZ-projection of an acquired PSF **(b)** XZ-projection of a wide-field image stack 15

2.3 **Fluorescence imaging system set-up.** The fluorescence microscope consists of a lamp and an excitation filter that only allows the specific excitation wavelength to pass through to the dichroic mirror, which has the ability to reflect a certain wavelength and be transparent for another. This ability grants only the emitting light access through the mirror while the exciting light is mirrored towards the specimen. The objective lens focuses the light onto the specimen and the eyepiece lens focuses the light towards the detector. 18

2.4 **Diagram illustrating the principles of confocal microscopy.** A light source emits light which travels through an aperture (light source aperture). The light is reflected by a dichroic mirror onto the specimen. The fluorescently labelled cells respond by emitting light different from the excitation wavelength. A pinhole in front of the detector blocks out-of-focus light and detects the in-focus. A confocal microscope exhibits similar layout to a wide-field microscope with a few exceptions. Two of those are the light source aperture and the detector aperture which only allow in-focus light to progress through the system. 20

2.5 **Description of the EM algorithm.** The algorithm alternates between the E-step and the M-step for some iterations. The average is recalculated during every iteration and will eventually converge. In the E-step, the probability $N(x_i; a_k, S_k)$ is calculated using Eq. 2.5 given the parameters for a particular cluster. Repeat the E-step for all pixels and every cluster. Then, using the M-step, recalculate new weights, average and covariance for each cluster. Repeat the E-step and M-step until the number of repetitions has been reached. 24

2.6 **The eigenvalues of the corresponding Principal Components.** The eigenvalues represent the amount of variation contained in each PC. The largest eigenvalue represents the first PC and, subsequently, the first PC contains most of the variation in the image. Many PCs do not contribute much to the information in the image and a reduction can then be made by discarding PCs with little variation (i.e. small eigenvalues). Choosing the number of PCs is then the overall problem. 28

2.7 **Linear interpolation between two points.** Two known data points are chosen (A and B). A line which runs through these points is fitted to them. The value of the intermediate point C is obtained by finding $f(x)$ of the line at the position C. 31

3.1 **The GlycoTech flow chamber system.** The system consists of a circular flow chamber (GlycoTech Corp., MD, USA) which we have fitted into a stainless-steel enclosure to enhance stability and allow ease of use. The bottom of the chamber is sealed by a 32 mm diameter coverslip with a monolayer of rat brain endothelial cells (RBE4). . . . 34

3.2 **Schematic drawing of the open flow chamber.** The custom-made Nylon insert fits into a MatTek dish with a confluent monolayer of endothelial cells (EC). The cells are exposed to the shear stress in an oval aperture in the centre of the insert. This central aperture is open and allows initial introduction of tumour cells (TC). The entire flow chamber is presented in 3D (A) and as top-view/cross-section (B). Detail view (C) depicts the vertical inlet tube, which is connected to the central aperture by a channel cut into the base of the insert using a milling machine. A symmetrical channel connects the opposite end of the central aperture to the outlet tube. On the outside, the outlet is connected to the inlet by flexible tubing going through a peristaltic pump. Measurement units are in mm. 36

3.3 **Flow chart of an image-acquisition protocol used with the Extended GlycoTech chamber.** The protocol is designed to capture cancer cells that adhere and settle down to the monolayer during flow conditions. A list of predefined positions was stored in the Metamorph acquisition system. The positions were visited consecutively and, for each position, a single image of the DiO green channel was acquired. A pause of five sec was ordained and a second image was obtained of the same position. Both of these images were thresholded at intensity level 1000 for 12-bit images. The AND operator applied to these two captures resulted in a binary image suitable for detecting adherent cancer cells. In the case of adherent cells, the binary image contains segments of the stationary cell whilst a non-stationary cell produces an empty image. A cell was considered as stationary if the number of segmented pixels was > 0.2 % of the number of pixels in an image (typically 696×520). 41

3.4 **Graphical explanation of Relative Invasion (RI).** Relative Invasion can simplistically be described as the amount of tumour-cell signal (shown in green) below the EC monolayer (in red) in relation to the tumour-cell signal throughout the cell height. **(a)** An artificially and intentionally created overlay depicted as a dotted line was added as a replacement for missing EC values. **(b)** 3D rendering of the invasion. 43

3.5 **Flowchart of the calculations of Relative Invasion** (RI). The z-levels of the upper surface of a stack of endothelial monolayers were estimated. Some of the regions were weakly labelled or were missing cell signal and produced unreliable readings. The z-levels in these areas were replaced by an artificially created overlay and the relative invasion was then quantified as the amount of sarcoma cell signal below the upper surface of the monolayer in relation to the total cell signal. 45

3.6 **Illustration of the calculations of OREM.** The minimum projection of monolayers (shown in red) at each time point was obtained to provide evidence for early openings. The estimation of the opening rate was performed in a predefined window, shown in green, of 4×4 μm (21×21 pixels) at a fixed location during the entire observation period. The position of the window was selected where the opening between 0-30 min was the largest. $OREM$ was then calculated as the difference in monolayer signal within the window between 0-30 min but normalised over the observation period. A difference in cell signal can be seen inside the window between the mentioned time points. The normalisation, the predefined window size and the fixed location of the window made the parameter comparable between experiments. The intensity of the monolayers was adjusted for visualisation purposes. . 47

3.7 **Flowchart of the steps to obtain OREM.** $OREM$ can be seen as a measurement of how quickly the signal disappeared in a small defined, fixed region, typically $4 \times 4\mu$m. The region (window) was applied to the minimum projection of a monolayer stack. The normalised rate at which the signal faded between 0 and 30 min constituted the parameter $OREM$. Because the rate is normalised using the maximum opening over all time points it is possible to compare the rate between different cells and experiments. 48

3.8 **Example of ellipses which defined Relative Spreading.** The area of an ellipse fitted to the segmented pixels was calculated for each time point. This area was divided by the area of the reference fit which was calculated as the area of the ellipse fitted to all the segmented pixels over all time points. Relative spreading can thus have a quantity >1 because it was possible that the reference fit was smaller due to a higher amount of segmented pixels. **(a)** An ellipse fitted to the segmented pixels found at a single time point. **(b)** A reference fit for a cell. 50

4.1 **Examples of intensity curves of strongly and weakly labelled areas.** The intensities for two different <x,y> positions were plotted as connected data points over z. The strongly labelled position exhibited a sharp peak in intensity around the surface z-location. The weakly labelled position portrayed high intensity values towards the start and end of the curve and low in-between. The fluorescence in this position was low and therefore most of the intensity values stem from blur originating at its neighbours. The z-level of the minimum intensity indicated where those were in focus and the z-level of the maximum intensity indicated where most of those were out of focus rather than the surface level. The visually estimated z-levels were subjectively found by manually scanning through the image stack for the z-level which contained the sharpest region for each position. **(a)** shows the intensity curve for a strongly labelled position. The z-level of the maximum intensity was close to the visually estimated level (z = 6 and 4 respectively). **(b)** shows the intensity curve for a weakly labelled position. The manual surface estimation and the z-level of the maximum intensity were different (z = 6 and 19 respectively). This was because of the interference of blur from neighbouring voxels. . . 54

4.2 **Examples of gradient curves obtained from a blurred stack.** The average gradient value using the Sobel operator was calculated for each plane and plotted as connected data points. The maximum gradient value indicated at which z-level the focus was located. A z-level of 1 represents the top of the stack. The three figures together indicate that the curve needed to be in a local context and filtered with an average filter in order to produce an accurate estimation. **(a)** represents a gradient curve where each data point represents the average gradient value for a plane. The in-focus plane was found at z=35 (maximum gradient value) and the coverslip was found at the position where the slope was steepest, indicated by the dashed line (z=38). **(b)** a raw gradient curve without smoothing for a single pixel over z. Dotted line represents the focus position at z=36. This curve did not undergo any smoothing to remove noise. The peak at z-level = 31 was due to noise. **(c)** a gradient curve filtered with an average kernel of 11×11 pixels. The noise was now suppressed and the accurate surface location was revealed as the z-level where the gradient had its maximum at z=40. Manual inspection confirmed this surface position. 57

4.3 **Example of graphs with correlation values obtained from gradient images acquired with a confocal and a wide-field microscope.** The correlation coefficient was calculated between two 11 × 11 pixel windows of consecutive z-planes. The Sobel gradient was calculated prior to obtaining the correlation values. **(a)** Correlation values obtained from a confocal stack. The correlation between two windows expressed a sharp peak at the in-focus position and low values towards the sides. **(b)** Correlation values obtained from a confocal stack, convolved with a PSF to simulate wide-field conditions. The correlation between two windows was believed to increase to a sharp peak at the in-focus position, which was not the case. Instead, the high values were contained in a broader spectrum of z-planes where the sharp peak was smoothed by the blur. 59

4.4 **Example of segmentations of a minimum projection obtained from a stack of an endothelial monolayer using thresholding.** The minimum projection emphasises the dark areas, which highlighted areas with low intensity. **(a)** Minimum projection. Arrows indicate examples of regions with low intensity which may cause problems. **(b)** Segmented result of (a) after applying the manually obtained threshold. **(c)** Histogram of the minimum projection. Arrows indicate the three different stages (modes) of brightness seen from left to right in (a). Dashed lines represent the manually selected threshold used to produce (b) and (d) respectively. **(d)** Segmented result after obtaining a threshold using a standard method (Otsu [1]). 62

4.5 **Histograms of a stack with no cells (only background noise) obtained with a wide-field microscope.** The noise in a microscope is usually described as being Poisson distributed [2]. Because a point in a wide-field system is influenced by every other point through diffraction and interference, the Central Limit Theorem [3] approximates the distribution to a Gaussian distribution. The stack contained 520×696 pixels over 76 z-slices (although the histograms shown represent a volume of 11×11×11), with resolution 0.2×0.2×0.2μm/px. Exposure time: 60 ms, binning 2×2. **(a)** The intensity distribution of a sub-volume of the acquired noise. **(b)** The gradient distribution of a sub-volume of the acquired noise. 64

4.6 **Histogram of a stack of size 11×11×11 pixels containing the difference between the gradient values of a stack of a monolayer and a filtered version of itself.** The gradient for each plane was calculated (denoted by G in Eq. 4.2). An average filter of 11×11 pixels was applied on a plane-by-plane basis to suppress the noise (G_f in Eq. 4.3). The difference between the two ($G - G_f$) is displayed as a histogram which represents the noise plus some residual gradient signal. The histogram in (b) has a wider distribution because the residual signal located in the upper segment of the histogram was stronger. **(a)** Histogram of an unreliable area. **(b)** Histogram of signal (reliable area). 66

4.7 **Histogram with the two mixtures superimposed.** The difference was separated into two clusters using the EM algorithm [4]. A window was classified as unreliable if the variance of the cluster with the lowest mean was < the variance of the measured noise. **(a)** Histogram of an unreliable region. **(b)** Histogram of a more reliable region. 68

4.8 **Example of segmentation of unreliable regions in a monolayer using GMM.** The segmentation was based on separating the Gaussian-like noise from the signal. The noise was obtained by calculating the difference between the original intensity stack and a filtered version of itself. The EM algorithm was applied on 11×11×11 pixel substacks with two classes: signal and noise sourced from the difference. The variance of the separated noise (i.e. the variance of the cluster with the lowest mean) is compared to the variance of an empty stack containing noise only (reference sample). A region was classified as unreliable if the variance of the separated noise < variance of the measured. The size of the original stack containing cell signal was 520×696×101 voxels with resolution 0.2×0.2×0.2μm acquired five hours into the experiment. **a)** Original in-focus plane. **b)** Segmented result. The white areas represent unreliable regions and are superimposed on the in-focus plane. The white arrow indicates an invaded area but correctly segmented as cell surface. This region was actually covered but invading TC forced the surface outside the in-focus plane. 69

4.9 **Segmentation of endothelial monolayer using Principal Components Analysis (PCA).** Eigenimages of endothelial monolayer are obtained through PCA and the hypothesis is that cell signal values are correlated and will therefore occupy the same range of PCs. **(a)** Minimum-intensity projection. **(b)** Eigenimage reconstructed by using the first 16 PCs only representing 99.6% of the information. **(c)** Segmented result of (b). The threshold was manually set to 0.25. **(d)** Histogram of the eigenimage shown in (b). The dashed line represents the subjectively and manually selected threshold of (b) to obtain the segmented result in (c). Threshold was set to 0.25. 70

4.10 **Example of segmentation of a monolayer using PCA.** The minimum projection was transformed into an eigenimage using the first 16 PCs, representing 99.7% of the information. The cell signal would occupy the first few PCs because of its correlation and noise would occupy latter PCs. However, blur affected the distribution of intensity values and caused the segmentation values to fail. The area in the centre of (a) is an example of where certain regions were falsely classified as reliable because the intensities were similar to cell signal. **(a)** Minimum projection of a stack of endothelial monolayers. **(b)** The eigenimage of (a) using the first 16 PCs. **(c)** Segmented result of (b) while applying the threshold of 0.25. Dashed line indicates a manually selected outline to represent the corresponding outline in (a). **(d)** Histogram of the eigenimage. The threshold was subjectively chosen to 0.25 which produced (c). 72

4.11 **The convolved images after different numbers of iterations.** The image (696×520 pixels) is convolved with a Gaussian kernel of σ=0.5 a number of times. The image gets more diffused with the number of iterations. The changes between 500 and 1000 iterations are small, which is why 500 is considered to diffuse the information enough to distinguish between the trustworthy and not reliable areas. 75

4.12 **The segmented monolayer after convolution with a Gaussian kernel iteratively.** The minimum projection (696×520 pixels) of the monolayer was convolved with a Gaussian kernel of 11×11 pixels 500 times. The convolution revealed the trends and behaviour of each pixel over the iterations. The image intensities will tend to reach the average if the iterations reach infinity. A pixel is selected as background if its diffusion rate is negative at any point in time. This implies that it is less than the average. The number of iterations was subjectively chosen to simulate infinity. **(a)** Minimum projection over z of a monolayer. **(b)** Segmented result. 76

4.13 **Comparison of segmentations of a minimum projection of an endothelial monolayer stack which PCA did not manage to segment.** The minimum projection over Z was obtained from a stack of endothelial cells. The minimum projection was convolved with a Gaussian kernel 500 times and the rate at which the cell signal diffused was investigated. Linear diffusion managed to segment the large unreliable area in the centre, which PCA did not. The successful segmentation was due to the fact that the behaviour of the cell signals over the iterations was used and not intensity itself. A segmentation using Otsu [1] was included as a comparison and the segmentation performed well due to the fairly uniform labelling. **(a)** Minimum projection **(b)** Segmented result using Linear diffusion **(c)** Segmented result using PCA with 16 PCs and the normalised eigenimage which was thresholded at 0.25 **(d)** Segmented result using Otsu [1]. 77

4.14 **Illustration of interpolation over a sarcoma-induced opening.** Sarcoma cells created openings within the monolayer in attempts to exit the flow channel. These openings did not contain enough signal to produce sufficient gradient values. *RI* measured the amount of cell signal below the monolayer in relation to the total. In order to prepare the surface for such a procedure, the opening was replaced by an interpolated overlay. **(a)** A surface with an opening caused by invading sarcoma cells. **(b)** The surface was restored by interpolating over the opening. 80

4.15 **Illustration of the disadvantage of Inpainting in the context of surface interpolation.** The main concept of inpainting is to propagate the gap with values from the boundary. The inpainting techniques gave rise to unrealistic surface reconstructions due to the fact that they inpaint in the direction of the gradient. The merging between the two sides may create very sharp transitions, which is not a good representation of the endothelial monolayer. **(a)** Illustration of a gap induced by a TC. **(b)** The inpainting algorithm tries to inpaint in the direction of the gradient which may cause sharp transition when the two edges of the surface merge. 86

5.1 **Example of a manual segmentation of a sarcoma cell.** The classification was made subjectively and the thresholds were set to include the maximum amount of cell signal and minimise the out-of-focus blur. **(a)** Maximum projections of raw intensity image stacks. **(b)** The thresholded result. **(c)** Histogram of the maximum projection. The dashed line indicates the chosen threshold (3200). 93

5.2 **Example of a segmentation of a sarcoma cell using Otsu's method.** **(a)** Maximum projection of a raw intensity image stack. **(b)** The thresholded result. **(c)** Histogram of the maximum projection. The dashed line indicates the calculated threshold (1285). 95

5.3 **Segmentation of a maximum projection of cells using linear diffusion.** The maximum projection image was convolved with a Gaussian kernel for t iterations (in this case t was subjectively chosen to 20). The projections over the t iterations containing the minimum value of the diffusion rate for each $< x, y >$ over the iterations were obtained. All positive rates were discarded as those represented blur and noise. For calculation purposes, though, the negative rates were inverted. To find a threshold, a normalised histogram of the diffusion rates was created and the normalised number of pixels below a threshold was plotted against the normalised sum of diffusion rates above. The threshold was selected where the number of pixels was greater than the sum of diffusion rates which in practice represented the nearest integer. The number of pixels below a diffusion rate (solid line) starts at 0.5 because 50% of the values have a maximum diffusion rate of zero (rounded to the nearest integer). **(a)** The maximum projection of the diffusion rates after 20 iterations. **(b)** The segmented result on the basis of thresholding diffusion rates. **(c)** A threshold for the diffusion rates was found by plotting the normalised number of rates below consecutive thresholds against the normalised sum of diffusion rates above the potential threshold. The threshold was chosen at the crossing of the two curves, where number of rates > the integrated sum (see inset). The vertical dashed line indicates the selected threshold which in practice is rounded to the nearest integer (in this instance a value of 3). 101

5.4 **Convolutions of a maximum projection of an intensity image obtained from a 3D wide-field stack representing a sarcoma cell.** The maximum projection image was convolved with a Gaussian kernel of 11 × 11 pixels (2 × 2 μm). Bright pixels in the maximum projection exhibited a higher diffusion rate compared to background/blur with lower diffusion rate (represented as dark values) after n iterations. However, a high number of iterations merged some features (see 100 iterations) into larger objects. This was an unwanted property and 20 iterations were found to be suitable. Values are inverted for visualisation purposes. Field size is 27 × 27 μm. 102

5.5 **Segmentation results of a maximum projection image containing a sarcoma cell based on linear diffusion and thresholding for a selection of iterations.** The maximum projection obtained from a 3D stack of images was convolved with a Gaussian kernel of 11 × 11 pixels (2 × 2 μm) n number of times (σ=0.5). The rate at which each pixel diffused was investigated and formed the basis for segmentation as cell signal values were different and diffused more quickly than blur and background. The maximum rate for each <x,y> was represented as intensity in an image. A threshold for this image was selected at the intensity level where the normalised number of pixels below a threshold candidate was greater than the normalised integrated intensity above (see Fig. 5.3(c)). The segmentation results look similar because the maximum values over the iterations are chosen which were the same in each case. Therefore, 20 iterations were chosen. Each result was also filtered with a 5 × 5 median filter to remove noise. Field size is 27 × 27 μm. 103

6.1 **Procedure of the creation of a validation data set for the maximum gradient.** The validation of the maximum gradient featured a data set based on a confocal stack. A confocal stack of a monolayer with fixed specimen was acquired with resolution <x,y,z> = 0.07×0.07×0.2 μm/pixel. The resolution of this stack was adjusted to match the resolution of a PSF (0.1×0.1×0.2). These were convolved and the result was a new stack which resembled wide-field conditions. The new convolved stack contained images with <0.33×0.33×0.2 > μm because the <x,y> resolution of the two stacks was decreased by 1/3 prior to convolution to reduce computation time. The maximum gradient was applied on both the adjusted and the blurred confocal stack where the confocal acted as a reference sample, i.e. ground truth. The depth maps obtained as a result were then compared. 108

6.2 **Flow chart of the construction of the sarcoma-cell validation data set.** Boxes of size 4×4×12 pixels with intensity of 1 were inserted into an empty stack at random <x,y> positions. This stack was convolved with a normalised PSF where the convolved result simulated wide-field conditions. The number of boxes in each stack was selected randomly but the minimum number of boxes was set to three. Noise at randomly selected locations was sampled from a stack acquired with a wide-field microscope containing no cells. The noise was added to the original stack with binary boxes and to the convolved stack after the convolution procedure (2a and 2b). The stacks were normalised between 0-100 so that a comparison could be made. Manual inspection of stacks with sarcoma cells suggested the intensity for cell signal should have a value of around 100. The segmentation procedure was applied to the maximum projections of the wide-field stacks and produced a binary mask. The binary mask (marked 3) was multiplied with the maximum projection of the intensity (marked 2b). The maximum projection of the stack with binary boxes (marked with 1) was multiplied with the maximum projection of the same stack but with noise added (marked 2a). This ensured that non-signal values were excluded. Correlation was then calculated on the remaining signal values. 110

6.3 **Reconstructed surface using maximum gradient from a stack obtained with confocal microscopy containing a monolayer of endothelial cells.** The surface of the monolayer was reconstructed by finding the z-position of the maximum axial gradient for each $< x, y >$. The image stack contained image planes of 73×73 μm at 50 different z-levels (0.33×0.33×0.2 μm /pixel). The white border line indicates the border of the sarcoma cell. 111

6.4 **Reconstructed surface using maximum gradient from an intentionally blurred confocal stack containing a monolayer of endothelial cells.** A stack acquired with confocal microscopy was blurred with an acquired PSF. The surface of the monolayer was reconstructed by finding the z-position of the maximum axial gradient for each $< x, y >$. The image stack of the source contained image planes of 73×73 μm at 50 different z-levels (0.33×0.33×0.2 μm /pixel). The white border line indicates the border of the sarcoma cell. 112

6.5 **Error map of depth values obtained with the maximum gradient technique between a confocal stack and a convolved version of itself.** A stack acquired with confocal microscopy was blurred with a measured PSF to enable wide-field properties. The maximum gradient was applied in both instances and the error is displayed as a map. Manual assessment determined the thickness of the monolayer to 8 z-levels (1.6 μm). Mean value of absolute difference: 3.16 slices (0.63 μm), standard deviation: 4.4 (0.63±0.88 μm). Manual assessment determined the thickness of the monolayer to 8 z-levels (1.6 μm). 113

6.6 **Graph of depth values of a cross-section obtained from a stack.** A confocal stack was convolved with a PSF to simulate a wide-field acquisition and depth values were obtained using the maximum gradient over z. The units are in relation to the coverslip. **(a)** Depth values are plotted over a cross-section. Dashed line indicates values from the confocal stack and solid line represents the convolved version where the values from the confocal stack then acted as a reference. The two versions seem to correlate well (Spearman correlation, r=0.86, p-value < 0.0001). **(b)** Image of the in-focus plane of the confocal stack. The white line in the centre indicates the location of the cross-section. **(c)** shows a profile plot of the same position but both stacks have been smoothed with an 11×11 prior to obtaining the maximum gradient. . 114

6.7 **Surface rendering of confocal stacks restored using the maximum gradient.** The maximum gradient technique applied for each <x,y> over z to produce depth values. The depth values are presented as a 3D surface volume and both seem to agree well. The images were rendered using Volocity (Improvision, UK). **(a)** The original confocal surface rendering. **(b)** Surface rendering from a restoration of a blurred confocal stack. 115

6.8 **Colocalised rendered images of a confocal stack and its blurred counterpart.** Surface values obtained using the maximum gradient from a confocal stack and the corresponding blurred stack were loaded into volume-rendering software and colocalised images were created. Yellow indicates areas where the depth values from the confocal and the blurred version were exactly the same. Green represents areas where the confocal surface values were higher and red represents areas where surface values obtained from the blurred stack were higher. The surfaces represent ±3 z-levels around the estimated value. The values are not always identical because the surface values fluctuate (see Fig. 6.6). Images rendered using Imaris. **(a)** Top view. **(b)** Bottom view. 116

6.9 **Examples of maximum-projection images and their respective masks.** Boxes were inserted into an empty stack to mimic mitochondria and form some kind of ground truth. This stack was convolved with a PSF to resemble sarcoma cells obtained with a wide-field microscope. The segmentation was applied on maximum-projection images of the convolved version and resulted in a binary mask. The mask related to the original stack was given by the maximum projection of the stack prior to convolution. The two binary masks were multiplied with their maximum-intensity projections respectively. The correlation between the sum of the intensities before and after convolution was calculated as well as the correlation between the number of segmented pixels in the masks. Noise was added to both stacks after the convolution. **(a)** Maximum-intensity projection of the original stack with added noise. **(b)** Maximum-intensity projection of the convolved stack with added noise. **(c)** The binary mask of the original. This is also the maximum projection prior to convolution. **(d)** The binary mask produced by the segmentation of the maximum projection of the convolved stack. 120

6.10 **Example of a segmentation result of the validation of tumour-cell segmentation.** Boxes of size (4×4×12) were inserted into an empty stack at random <x,y> positions. This stack was convolved with a PSF obtained from a wide-field microscope which used the same equipment as the actual experiments. The resulting stack was segmented using Linear diffusion (section 5.2.1). The segmented image acted as a mask and was multiplied with the maximum projection of the convolved stack to remove out-of-focus blur. To evaluate the result of the removal, the correlation coefficient between the intensity of the original unconvolved maximum projection and the intensity of this new image was compared. The segmentation procedure slightly altered the location of the boxes due to the asymmetric shape of the PSF. However, the intensities and the number of segmented pixels in the original maximum projection and the convolved seemed to correlate well (see Table 6.3).**(a)** shows the maximum projection of the original image (i.e. the reference) prior to convolution. **(b)** Maximum projection of the convolved stack. **(c)** Segmented result. **(d)** The boundary of the original boxes (green) superimposed on the segmented result. 125

6.11 **Example of manual fitting of an ellipse to the intensity in a z-plane of a TC stack.** An ellipse was fitted manually to the intensity of each z-plane. The area of each z-plane represented the volume of a cell which was used to quantify the invasion and as a validation of the *RI*. The manual *RI* was quantified as the volume below the surface in relation to the entire cell volume. 126

7.1 **Example of an image of an endothelial monolayer at the in-focus position of a stack labelled with the described technique.** The described procedure for surface labelling provided excellent surface definition and prolonged photostability. 130

7.2 **Images of a sarcoma cell invading a monolayer of endothelial cells without flow where the sarcoma cell had invaded almost completely underneath the surface of the monolayer.** The images present renderings of a z-stack of images (field size 73μm×73μm) acquired from 50 z-levels at 0.2 μm separation by a laser-scanning confocal microscope LSM 510 (Carl Zeiss MicroImaging GmbH, Jena, Germany). Endothelial cells labelled with CellTracker Orange CMTMR were imaged using a 543 nm line of a HeNe laser and are represented in red, and the sarcoma cell labelled with green DiO was imaged using a 488 nm line of an Argon laser and is represented in green. (A) Shows the isosurface rendering of the sarcoma cell. (B) presents the maximum-intensity projection of the endothelial monolayer where the individual cells and openings between them can be identified. (C) and (D) show the top view and the bottom view of combined isosurfaces. The images were rendered using Imaris (Bitplane AG, Switzerland). 134

7.3 **Histograms of sarcoma-cell induced Opening Rate of the Endothelial Monolayer (OREM) between 0 and 30 min in conditions without and with flow.** The control cells without shear flow showed a decreasing trend of the number of cells with increasing opening rate (Pearson correlation P value < 0.01). The sarcoma cells exposed to flow showed an increasing trend of the number of cells with increasing opening rate with the exception of a small subset of late-responding cells which did not exhibit any activity during this initial period. The statistical significance of the difference between the two groups is presented in Table 7.1. The total number of evaluated cells was 104 without flow and 112 under flow. 135

7.4 **Relative Invasion (RI) of invading sarcoma cells without and with shear flow plotted over a 90 min observation period.** *RI* measures the ratio of the volume of an invading sarcoma cell below the upper monolayer surface and the total volume of the sarcoma cell. RI values are plotted as data points connected by solid lines (no shear flow) and dashed lines (flow with shear stress). Control sarcoma cells without shear flow exhibited lower invasion in the first 45 min compared to sarcoma cells exposed to shear flow. The significant difference of the invasion rate at this early stage is described in Table 7.1. Later on, the situation reversed and the control cells showed a significantly higher level of invasion in comparison to the sarcoma cells exposed to shear flow. Graph represents data from nine control cells without flow and 13 cells under flow conditions. Error bars represent standard errors of the mean. 136

7.5 **Images illustrating sarcoma cells invading monolayers of endothelial cells.** Endothelial cells labelled with CellTracker Orange CMTMR, using the protocol described in 7.1.2, are represented in red and sarcoma cells labelled with Vybrant DiO solution are represented in green. The Vybrant DiO dye produces punctate staining throughout the cytosol. (A) presents images from a time-lapse recording of a sarcoma cell invading a monolayer of endothelial cells. Images of the endothelial cells show minimum z-projections and images of the sarcoma cell show maximum z-projections of optical sections obtained between the surface of the monolayer and the substrate. The invasion was monitored over 90 min and the sarcoma cell was found to partially extend under the monolayer after 30 min. Scale bar represents 5 μm. (B) and (C) show 3D-reconstructions, at early and late stages of invasion respectively, of an adhering sarcoma cell (left) and an invading sarcoma cell (right) interacting with a monolayer of endothelial cells. The raw data were acquired as stacks of wide-field images. The surface of the endothelial cells was reconstructed by locating the in-focus level at each <x,y> position. The images of the sarcoma cells were processed by high-pass filtering and soft thresholded to reduce out-of-focus blur. The images were pre-processed by custom-developed software in MATLAB and the resulting data were presented using Volocity (Improvision Inc) 141

7.6 **Average area of the fitted ellipses above and below the monolayer.** Ellipses were fitted to the segmented pixels above and below the monolayer in MATLAB [5] and the area of these was computed. The experiments without flow expressed a higher rate of spreading both above and below the monolayer in the earlier stages. After a while, the situation reversed and the cells exposed to flow could not sustain the pace of spreading. Note that the actual area cannot be compared because the performance of the labelling technique may vary between cells. 142

7.7 **Average number of segmented pixels of a sarcoma cell over a 90-min time period.** The numbers of segmented pixels from the two experimental situations (control and flow) are different. Situations with flow have a higher amount compared to control. The amount of labelling substances attached to the mitochondria was different and therefore produced different segmentation results. The error bars represent the standard errors of the mean (Eq. 7.1). 143

7.8 **Relative spreading of sarcoma cells below the monolayer without and with flow.** Ellipses were fitted to the segmented projections above and below the surface. A reference fit was obtained for each cell so that different cells could be compared. The reference samples for a cell which formed the underlying data comprised the entire set of segmented pixels in all time points and resulted in an image with every segmented pixel during the entire observation period for a cell. An ellipse was fitted to this set and acted as a reference. The fitted ellipse of the segmented pixels for each time point was then divided by the reference. One detail to note is that the Relative Spreading may have a value > 1 because the area of the reference ellipse can be smaller than the area of each time point. Error bars represent standard error of the mean. 144

7.9 **Ratio of major/minor axis below the monolayer.** The spreading of cells, described by the major and minor axis, was investigated below the monolayer surface. An ellipse was fitted to all segmented pixels for a cell during all time points and used as a reference. The major or the minor axis for each individual cell was divided by the respective axis of the reference fit (x/x_{ref},y/y_{ref}) in two experimental situations to depict the shape changes that may have occurred. A value of one indicates that the shape of the reference fit and the individual cells are the same. The value at the first acquisition time point (0 min) is zero because sarcoma cells were introduced after the first acquisition time point. The spreading patterns in control and flow experiments were similar. Error bars represent standard error of the mean. 145

Acronyms and abbreviations

bFGF	basic Fibroblast Growth Factor
CCD	Charge-Coupled Device
CMTMR	M 5-(and-6)-(((4-chloromethyl)benzoyl)amino) tetramethylrhodamine
DMSO	dimethyl sulfoxide
EC	Endothelial Cells
GMM	Gaussian Mixture Model
MEM	Minimal Essential Medium
OREM	Opening Rate of the Endothelial Monolayer
PC	Principal Component
PCA	Principal Components Analysis
PSF	Point Spread Function
RBF	Radial Basis Function
RES	Relative Spreading
RI	Relative Invasion
SVD	Singular Value Decomposition
TC	Tumour Cells

Nomenclature

$I(x, y, z)$	image intensity of sarcoma cell fluorescence in a voxel
$I_{minp}(\mathbf{x})$	minimum intensity projection image over z
$I_{diff}(\mathbf{x}, t)$	difference in intensity between two consecutive minimum z-projections t and t+1
$U(x, y)$	upper surface of the endothelial monolayer
Ω_C	a set of N positions <x,y> with signal in the z-projection of the entire image stack
Ω_I	a set of N positions <x,y> where the invading sarcoma cell is present in the z-projection

Chapter 1

Introduction

1.1 The problem domain

The spread of cancerous cells to a remote site that form secondary tumours, metastasis, is still the major problem for cancer patients since it is responsible for the majority of their deaths [6] and cancer has become one of the most common diseases in western countries. The process by which metastases form is referred to as the metastatic cascade [7]. In many cases of cancer, the metastatic cascade involves tumour cells spreading in the body through blood vessels. The metastatic cascade can then be described as a sequence of necessary events [8]. In this metastatic cascade, the tumour cells have to actively invade through endothelium twice (intravasation and extravasation). The invasion is therefore a very important aspect of the metastatic cascade [9].

Previously, the invasion has mostly been quantified subjectively by manual scoring and some of these studies were limited to static observation of the end result. Developing a direct-viewing protocol for objective evaluation of invasion would therefore provide additional insights.

1.2 Aims

We decided to explore additional aspects of the extravasation process *in vitro* by high-resolution 3D imaging combined with an image-processing-based quantitation of its dynamics. The aim is to develop a novel direct viewing flow assay and apply it to an investigation of metastatic rat sarcoma cells invading monolayers of rat brain endothelial cells *in vitro* to objectively quantify the invasion in situations without and with shear forces.

1.3 Contribution

Objective evaluation of the cancer-cell invasion has attracted little interest, partly because wide-field microscopy introduces blur, which degrades the information in the images. Confocal images require extensive monitoring periods which may harm the dynamic events of invasion. This thesis devises two new quantitative parameters, Relative Invasion (RI) and the Opening Rate of the Endothelial Monolayer ($OREM$), to objectively assess the invasion, which required novel image-processing procedures. The first parameter, RI, was defined as the percentage of sarcoma cell signal below the monolayer. This procedure consisted of the restoration of the endothelial monolayer surface from a stack of wide-field images. In brief, the z-location of the surface was first determined. Certain surface regions contained unreliable cell signal readings, because of blur introduced by wide-field microscopy, and needed to be constructed with interpolated values in order to estimate RI correctly. It also included segmentation of sarcoma cell signal in the projection image by investigating the diffusion rates over multiple convolutions. The second parameter $OREM$ was defined as the speed at which the sarcoma cells open the monolayer at early stages of the experiments.

The system was successfully applied and our approach revealed a novel aspect of

the invasion process, namely its non-linear modulation by the shear flow, similarly to white blood cells.

1.4 Thesis overview

The remaining parts of the thesis are organised as follows:

Chapter 2 contains background information and related work. It explores the current use of flow chambers, how invasion has previously been quantified and some related image-processing techniques.

Chapter 3 contains descriptions of the experimental set-up used for the experiments which include the new Open flow chamber and the corresponding acquisition technique. It also defines the quantitative parameters.

Chapter 4 contains descriptions of the surface reconstruction which is divided into three sections: surface estimation, identification of unreliable regions of endothelial monolayers and interpolation over these regions.

Chapter 5 contains descriptions of the segmentation of sarcoma cells and explores histogram-based segmentation and segmentation based on Linear diffusion.

Chapter 6 contains Validation of image-processing procedures and the quantitative parameters with their statistical significance.

Chapter 7 contains biological results of the findings.

Chapter 8 contains a discussion on the possible implications of the findings, conclusions and future work.

Chapter 2

Background

2.1 Cancer-cell invasion

Cancer is one of our most common diseases. Discovering tumours at an early stage significantly increases the chances of survival and the fate of the patient is more successful [10]. Early detection helps in the prevention of metastasis, which is one of the key elements in successful treatment. Metastases occur when cancer cells detach from the primary tumour, penetrate the blood vessel wall and enter the blood system. The cells are then circulated until some attach to a vessel wall, invade the tissue and start multiplying to form a new tumour [8] (see fig. 2.1). However, not every cell that manages to invade creates a new tumour. Most cells die during the circulation process and do not survive and transmigrate [11] [12] [9]. Only those that proliferate will create a secondary tumour and it is therefore important to understand the properties of the metastatic cascade.

Cell motility is thought to be involved in the invasion step of metastasis. Motility can be seen as sequential steps of pseudopodia extensions, adhesion, intracellular contraction and intracellular retraction (rear release) [13] where the cell scans the

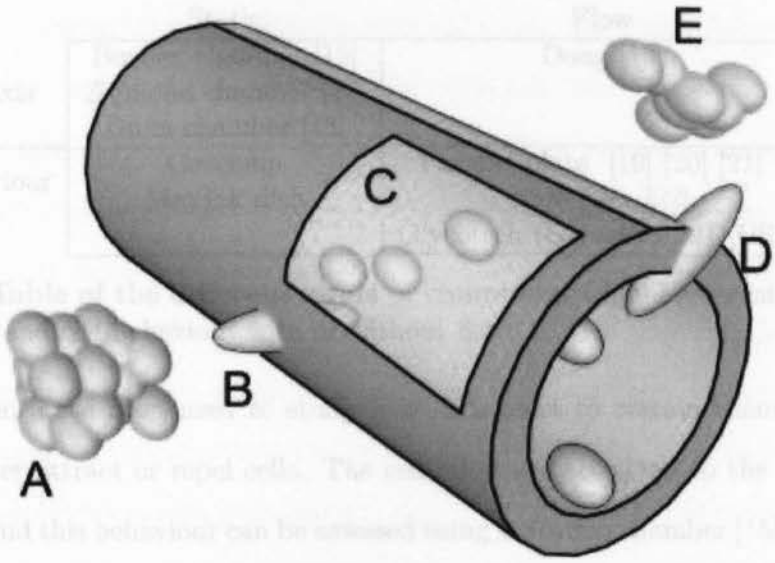

Figure 2.1: **Diagram of the metastatic cascade illustrating the importance of active cell migration through the endothelium.** A subset of tumour cells leaves the primary tumour (A) and intravasates (B) into the blood circulation system (C). Some of those cells adhere to the vessel wall at a remote site and extravasate (D) into the surrounding tissue. Proliferation occurs once the transmigration through the endothelial cells is complete and forms the basis of a secondary tumour metastasis (E).

surroundings with its pseudopodia and adheres to the endothelium, contracts its body towards the leading edge and finally releases its rear end to complete the motion. The invasive characteristics are influenced by different stimuli linked to motility and a number of factors have been identified as being responsible. These can be grouped as autocrine motility factors, extracellular matrix proteins and host-secreted growth factors [14]. These cause a tumour cell to direct itself towards e.g. a chemical gradient or towards the source from where the factor originated.

In order to study motility and invasion *in vitro*, a number of chambers have been developed during the years and can be arranged into two groups with two subgroups each as seen in Table 2.1. Some of them are used to study the influence of chemotaxis in relation to migration *in vitro* [15] [17] [18].

	Static	Flow
Chemotaxis	Boyden chamber [15] Zigmond chamber [17] Dunn chamber [18]	Dong [16]
Cell behaviour	Coverslip MatTek dish	Parallel-plate [19] [20] [21] Side-view [22] Glycotech (Glycotech,MD,USA)

Table 2.1: **Table of the different kinds of chambers.** Chambers exist to examine chemotaxis and cell behaviour with or without flow.

Chambers have been used to study how cells react to certain chemical agents. Agents either attract or repel cells. The cells that are attracted to the agent move towards it and this behaviour can be assessed using a Boyden chamber [15]. A Boyden chamber consists of two compartments, separated by a microporous filter. One agent occupies the lower compartment and the cells, combined with another solution, are located in the upper compartment. The cells then travel towards the lower section through the filter. The distances the cells have travelled inside the filter reveals their attraction. The holes within the filter are so tiny that the cells can only enter it by choice and not by e.g. gravity. This will ensure that the cells deliberately move toward the chemical substance. The filter is then post-examined manually using a microscope to evaluate the invasion. An advantage with this approach is that the experiment and evaluation are easy to perform and simple to assess, and there are few variables to take into consideration. However, it does not allow for direct viewing. Solutions have been devised to solve this problem. The Zigmond chamber [17] is one which tries to implement a direct viewing approach. It is made of glass or plexi-glass with two rectangular compartments separated by a bridge with height 1mm. The two wells are filled with two different solutions. The cells are grown on a separate coverslip which is mounted over the wells and the bridge with the cells "upside down", facing the agents. The coverslip is held in place by two spring clips at each end. This set-up allows for a

gradient to be formed over the bridge to which the cells can react. Since the chamber is transparent - unlike the Boyden chamber - the cell behaviour can be monitored during its course. The material of which the chamber is made also has good optical properties which is important to obtain meaningful images. One negative aspect of this invention is that there is no fixed distance between the bridge and the coverslip where the cells reside. The springs which hold the coverslip may introduce different forces between experiments, causing the chamber to have different distances between the bridge and the coverslip and this may affect the result. It is thus difficult to repeat the experiments with identical settings. A Dunn chamber [18] overcomes this problem by modifying a commercially manufactured counting chamber. A counting chamber consists of a round well, centred on the coverslip with a fine grid net at its bottom, which allows the experimenter to visually count the number of cells on the coverslip. The modification consists of drilling a second, inner well. The inner well contains one chemoattractant and the outer another, preferably weaker, agent. The coverslip is positioned over the wells and sealed with wax, leaving a small opening by the outer section. The gap is used to suck out the medium contained in the outer well and replaces it with whatever solution is required. The opening is lastly sealed as well. This set-up assures a fixed gradient over the bridge and there is no excessive leak of fluid from one compartment to the other. The Dunn chamber is also made of thin glass which makes it suitable for a wide range of applications in microscopy. However, it does not facilitate flow experiments. The Dong chamber [16] seems to be the first instance in which chemotaxis and shear forces are taken into consideration. Dong et al developed a modified Boyden chamber to study the influence of shear stress on the invasion process. It allows for easy assembling using six screws and the top plate features an inlet and an outlet to admit cells to flow through the window of the gasket, above a monolayer of endothelial cells. The monolayer was grown on

the top side of the filter and exposed to TC interaction and the flow. The wells below the filter were filled with a chemoattractant solution. The bottom side of the filter was then post-imaged for migrated cells. This set-up utilises the advantages of a Boyden chamber as well as a conventional parallel-plate flow chamber to assess the influence of chemoattractants on cell behaviour in conjunction with flow. Even though it provides options for flow, it lacks visual inspection. The chamber only allows for post-examination of the filter and there is no indication of cell behaviour during the course of the experiments.

The parallel-plate flow chamber has now become the mainstream tool to assess cell-cell interactions. The scheme was first proposed by Hochmuth [19] and later devised by Lawrence *et al* [20] where a vacuum was used to ensure a fixed height between the coverslip and the bottom of the chamber. The chambers consist of two parallel plates where, for example, ECs are cultured on the top plate and the bottom plate holds a gasket to - when vacuum is applied - ensure a distinct height of the chamber. These are used to record the cell behaviour during the experiment (direct viewing) while exposed to flow. New proposals also include the Glycotech flow chamber (Glycotech, MD, USA) which is circular and smaller than previous chambers. A disadvantage though is that these do not facilitate a way of directly injecting the cells. Cells have to circulate through the tubing, which may allow the cells to adhere and cluster inside the tubing. This is also time consuming. The time it takes for the cells to travel from the injection point through the tubing and into the chamber can be considerable. A comparison of flow chambers can be found in [23]. Recent developments also include side-view chambers which allow for axial instead of lateral investigation [22] [24]. Two rectangular coverslips were adjusted so that the surface had a 45° slope on each side of the flow channel. The coverslips were coated with a reflective substance. The light source originated above one of the

mirrors which directed the light through the side of the specimen. The objective lens was located below the mirror on the opposite side. This opens up new possibilities to study how the interactions between the cells occur axially which is relevant in invasion studies. The optical properties could possibly be a problem since mirrors do not reflect all light. This may also affect the signal-to-noise ratio and produce noisy images.

TCs interact with endothelial cells and release chemoattractants [25] which contain valuable clues to the adhesion [26] [27] and invasion [28] and are thought to be involved in these steps [29] [30] [31] . It was previously discovered that leukocytes can open endothelial cell (EC) junctions through chemotactic stimuli and invade the tissue in static conditions [32]. This coincides with static results where images from Scanning electron Micrographs clearly show that tumour cells induce "holes" among ECs [33] and eventually form secondary tumour colonies [34]. Some studies suggest that signalling pathways are involved in the retraction and that the process is TC-initiated [35]. Adhering and extravasating tumour cells tend to cause EC opening and retraction [34] which typically culminates within 1 hour but can still be ongoing, with declining intensity, for up to 24 hours after initial adherence [36]. *In vivo* experiments also support these results [37].

Cancer cells propel through the barrier once the endothelial junctions are disassembled [38]. The mechanism by which the tumour cells open EC is not yet fully understood. In some studies, neutrophils are thought to assist tumour cells in their strive to extravasate during flow [39], either by chemotaxis [40] or motivated by shear forces [41]. Among shear, shear rate expresses higher importance than shear stress as the neutrophil-facilitated contact with EC tends to increase during former conditions [42].

In certain situations, TCs have the ability to completely and permanently damage

the connections between the individual endothelial cells, which will eventually cause apoptosis [43] [44]. Nevertheless, the layout of the endothelium is highly dynamic and enables restoration capacities among EC (without apoptosis) once extravasation is completed [45]. This suggests a dual response to invasion where the duplex is not fully understood.

2.2 Assessment of cancer-cell invasion

One path to understanding metastasis is to quantify the invasion process. Li *et al* [46] incorporate a Boyden chamber coupled with a radioactive labelling technique to measure invasion. Transwell chambers form a dual compartment chamber with confluent monolayer of endothelial cells grown on a filter as separation. Tumour cells then travel from the top compartment towards the bottom and the invasion is measured as the ratio of radioactivity in the lower compartment related to the total. This circumvents the labour-intensive procedure of visually counting the invaded cells. However, it does not facilitate direct viewing, which makes the visual monitoring of the cells during the experiment impossible. The radioactive labelling may also prove to be toxic to the cells and may alter the cell function if the experiments are performed over extensive periods.

The 3D trajectories of the nucleus of invading cells have also been investigated where cells invaded a layer of collagen gel [47]. Image stacks were obtained from an inverted fluorescence microscope every hour, providing a 4D dataset which was used for analysis. The centroid of each cell is located manually in each (full) projection (XY, XZ and YZ) and stored together with the time information in a data file which provided the voxel centroid over time. This was repeated for every cell and time point and provides evidence for a significant difference in their migration kinetics (i.e. non-

invasive cells migrated less) in 3D which was not evident in 2D. The method, however, is labour-intensive and only tracked the centroid. An automatic way of tracking cells from 3D stacks was also developed [48] where 3D stacks of gel consisting of a mixture of collagen and matrigel were obtained as a tiled series. The cells were automatically segmented and their 3D trajectories were calculated based on a nearest-neighbour algorithm. The nearest-neighbour window was divided into 12 regions forming the basis of a 13-state Markov chain representing eight axial states, four lateral states and one stationary state. The movement of the cells was then classified according to their movement in the window relative to the previous frame. All of these solutions give a good indication of the direction of the cell movement (in 3D) but no information about the invasion as such. It provides information about cell journey and movement but not the amount of invasion.

A recent study has revealed tumour-cell behaviour related to the breakdown of endothelial cell junctions under flow, featuring a parallel-plate flow chamber [49]. Morphology of tumour cells was assessed manually and axial and lateral spreading were quantified by using fluorescence microscopy. Measuring the spreading axially and laterally aided numeric analysis of the elongation. This facilitates an estimate of the activity as the cells spread both axially and laterally under shear stress. Hart *et al* [50] present a way of quantifying the metastasis and investigate the different steps involved under static conditions. A matrigel invasion chamber hosts the participating specimen (Bone marrow endothelial cells (BMEC) and prostate cell line (PC-3)) and provides an opportunity to objectively explore the cooperation between the cell types. The progression was also monitored every 30 min for 10 hours using a confocal microscope (LSM510). The images captured revealed that during the time course, TCs pseudopodia reached toward the coverslip and pressed in, under the endothelial layer, and the entire body had extravasated after 3.5 hours. This implies

that the interaction between the two sides is an ongoing process. The invasion is slower than for monocytes and this may be due to the fact that TCs are larger than monocytes (higher resolution images are used to capture monocytes) [51] and can not slip through the junctions as easily. It therefore has to extend its filopodia into the endothelium and cause a retraction. The complete journey, including adherence to endothelium, invasion and migration through junctions, is measured to about 4 hours [50]. Quantitative analysis of invasion is of interest to many biologists and an efficient and reliable experimental set-up as well as analysis techniques are important to produce statistically legitimate studies.

In order to contribute to a potential improvement of the current understanding, this project studies metastasising sarcomas in an inbred rat model [52] where the metastasising cells have to invade through the endothelial monolayer during flow conditions *in vitro*. Furthermore, it would be of great interest to study the dynamics of the invasion process in a direct viewing approach. This thesis describes a new invasion assay *in vitro* consisting of a new flow chamber and novel image analysis to provide measurements of the invasion dynamics.

2.3 Imaging modalities in microscopy

A light microscope is invaluable when investigating living species such as cells. Light microscopy makes it possible to explore the behaviour of the cells *in vitro* without causing harm or damage. An example of a description of a simple light microscope can be seen in Fig. 2.3. The cells are exposed to a set of light beams, which highlights their features. A light source illuminates the specimen and the resulting light is collected at the eyepiece to form the actual image. In a light microscope, both visible light and ultraviolet light can be used to visualise the specimen and the resolution is governed by refraction [53], diffraction [54] and the Point Spread Function [55]. An overview of common live cell imaging/microscopy techniques can be found in [56] [57] [58].

2.3.1 Point Spread Function

The image formation in a microscope can be described as a convolution process according to Eq. 2.1. The observed stack O is formed when it is convolved with the unknown light-spreading function (i.e. the PSF) which describes how the light is spread throughout the specimen. Fig. 2.2 shows a projection of an acquired PSF. The basic principle of convolution is that the PSF is shifted so that its centre is located at each 3D point and the contribution from each shifted PSF is integrated. The observed image O and the PSF (Eq. 2.1) are acquired data and S is the unblurred image. All 3D wide-field microscopy images contain light which originates from the rest of the cell and degrades the image.

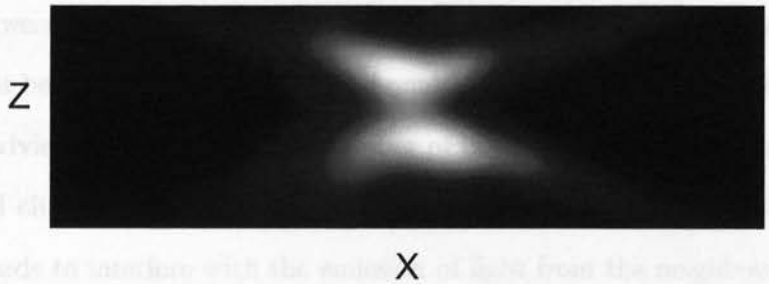

(a)

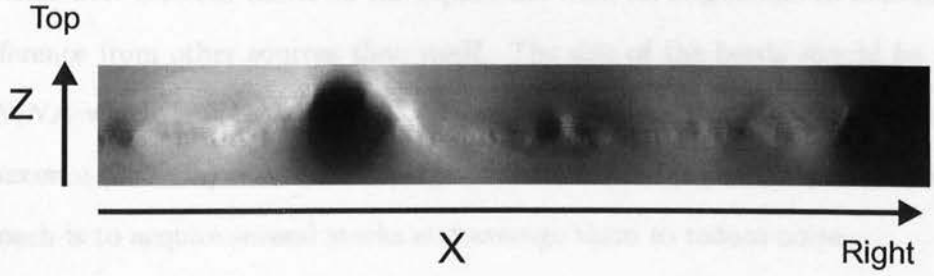

(b)

Figure 2.2: **Example of an XZ-projection of an acquired Point Spread Function (PSF).** A single point influences its neighbouring points in a manner described by the PSF. The surrounding voxels are affected, mainly in Z-direction but also in XY. This behaviour is due to asymmetry of the optics. A black pixel in the image represents no influence from the point source and white represents heavy influence. **(a)** XZ-projection of an acquired PSF **(b)** XZ-projection of a wide-field image stack

Blur prohibits a user from examining the focal plane accurately. The information about the degradation process can be obtained from a 3D image stack of a point source, which usually consists of a fluorescent bead. Images of the bead are obtained at several focal planes, below, at and above the in-focus plane and form the (PSF).

$$O(x, y, z) = S(x, y, z) \otimes PSF(x, y, z) \tag{2.1}$$

A PSF can be obtained both theoretically and experimentally. Software (e.g. Huygens, Scientific Volume Imaging, Netherlands) is used to obtain a PSF theoretically which usually requires knowledge of the numerical aperture of the objective lens, wavelength of the emitted light, the dimensions of the PSF, size of a pixel and distance between the z-planes. An experimental PSF is acquired by capturing stacks of fluorescent beads. The beads are placed onto a dish or a coverslip which is then imaged. It is advisable to use a smaller number of beads compared to a larger number, as unwanted clusters are likely to form which will cause the light emitted from the clustered beads to interfere with the emission of light from the neighbouring beads.

Beads were selected based on the separation from its neighbours to minimise the interference from other sources than itself. The size of the beads should be 1/3 of $1.22\lambda\backslash NA$ which is $0.41\lambda\backslash NA$ [59]. In our case where the $NA = 1.4$ and green fluorescence (500 nm) was used, the size of the bead should be $0.15\mu m$. A common approach is to acquire several stacks and average them to reduce noise.

2.3.2 Wide-field Fluorescent Microscopy

Wide-field fluorescence microscopy is one of the most important tools in cell examination. It gives the ability to visualise the fundamental structures that exist within the cell in their natural hydrated environment. Figure 2.3 shows the design of a light

microscope. The light emitted by the lamp is passed through the system, reflected by the specimen and recorded by the sensor. The collector lens collects the light produced by the lamp and focuses it on the dichroic mirror while the objective lens assembles the reactive light (which reacted with the specimen). The dichroic mirror is a semi-transparent mirror which selectively pass a range of wavelengths. This allows only the fluorescent light to reach the eyepiece. As an extra precaution, a barrier filter is installed to make sure the correct wavelength is used in the imaging. The microscope can be divided into three sub-systems with respect to how the light travels according to the list below [60].

1. Light source - collector lens - excitation filter and dichroic mirror
2. Objective lens - specimen - objective lens – dichroic mirror
3. Barrier filter - eyepiece lens – sensor

The aim of the first sub-system is to focus the light on the specimen. The light usually originates from a mercury lamp or a xenon lamp and emits UV-light. It is of importance that the specimens are uniformly illuminated in order to avoid shadows in the images. The objective lens assembles all light and focuses it onto the cells. The light will react with fluorophores in the specimen and produce a resulting set of light waves. The incoming and outgoing rays of the objective lens will be of different wavelengths and therefore the outgoing light is able to pass through the dichroic mirror. The eyepiece lens makes the light visible to the eye or the sensor which digitises

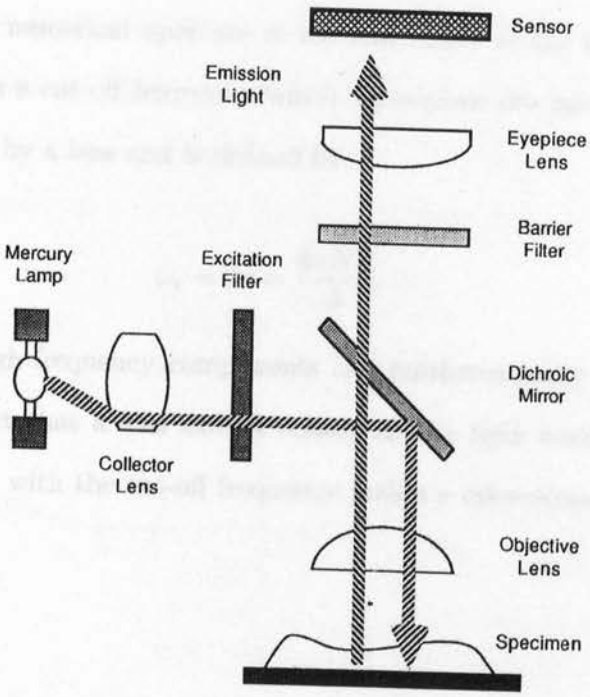

Figure 2.3: **Fluorescence imaging system set-up.** The fluorescence microscope consists of a lamp and an excitation filter that only allows the specific excitation wavelength to pass through to the dichroic mirror, which has the ability to reflect a certain wavelength and be transparent for another. This ability grants only the emitting light access through the mirror while the exciting light is mirrored towards the specimen. The objective lens focuses the light onto the specimen and the eyepiece lens focuses the light towards the detector.

the image. The sensor is usually a CCD-camera.

Each lens is characterised by

$$a = \frac{2\pi NA}{\lambda} \tag{2.2}$$

where NA is the numerical aperture of the lens and λ is the wavelength of the light. Every lens has a cut-off frequency which determines the maximum frequency that can be resolved by a lens and is defined by

$$\omega_c = 2a = \frac{4\pi NA}{\lambda} \tag{2.3}$$

The cut-off of high-frequency components can mathematically be described as convolution. The fact that a lens cannot collect all the light available (due to its limited size) together with the cut-off frequency makes a microscope a band-limited system.

2.3.3 Confocal microscopy

Confocal microscopy was invented in the 1970s and it is thought to provide an intermediate resolution between wide-field and electron microscopy. It provides higher resolution than a wide-field but still with the possibility to study living specimens. Confocal microscopy also provides optical sectioning which reduces the out-of-focus information normally present in the wide-field technique, leading to reduced contrast [61]. Images obtained with confocal microscopy are clear and sharp immediately after the acquisition without the need for any post-processing.

The set-up of a confocal microscopy can be viewed in Fig. 2.4. Since the exact

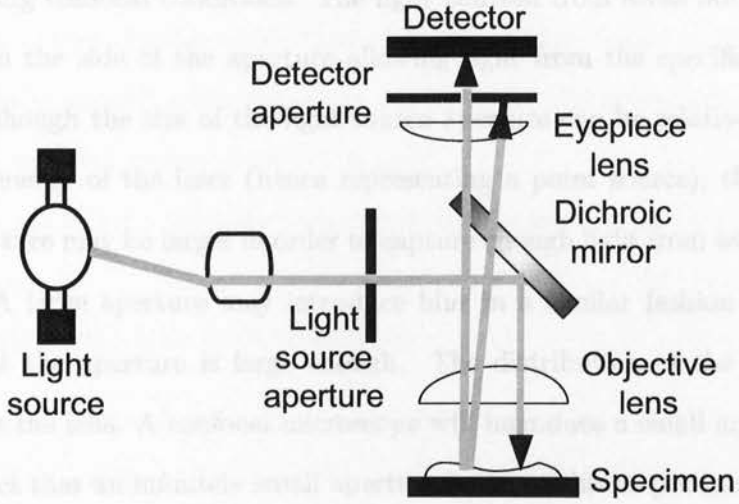

Figure 2.4: **Diagram illustrating the principles of confocal microscopy.** A light source emits light which travels through an aperture (light source aperture). The light is reflected by a dichroic mirror onto the specimen. The fluorescently labelled cells respond by emitting light different from the excitation wavelength. A pinhole in front of the detector blocks out-of-focus light and detects the in-focus. A confocal microscope exhibits similar layout to a wide-field microscope with a few exceptions. Two of those are the light source aperture and the detector aperture which only allow in-focus light to progress through the system.

location of each scan is known, we can then obtain a 3D representation of the specimen using the fluorescence intensity level for each voxel $< x, y, z >$. The specimen is then

scanned line by line, plane by plane, until the defined range has been covered. The term confocal stems from the fact that the image of the light source aperture and the image of the detection aperture have the same focus.

One conclusion that can be drawn from Fig. 2.4 is that a point illuminated by a point light source will be equally illuminated on the detector side (considering optimal conditions) [62]. To minimise the effects of diffraction, small apertures are positioned at the light source and the detector and are the main differences compared to wide-field fluorescence. The detection aperture must be positioned so that only light that coincides with the focal plane travels through to the light detection device, hence achieving confocal conditions. The light emitted from areas not in focus will bounce off on the side of the aperture allowing light from the specific voxel to be received. Although the size of the light source aperture can be relatively small due to the high energy of the laser (hence representing a point source), the size of the detector aperture may be larger in order to capture enough light from weakly labelled specimens. A large aperture may introduce blur in a similar fashion to wide-field provided that the aperture is large enough. The distribution of the light is then dependent on the lens. A confocal microscope will introduce a small amount of blur due to the fact that an infinitely small aperture is impossible to produce. This turns the image-generation process into a convolution process. Therefore, some out-of-focus information is unavoidable but the quality is far better than wide-field. The sectioning property of the confocal technique is an important aspect. Due to the directed emitting light from the light source and the detection aperture, only the light from the imaged voxel will reach the detection device. In wide-field microscopy the in-focus plane will be imaged sharply and the other planes will be blurred, as all light will reach the detector. The drawback with the confocal technique is that it requires a long time to acquire, an image as each voxel in the specimen has to be imaged.

It is also fluorescence-intensive as each $< x, y >$ is exposed to light multiple times when acquiring optical sections. Long monitoring periods with multiple acquisition are therefore in some cases prohibited. This makes the technique useful for high-resolution images, acquisition of fixed specimens or specimens with slow movement.

2.4 Image-processing techniques

An image stack acquired with a wide-field microscope contains blur which interferes with the cell signal. As a result, the cell signal is not readily available without manual intervention. Manual involvement may allow variations between experiments due to the subjective nature of those estimations. Instead, we would like to obtain an objective, computer-generated measurement of the invasion which requires computerised segmentation and estimation of the cell signal.

The following sections describe techniques used to segment cell signal.

2.4.1 Gaussian Mixture Models

Consider a set of scattered multidimensional data points $(\mathbf{x}_1, \mathbf{x}_2, \ldots, \mathbf{x}_n)$ which form m clusters. We can define a multivariate Gaussian model such that

$$P = \sum_{k=1}^{m} w_k p_k(\mathbf{x}_i), \qquad w_k \geq 0 \qquad i : 1, 2, \ldots, n \tag{2.4a}$$

$$\sum_{k=1}^{m} w_k = 1 \tag{2.4b}$$

where w_k is the weight (i.e. prior or mixing coefficients), the sum of the weights of all clusters has to be $= 1$ (Eq. 2.4b), p_k is the probability of cluster k and P is the mixture model. The general multidimensional case of the probability where

the point $\mathbf{x}_i$ belongs to the cluster k, given the average $\mathbf{a}_k$ and covariance $\mathbf{S}_k$, is defined in Eq. 2.5 [63] where the parameters $(\mathbf{x}_i - \mathbf{a}_k)^T \mathbf{S}_k^{-1} (\mathbf{x}_i - \mathbf{a}_k)$ represent a matrix multiplication and $\mid \mathbf{S}_k \mid$ the determinant of $\mathbf{S}_k$.

$$p_k(\mathbf{x}_i) = N(\mathbf{x}_i; \mathbf{a}_k, \mathbf{S}_k) = \frac{1}{(2\pi)^{d/2} \mid \mathbf{S}_k \mid^{1/2}} exp\left(-\frac{1}{2}(\mathbf{x}_i - \mathbf{a}_k)^T \mathbf{S}_k^{-1} (\mathbf{x}_i - \mathbf{a}_k)\right) \quad (2.5)$$

This gives the probability that a point is drawn from a d-dimensional Gaussian distribution with mean $\mathbf{a}_k$ and covariance $\mathbf{S}_k$. The task is to estimate the weight w, average $\mathbf{a}$ and covariance $\mathbf{S}$ for each cluster. The E-M algorithm performs such a task in which these values are estimated. The principle is described in Fig. 2.5.

So each pixel contributes to each mixture with a different amount defined by d. By alternating between the E-step and the M-step a fixed number of times, the estimates will approach the true value. The M-step is practically realised by the iterations. The more iterations, the closer the estimate will be to the true value. The run time for the algorithm depends on the expected accuracy of the result and more iterations obviously give greater accuracy.

The EM algorithm needs to be initialised by given starting values for the weight, average and covariance. This can be achieved by *kmeans* algorithm [64] or any other clustering algorithm. The goal is to minimise the sum of squared distances within each cluster. *kmeans* initialises the centres randomly. The distance from each point to each cluster centre is then obtained and the point is assigned to the cluster to which it is closest. This step is repeated until no data points are changing cluster or a predefined number of iterations has been reached. The output from *kmeans* is fed into EM which utilises this as its starting point. If these estimates are incorrect or badly chosen, EM will take extensive time to converge. It may also converge to a

E-step: Calculate the contribution of point $\mathbf{x}_i$ to the gaussian mixture component k

$$d_{ik} = \frac{w_k N\left(x_i; a_k, S_k\right)}{\sum_{j=1}^{m} w_j N(x_i; a_j, S_j)} \tag{2.6}$$

M-step: Calculate a new weight w, average $\mathbf{a}$ and covariance $\mathbf{S}$ for each mixture component k

$$w_k = \frac{1}{n}\sum_{j=1}^{n} d_{jk}$$

$$a_k = \frac{\sum_{j=1}^{n} d_{jk} x_j}{\sum_{j=1}^{n} d_{jk}}$$

$$S_k = \frac{\sum_{i=1}^{n} d_{ik}\left(x_i - a_k\right)\left(x_i - a_k\right)^T}{\sum_{i=1}^{n} d_{ik}}$$

Figure 2.5: **Description of the EM algorithm.** The algorithm alternates between the E-step and the M-step for some iterations. The average is recalculated during every iteration and will eventually converge. In the E-step, the probability $N\left(x_i; a_k, S_k\right)$ is calculated using Eq. 2.5 given the parameters for a particular cluster. Repeat the E-step for all pixels and every cluster. Then, using the M-step, recalculate new weights, average and covariance for each cluster. Repeat the E-step and M-step until the number of repetitions has been reached.

local minimum instead of the global.

The probabilities that a point belongs to cluster 1 and cluster 2 are obtained according to E-step - Fig. 2.5. This is repeated for every point. The parameters of each cluster within the mixture are then updated using the M-Step. The algorithm alternates between these two steps until a certain number of iterations have occurred or the difference in likelihood between the current step and the previous step has reached a certain value. The likelihood function is defined according to Eq. 2.7 [65].

$$\text{Ł} = \left(\prod_{i=1}^{n} p_i(x_i; a_i, \Sigma_i)\right) \tag{2.7}$$

Often the log-likelihood is used, which is the log of the likelihood function in Eq. 2.7.

A disadvantage with EM is that the number of clusters has to be known. This property usually comes naturally since the clusters often represent a physical event. However, if such an event does not exist, selecting the number of clusters can be somewhat difficult [66] although the likelihood can be utilised to estimate an appropriate number by maximising the Bayesian information criterion (BIC) [67]. Advantages are that each point is given probabilities of belonging to a particular cluster and the statistics of the cluster can be used to estimate missing data points. GMM can also be used in classification where the distribution of the objects are known. The distribution from the unknown object (e.g the mean) is compared with the distribution of a known object and a match is made if the value is within the known distribution [68].

2.4.2 Principal Components Analysis

Principal Components Analysis (PCA) is a common technique for dimensional reduction. The main concept is to reduce the dimensionality of a matrix while still maintaining as much of the variation as possible. This is achieved by transforming the existing data into a new set of variables, Principal Components (PC), so that the first few components represent most of the variation in the original dataset. The transformation turns a set of correlated vectors into a new set of uncorrelated vectors (PCs) and this approach can reveal structures in the data that are not obvious without transformation.

The transformation can be written in mathematical terms as

$$\mathbf{z} = \mathbf{V}_k^T \mathbf{x} \tag{2.8}$$

where $\mathbf{x}$ is the original data to be transformed and $\mathbf{z}$ is the output after transformation determined by PCA, i.e. the Principal Components (PCs); $\mathbf{V}^T$ is a transposed version of the matrix $\mathbf{V}$ where the *nth* column represents the *nth* eigenvector of the covariance matrix of the original data $\mathbf{x}$.

If $\mathbf{A}$ is an $m \times n$ matrix with m observations in n variables then the PCs are found by using the scatter matrix. The observed covariance matrix C (a.k.a. scatter matrix) is defined in Eq. 2.9 [69].

$$\mathbf{C} = \mathbf{A}^T \mathbf{A} \tag{2.9}$$

A common approach to obtain the eigenvectors and eigenvalues is to apply Singular Value Decomposition (SVD). The decomposition produces three additional vari-

ables according to Eq. 2.10.

$$[\mathbf{U}, \mathbf{S}, \mathbf{V}] = svd(\mathbf{C}) \tag{2.10}$$

The contents of these are such that the columns of **V** represent the eigenvectors and the diagonal values of S are the eigenvalues, i.e.

$$\lambda = diag(\mathbf{S}) = \begin{bmatrix} s_{11} & & \\ & \ddots & \\ & & s_{mm} \end{bmatrix}$$

The reduction of the original matrix is then performed according to Eq. 2.8.

Details of the transformation can be found in [70]. In the case of multidimensional data, the PCs can be multiplied by the columns of the original data [71] and each eigenvector can therefore be applied to the columns of the image forming an eigenimage such that

$$\mathbf{W} = \mathbf{z}_i \mathbf{V}_k^T \qquad i : i = 1, 2 \cdots n, \qquad k : k = 1, 2 \cdots m \tag{2.11}$$

and i represents the ith column in the image and k the kth eigenvector. The original image is recovered if all eigenimages are added together. If the eigenvectors were ordered in ascending order according to their eigenvalue, the vector with the highest eigenvalue represents the first principal component; the second highest represents the second component etc. The eigenvalue describes the amount of variation within the dataset (i.e. the variance) so that the vector with maximum variance is in the first dimension, second largest variance is in the second dimension etc. The dataset can then be reduced by retaining only the vectors with the corresponding p largest eigenvalues. The amount of information retained can be viewed by plotting the

eigenvalues for each PC as seen in Fig. 2.6 and is drastically decreased with a higher number of PCs.

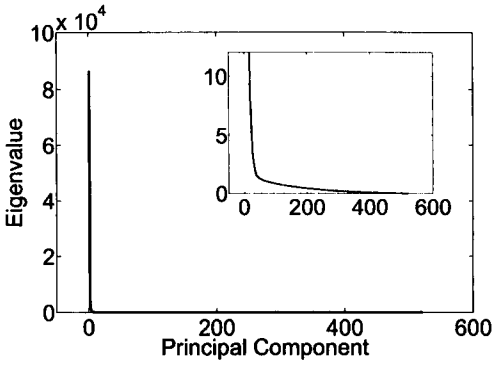

Figure 2.6: **The eigenvalues of the corresponding Principal Components.** The eigenvalues represent the amount of variation contained in each PC. The largest eigenvalue represents the first PC and, subsequently, the first PC contains most of the variation in the image. Many PCs do not contribute much to the information in the image and a reduction can then be made by discarding PCs with little variation (i.e. small eigenvalues). Choosing the number of PCs is then the overall problem.

2.4.3 Linear diffusion

Signals, or images, are viewed differently depending on the current scale or resolution. For example, an image of a building within a city offers plenty of detail compared to the satellite image. On the other hand, a satellite image over the city provides a good overview but very little detail. The two images provide levels within a scale space where the transition between the two explores the lifetime of certain features. The behaviour of signal over multiple scales is subject to variations depending on the strength of the local structures and is the major property of scale space filtering. The main purpose is to produce a compound of derived signals such that the fine detail decreases with decreasing scale. The behaviour of a signal over multiple scales was first defined in one dimension [72] and later in two dimensions [73] and can be viewed as a diffusion where the signal is diffused over the scales. Representing the signal over multiple scales segments coarse and fine details such that the coarse details remain over the scales longer and fine details will fade quicker. This is realised in mathematical terms by convolution between the signal and a kernel. High values are diffused towards lower values where they eventually reach the average signal value. The general form of the diffusion equation is formulated as

$$\frac{\partial I}{\partial n} = D\Delta I\left(\mathbf{x}, n\right) \tag{2.12}$$

where D controls the blurring at each iteration n and ΔI the intensity result at each iteration. For linear diffusion, D is constant. Witkin [72] described the Gaussian kernel as the preferable choice because of its symmetry and decreasing values away from the average. In terms of images, the process could be defined as

$$F(\mathbf{x}) \otimes G(\mathbf{h}, \sigma) \qquad \mathbf{x} \in (x_1, y_1), \mathbf{h} \in (x_2, y_2) \tag{2.13}$$

where $F(\mathbf{t})$ is the original image, $G(\mathbf{t}, \sigma)$ is a Gaussian kernel with standard deviation σ and $\otimes$ represents convolution. This implies that the Gaussian function acts as a weighting function where values close to the mean are given a high score and values further away a lower score.

2.4.4 Numerical interpolation

The cancer cells introduce openings in the monolayer in their strive to exit the flow channel. These openings introduce false readings when the surface is reconstructed and need to be addressed. In this case, interpolation nodes around the opening must be chosen as representative descriptions of the shape of the surface.

Numerical interpolation is the process by which intermediate values are estimated, and given known values. It estimates values in relation to its surroundings. The technique is based on fitting polynomial curves to the data points and the simplest form of interpolation is the linear interpolation. With linear interpolation, a linear equation was used to predict the values in-between two nodes as shown in Fig. 2.7. The interpolation function MUST go through the nodes exactly.

The interpolation function can be any polynomial that seems to fit the function values and the most common is a cubic polynomial. Multidimensional interpolation is performed by interpolating one dimension at a time with the result from the previous iteration as input to the current, as explained in the pseudo code below.

```
Y = multidimensional matrix;
for p = 1 TO num of dimensions
Y = interp1D(Y,p);
end
```

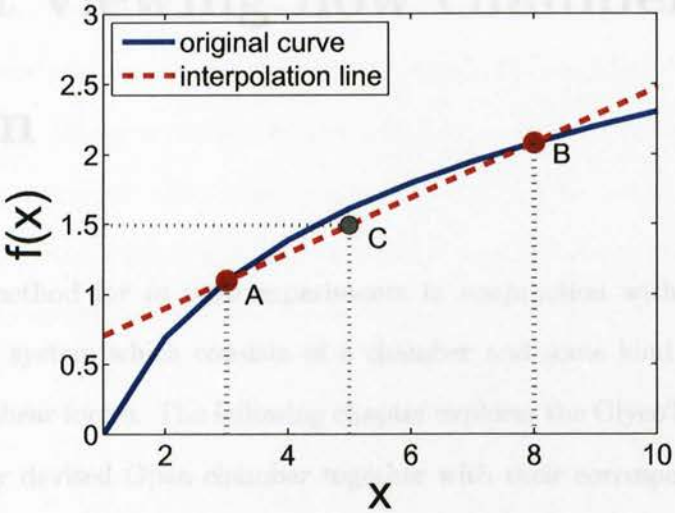

Figure 2.7: **Linear interpolation between two points.** Two known data points are chosen (A and B). A line which runs through these points is fitted to them. The value of the intermediate point C is obtained by finding $f(x)$ of the line at the position C.

Chapter 3

Direct viewing flow chamber system

A common method for *in vitro* experiments in conjunction with flow is to use a flow chamber system which consists of a chamber and some kind of mechanism to generate the shear forces. The following chapter explores the GlycoTech flow chamber and the newly devised Open chamber together with their corresponding acquisition procedures. It also includes the devised definitions of the quantitative units of invasion applied to the results given by the experiments.

3.1 GlycoTech flow chamber system

The circular flow chamber was purchased from GlycoTech Corp., MD, USA. The set-up consisted of the chamber, a rubber gasket and flexible tubing where the gasket was positioned on top of a coverslip with a confluent monolayer of endothelial cells. The gap between the chamber and the gasket/coverslip was sealed with vacuum and grease to form a tightly closed system according to the manufacturer. However, this

solution did not perform well for our purposes as leakage was a common problem. Assembling the system was also time-consuming due to the combination of vacuum and grease. Instead we developed a metal enclosure which enclosed the system as shown in Fig. 3.1. The enclosure was gently secured with three metal screws which restrained the chamber from leakage. The chamber was then ready for installation on the microscope stage.

One problem we faced was air bubbles. The assembling of the chamber did not always create an air-free environment as the union between the gasket/coverslip and the chamber made it possible for air to remain inside the chamber. The effect of these could be seen in the field of view of the microscope as large blobs floating around. These could potentially affect the measurements and the optical properties. The introduction of the sarcoma cells was also problematic as described in section 3.3.1. This led to the development of the Open chamber.

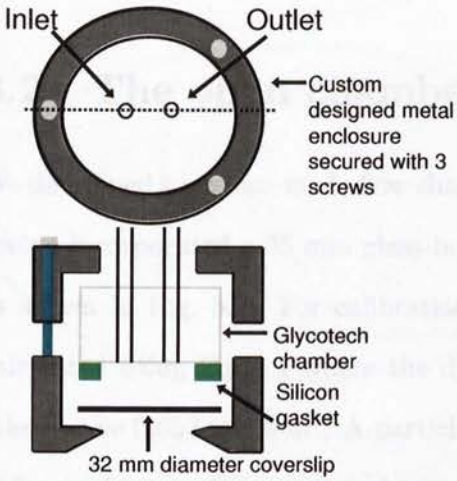

(a) Cross-section of the flow chamber system. The metal enclosure stops the chamber from leaking and keeps it in place and is secured with three screws.

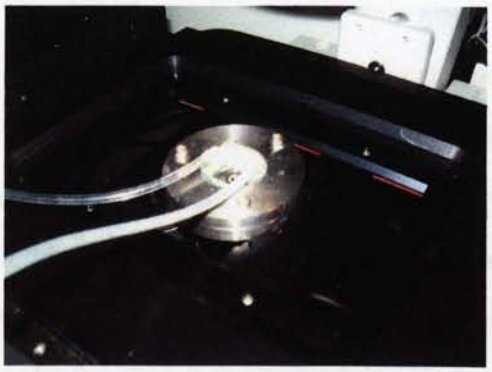

(b) Photograph of the extended chamber positioned in the stage.

Figure 3.1: **The GlycoTech flow chamber system.** The system consists of a circular flow chamber (GlycoTech Corp., MD, USA) which we have fitted into a stainless-steel enclosure to enhance stability and allow ease of use. The bottom of the chamber is sealed by a 32 mm diameter coverslip with a monolayer of rat brain endothelial cells (RBE4).

Table 3.1: **Parameters and values used in estimating the shear stress for experiments used with the open chamber.**

Notation	Parameter	Value
e	viscosity	0.653 mN s m^2
d	distance travelled	50 μm
t	observation time	277 ms
h	height above surface	8 μm
P	shear stress	14.7 dyn cm^{-2}

3.2 The open chamber

We developed a custom-made flow chamber for the direct viewing assay. The chamber design incorporated a 35 mm glass-bottom MatTek dish (MatTek Corp., MA, USA) as shown in Fig. 3.2. For calibration, the shear force P in the flow chamber was calculated using Eq. 3.1 where the dynamic viscosity of the culture medium e was taken to be 0.653 mN s m^2. A particle flowing through the chamber, at the height h of 8 μm above surface, was used to measure the flow speed by determining its travel distance d of 50 μm over the observation time t of 277 ms. The shear force P was calculated to be 14.7 dynes cm^{-2}. This fairly high shear force was chosen to give us a good contrast between no flow and flow conditions, while still lying within the range used in previous studies, such as [49].

$$P = e\frac{d}{t \cdot h} \tag{3.1}$$

The set-up comprised of a Nikon TE2000 inverted microscope (63× 1.4 NA) fitted with a scientific cooled CCD camera (Cascade-II, Photometrics) and a motorised stage (MS2000, ASI) to record about 20-30 suitable fields with a monolayer of endothelial cells, capturing red fluorescence images. The flow is then started and the

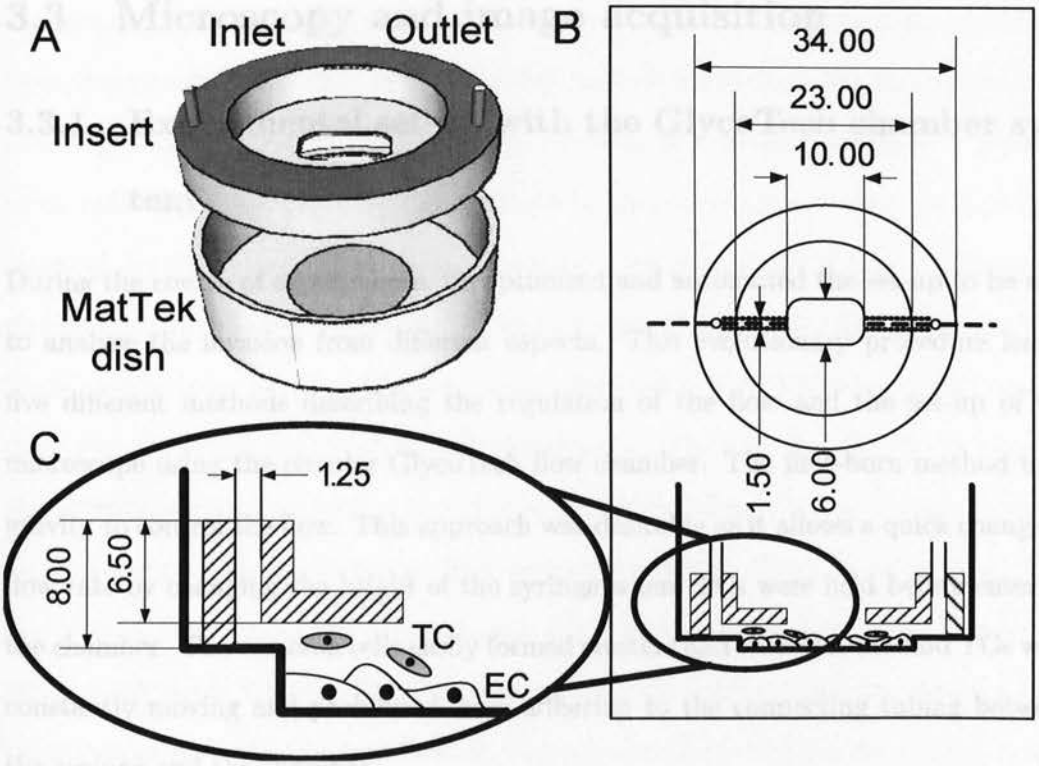

Figure 3.2: **Schematic drawing of the open flow chamber.** The custom-made Nylon insert fits into a MatTek dish with a confluent monolayer of endothelial cells (EC). The cells are exposed to the shear stress in an oval aperture in the centre of the insert. This central aperture is open and allows initial introduction of tumour cells (TC). The entire flow chamber is presented in 3D (A) and as top-view/cross-section (B). Detail view (C) depicts the vertical inlet tube, which is connected to the central aperture by a channel cut into the base of the insert using a milling machine. A symmetrical channel connects the opposite end of the central aperture to the outlet tube. On the outside, the outlet is connected to the inlet by flexible tubing going through a peristaltic pump. Measurement units are in mm.

system revisits each position at regular intervals acquiring both red (monolayer) and green (tumour cells) fluorescence stacks (excitation lambda = 540 nm and 488 nm respectively, resolution $0.2 \times 0.2 \times 1$ μm).

3.3 Microscopy and image acquisition

3.3.1 Experimental set-up with the GlycoTech chamber system

During the course of experiments, we optimised and automated the set-up to be able to analyse the invasion from different aspects. This evolutionary procedure led to five different methods describing the regulation of the flow and the set-up of the microscope using the circular GlycoTech flow chamber. The first-born method used gravity to control the flow. This approach was desirable as it allows a quick change in flow rate by changing the height of the syringe where TCs were held before entering the chamber. The sarcoma cells easily formed clusters and with this method TCs were constantly moving and prohibited from adhering to the connecting tubing between the syringe and the chamber.

In this way the amount of cells used in each experiment and the number of cells passing through the chamber would still be high. Although a high flow rate could quickly be established, the time between the cells entering the system via the syringe and entering the chamber through the tubing was still a factor, as extensive time was needed for the sarcoma cells to enter the chamber. Despite the fact that the flow rate was easily manipulated with this method, the flow rate had to be moderate in order to prevent endothelial cells from being washed away. A drawback was that there was no accurate measurement of the flow which was therefore arbitrary. It was also difficult to make the sarcoma cells adhere onto the monolayer because of the disturbing flow. This problem was solved by attaching a clamp to the outlet. The clamp opened the possibility to position the cells onto the monolayer within its field of view to a desirable area (i.e confluent monolayer) and record its adherence. One

disadvantage that occurred was, again, related to the time the cells had to travel from the syringe to the chamber. The delay made it difficult to fully know when the cells had entered the chamber. The live mode in the microscope made it possible to occasionally catch them flowing through but the performance was not accurate. Without precise measurement of the flow rate it was also impossible to calculate the duration of this process. Reducing the waiting time was a priority and one option was to inject the cells into the chamber before assembling it. This reduced the waiting time and the cell could be observed immediately. However, the first 15 minutes of the adherence process was obsolete due to the delay between injection and actually viewing them in the microscope. The acquisition began after the adherence. This meant that introducing the sarcoma cells as close to the chamber as possible would seem to be ideal. Using a T-piece connected to the flow loop would open for such an arrangement with medium flowing through the loop. A separate tubing with a separate syringe was prepared containing medium and cancer cells. The new wire contained three sections of liquid: Two with medium and one with the actual cells situated between the two regions, allowing visual assessment of the entry in to the chamber. The syringe was attached to the inlet to allow the solution to be propelled through the T-piece. This opened for a high concentration of cells injected very close to the chamber. Care had to be taken not to use force when driving the cells into the chamber due to sensitivity of the endothelial cells as they were easily washed off.

In an attempt to control the flow rate, a peristaltic pump was used as it provided a mechanism to automatically control the flow. TCs were located in a container connected to the pump and chamber with flexible tubing where one section was attached to the pump with cells ready to be transported into the chamber. The other section acted as an outlet from the chamber and carried TCs that did not adhere to the monolayer back to the container. The advantage of a peristaltic pump is that

it can reuse the medium together with the cells, which allows for long periods of monitoring. The peristaltic function also imitates the pulsation of the heart, which may have an effect on the TC invasion.

In another set-up TCs were stored in a syringe before use. The syringe was positioned horizontally on the tray of a syringe pump. The syringe was connected to the inlet of the chamber via flexible tubing and the outlet from the chamber was discharged in a container. The syringe pump was set to maintain a certain flow rate during the experiment. It also offered the option to set a series of predefined programs such as a gradually increasing rate for a period of time. However, this set-up did not facilitate any recycling of cells. In contrast, they were not exposed to mechanical forces as applied by the peristaltic pump, which may result in cell damage or cell death. Also, since this was a closed system, environmental factors such as viruses were also eliminated. Cells attaching to the syringe wall was also a problem even though the syringe pump rotated the tray to avoid cells becoming stationary.

To automatically detect whether a sarcoma cell actually had adhered while using any of the protocols described, an extension to the acquisition system was developed (see Fig. 3.3). Before the time-lapse acquisition started, we searched manually in the chamber for areas with confluent monolayers. Once a confluent area was found, its position was marked in a list in the Metamorph acquisition system (Molecular Devices Corporation, U.S.A.). Around 80 different positions were needed. The flow was introduced and the system then visited each position consecutively and, for each position, a single DioGreen image was acquired. A pause of five seconds was ordained and another single DioGreen image was captured of the same position. Applying a global threshold (set to 1000 for a 12-bit range) for both images aided the segmentation and the AND operator was employed to form a joint image. If the resulting area was above a certain size (typically 0.2% of the number of pixels in the

image), it was concluded that a cell actually had adhered and a stack was captured. Two single images (with the AND operator applied respectively) were obtained to include only stationary sarcoma cells and to avoid cells just flowing through and accidentally coinciding with the acquisition. Hopefully the sarcoma cells would adhere at one of these positions. We pre-scanned the chamber for up to 200 confluent areas of monolayer and marked these in a list in the Metamorph acquisition system before the flow was introduced.

All of these set-ups to introduce the sarcoma cells into the chamber share some common problems. One is that it is difficult to determine when TCs enter the chamber. TCs have to travel through the tubing in order to reach the chamber. This timing could be calculated by investigating the flow rate and the volume of the tubing and then estimating the time the cells required to travel into the chamber. The entrance time was needed in order to start the acquisition correctly, preventing the cells (mainly ECs) from bleaching and stopping toxins released by the labelling. However, the calculated time would only be a rough guide and scanning through the chamber for cells still had to take place. It was also common that TCs, while travelling inside the tubing, attached to the tubing wall. This resulted in a low number of cells actually completing the journey. A solution was to increase the flow rate, but TCs might then have traversed through the chamber without any chance of interacting with the monolayer. This approach also altered the value of the shear stress that the experiments were designed for. Both set-ups have problems in terms of allowing TCs to adhere to the monolayer and knowing the time of this event. The flow created a difficult environment for this task. One option would be to stop the flow for a short period to allow TCs to initiate this process. However, some of the cells are still inside the tubing and will adhere to the wall when the rate decreases. The distribution of TCs inside the tubing will also affect the number of cells that will actually adhere

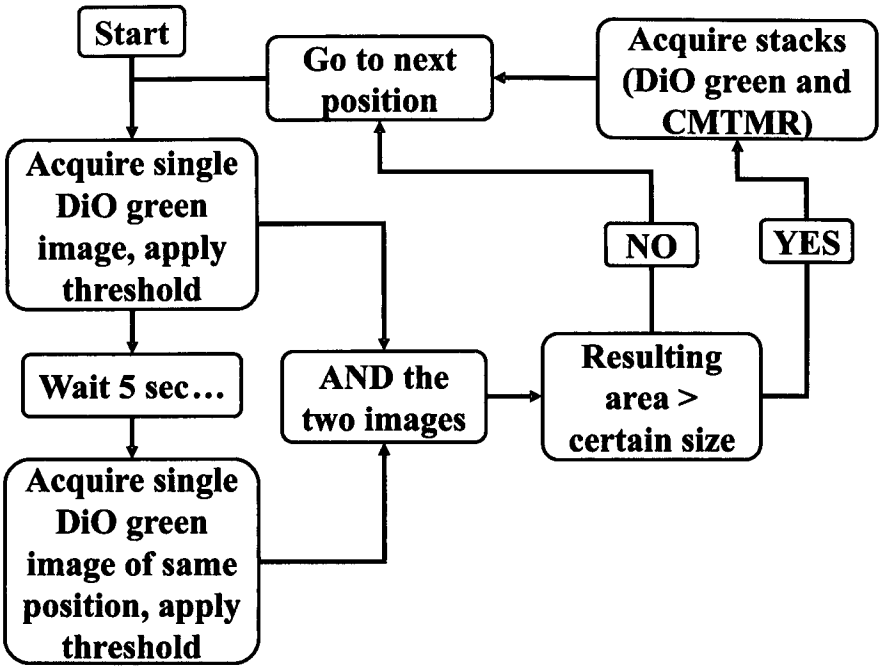

Figure 3.3: **Flow chart of an image-acquisition protocol used with the Extended GlycoTech chamber.** The protocol is designed to capture cancer cells that adhere and settle down to the monolayer during flow conditions. A list of predefined positions was stored in the Metamorph acquisition system. The positions were visited consecutively and, for each position, a single image of the DiO green channel was acquired. A pause of five sec was ordained and a second image was obtained of the same position. Both of these images were thresholded at intensity level 1000 for 12-bit images. The AND operator applied to these two captures resulted in a binary image suitable for detecting adherent cancer cells. In the case of adherent cells, the binary image contains segments of the stationary cell whilst a non-stationary cell produces an empty image. A cell was considered as stationary if the number of segmented pixels was > 0.2 % of the number of pixels in an image (typically 696×520).

and invade when the flow rate drops. These issues led to the development of the open chamber described in section 3.2.

3.3.2 Acquisition with the Open chamber

The custom-made flow chamber with labelled endothelial monolayer was connected to a peristaltic pump by flexible tubing to form a circulation system. The chamber

was secured into a 35 mm culture dish stage insert and placed onto the microscope stage within a 37°C temperature-controlled enclosure. Since the endothelial cells may change shape and compromise confluency when flow is started for the first time, shear flow was applied for an interval of 15 min before choosing 20 confluent observation fields based on visual inspection of the labelled endothelial cells. The fields were selected for subsequent multi-field recording in the Metamorph (Universal Imaging Corp, USA) software for acquisition of images using a 60× 1.45 NA lens on a Nikon TE2000 inverted wide-field microscope, equipped with a scientific cooled CCD camera (Cascade-II, Photometrics) and a motorised stage (MS2000, ASI). After the field selection which took about 5 min, the acquisition was started and each field was revisited every 15 min, acquiring image z stacks of both the sarcoma cells and the endothelial cells. Stacks of 21 images were acquired with 1 μm z-step using binning 2 which provided a 0.2 μ × 0.2 μm × 1 μm voxel (volume-element) size. Binning refers to the process by which the image size is decreased in relation to the number of binned pixels. Binning 2 (i.e 2×2) increases the sensitivity of the camera and reduces the image size by a factor of 4 [58]. The wavelength of the excitation light alternated between the z stacks using 488 nm for imaging of the sarcoma cells labelled with green fluorescence, and 540 nm for imaging of the endothelial cells labelled with orange fluorescence. The suspended labelled sarcoma cells were introduced into the central aperture of the chamber immediately after the first acquisition time point. The peristaltic pump was then switched on at the second time point, and left to constantly circulate medium. Image stacks were acquired every 15 min for 90 min at each field. Control experiments without flow were performed in MatTek dishes using identical imaging configuration. Paired experiments without flow and with flow were repeated three times for metastatic sarcoma cells T15. Non-metastatic cells K2 were assessed twice under conditions without flow.

3.4 Quantitative measurements

We devised two new measurement parameters which describe the dynamics. The first parameter, Relative Invasion (RI), measures the amount of invasion, i.e the penetration of the monolayer by the cancer cell while the second parameter, Opening Rate of the Endothelial Monolayer (OREM), measures the dynamics of the opening rate of the endothelial monolayer before enduring invasion.

3.4.1 Relative Invasion (RI)

A manual preselection of tumour cells was needed to avoid clusters of cells and interfering debris. A maximum projection of each time point projected the movement and spreading of TCs and indicated a region of interest. The criteria for selection of TCs was that the signal ought to be fairly strong and not too close to other cells which could cause conflict. An area of typically 20×20 μm enclosing TC was used for processing. A graphical explanation is shown in Fig. 3.4.

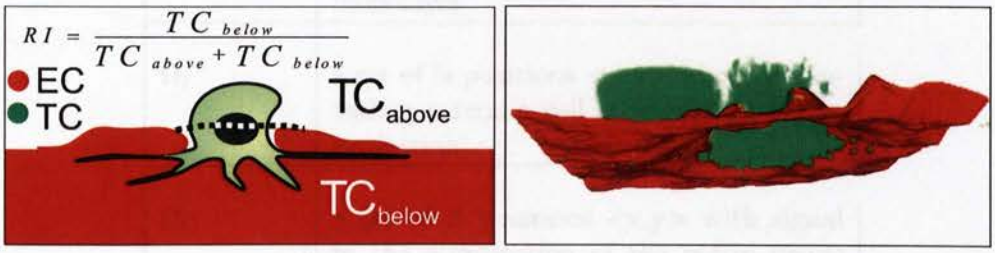

(a) (b)

Figure 3.4: **Graphical explanation of Relative Invasion (RI).** Relative Invasion can simplistically be described as the amount of tumour-cell signal (shown in green) below the EC monolayer (in red) in relation to the tumour-cell signal throughout the cell height. **(a)** An artificially and intentionally created overlay depicted as a dotted line was added as a replacement for missing EC values. **(b)** 3D rendering of the invasion.

RI is defined as the ratio of the volume of the invading cancer cell underneath the upper surface of the monolayer relative to the total volume. Fig. 3.4 helps visualise

the parameter. More formally,

$$RI = \frac{\sum_{<x,y>\in\Omega_I} Proj_I(x,y)}{\sum_{<x,y>\in\Omega_C} Proj_C(x,y)} \qquad with \tag{3.2a}$$

$$Proj_I(x,y) = Max_{z=1}^{U(x,y)}\left(I(x,y,z)\right), \qquad Proj_C(x,y) = Max_{z=1}^{top}\left(I(x,y,z)\right) \tag{3.2b}$$

where Ω_I is a set of N positions <x,y> of an invading sarcoma cell with signal in the z-projection below the upper endothelial monolayer surface U(x,y) and Ω_C is a set of N positions <x,y> with signal in the z-projection of the whole image stack. I(x,y,z) denotes the signal of a 3D volume element (voxel) in the image stack. Table 3.2 summarises the notation.

U(x,y)	the upper surface of the endothelial monolayer
Ω_I	a set of N positions <x,y> where the invading sarcoma cell is present in the z-projection
Ω_C	a set of N positions <x,y> with signal in the z-projection of the entire image stack.
I(x,y,z)	the image intensity of green fluorescence in a voxel. A z value of 1 corresponds to the coverslip surface

Table 3.2: **Notation used in the equations for *RI*.**

The procedure for obtaining *RI* is described in Fig. 3.5. The surface of the

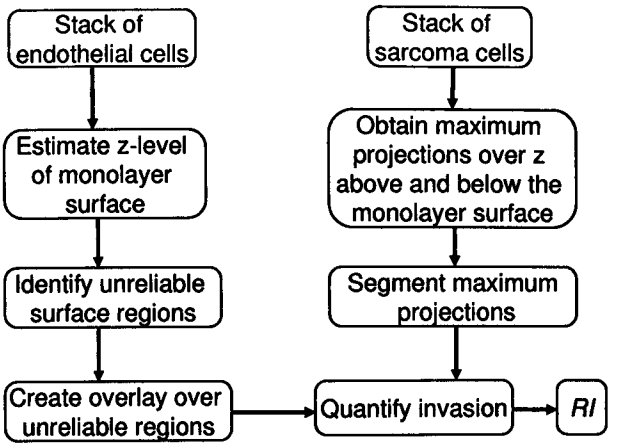

Figure 3.5: **Flowchart of the calculations of Relative Invasion** (RI). The z-levels of the upper surface of a stack of endothelial monolayers were estimated. Some of the regions were weakly labelled or were missing cell signal and produced unreliable readings. The z-levels in these areas were replaced by an artificially created overlay and the relative invasion was then quantified as the amount of sarcoma cell signal below the upper surface of the monolayer in relation to the total cell signal.

monolayer $U(x, y)$ was first established and represented as a depth map. Some of the areas contained unreliable values due to the influence from neighbouring voxels. An artificial overlay based on the surroundings was created to replace the unreliable values with new values. Finally, the mitochondria of the sarcoma cells were segmented ($Proj_I(x, y)$, $Proj_C(x, y)$) which enabled the quantitation.

3.4.2 Opening Rate of the Endothelial Monolayer

A tumour cell tries to disassemble the connection between the endothelial cells once it has adhered. TC induced an opening, large enough for the cell to propel through. The speed of this event is the basis for the Opening Rate of the Endothelial Monolayer $OREM$. To prepare the data for measurement, a minimum projection over z of each time point was obtained and loaded into ImageJ (NIH Image, Bethesda, USA) as images after each other. Each position produced one file (with n time points) and was observed to disclose areas of interest. Once an opening was found, the area of 4×4 μm was selected, centred at the location where the initial opening appeared to be the largest. $OREM$ was measured during invasion by quantifying the fluorescence signal of the endothelial cells in 4 μm $\times$ 4 μm areas where invasion commenced. Fig. 3.6 depicts the fixed window and the corresponding change in the monolayer over time. The size 4×4 was determined to be - in our experience - the average size of the initial opening. The location of an area was selected manually for each cell and remained the same over time. Once the positions were found and recorded, the procedure was automated in Matlab. A flowchart of the procedure is found in Fig. 3.7. The signal was measured from the minimum projection of the image z-stacks of monolayer cells for each time point. The sarcoma cell-induced opening in the monolayer resulted in a decrease of signal values over time in the selected areas of the minimum-projection images. However, the procedure included multiple acquisitions which introduce photo-bleaching. The effect of photo-bleaching is a rapid decrease in cell signal and, in the worst scenario, the cell signal is eliminated. The photo-bleaching in these experiments was limited because of short exposure time and therefore did not have a serious impact.

The intensity of the projection images I was normalised (Eq. 3.3a) over the

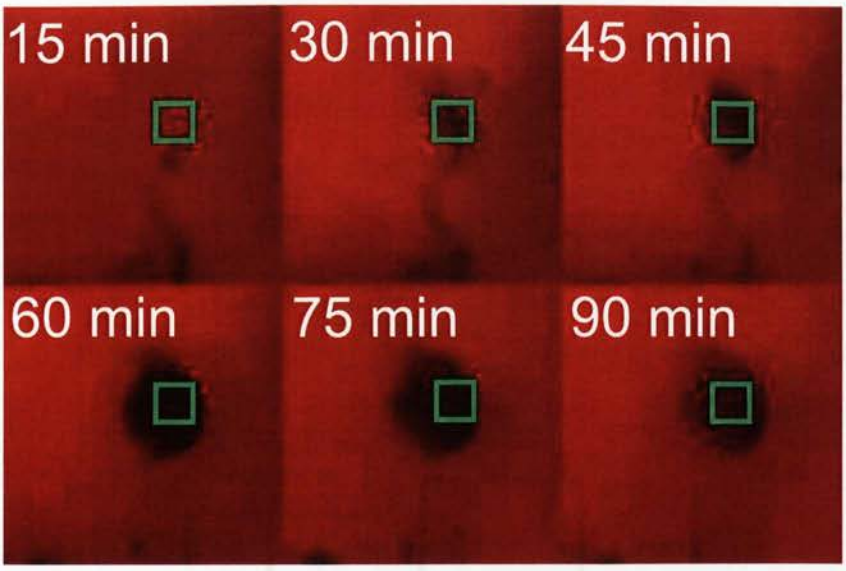

Figure 3.6: **Illustration of the calculations of OREM.** The minimum projection of monolayers (shown in red) at each time point was obtained to provide evidence for early openings. The estimation of the opening rate was performed in a predefined window, shown in green, of 4×4 μm (21×21 pixels) at a fixed location during the entire observation period. The position of the window was selected where the opening between 0-30 min was the largest. *OREM* was then calculated as the difference in monolayer signal within the window between 0-30 min but normalised over the observation period. A difference in cell signal can be seen inside the window between the mentioned time points. The normalisation, the predefined window size and the fixed location of the window made the parameter comparable between experiments. The intensity of the monolayers was adjusted for visualisation purposes.

monitoring period of 90 min and thus comparable between repeated experiments. The intensity was then automatically monitored over the time points and the normalised rate at which the intensity decreased revealed the speed of the opening (see Fig.3.7).

$$I_{norm} = \frac{I(t) - min(I)}{max(I) - min(I)} \tag{3.3a}$$

$$OREM = I_{norm}(t_1) - I_{norm}(t_2) \tag{3.3b}$$

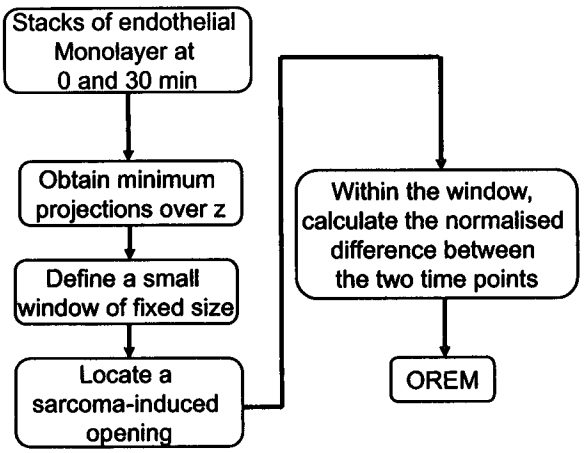

Figure 3.7: **Flowchart of the steps to obtain OREM.** *OREM* can be seen as a measurement of how quickly the signal disappeared in a small defined, fixed region, typically $4 \times 4\mu$m. The region (window) was applied to the minimum projection of a monolayer stack. The normalised rate at which the signal faded between 0 and 30 min constituted the parameter *OREM*. Because the rate is normalised using the maximum opening over all time points it is possible to compare the rate between different cells and experiments.

3.4.3 Relative spreading

A tumour cell may also spread laterally while exposed to shear. In order to assess this property, we developed Relative Spreading (RES) which quantified the relative spreading below the monolayer surface. The spreading was estimated by calculating the area of an ellipse fitted to the segmented points. Firstly, a reference fit (see Fig. 3.8) was obtained which utilised the segmented point in a projection of all time points (see Fig. 3.8). This meant that all the segmented pixels over all time points for a particular cell formed a set on which the fitting was applied. The area of the reference fit was divided by the area found in each time point, which created a relative unit comparable between different cells.

The implementation utilised Matlab's vitelline function [5] and the spreading was defined as the area of the ellipse. The relative spreading was more formally defined as

$$RES = \frac{A_{tp}}{A_{ref}} \tag{3.4}$$

where A_{ref} symbolises the area of the reference fit and A_{tp} the area of a fitted ellipse at a single time point. An example of a reference fit and a fit from an individual time point is shown in Fig. 3.8.

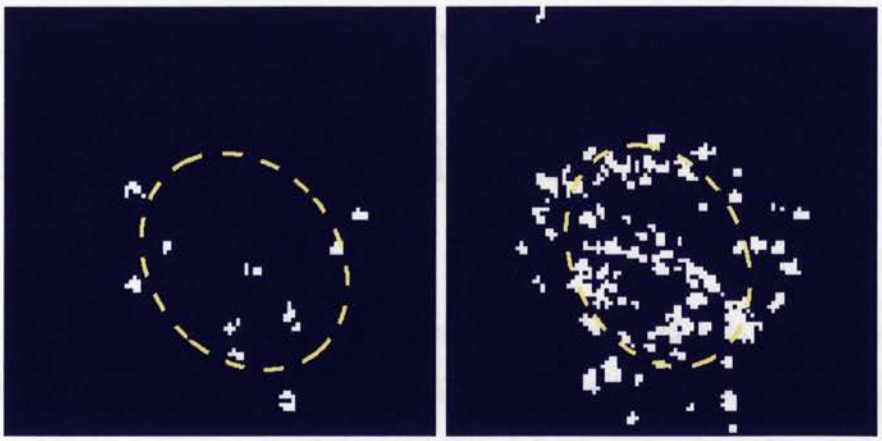

(a) (b)

Figure 3.8: **Example of ellipses which defined Relative Spreading.** The area of an ellipse fitted to the segmented pixels was calculated for each time point. This area was divided by the area of the reference fit which was calculated as the area of the ellipse fitted to all the segmented pixels over all time points. Relative spreading can thus have a quantity >1 because it was possible that the reference fit was smaller due to a higher amount of segmented pixels. **(a)** An ellipse fitted to the segmented pixels found at a single time point. **(b)** A reference fit for a cell.

Chapter 4

Surface reconstruction of endothelial monolayers

TCs have an ability to invade into monolayers of endothelial cells and the proposed method to quantify this behaviour was defined as Relative Invasion (RI) according to Eq. 3.2a. This property required the location of the upper surface $U(x, y)$ (Eq. 3.2b) of the monolayer plus the location of the sarcoma cell signal. In order to achieve this, the upper surface was reconstructed from a 3D stack and represented as a 2D depth map. However, some values in the depth map could not be trusted, because TCs induce openings in the monolayer which leave areas with no or little cell signal. These regions needed to be identified in order to create a covering so that RI could be estimated. This chapter describes methods for finding the upper surface $U(x, y)$, identification of invaded regions and the interpolation over these regions.

4.1 Finding the upper surface

Research has been conducted through the years to investigate cancer metastasis and the interaction between cancer cells and endothelium. Sarcoma cells have a good ability to penetrate the endothelium and metastasise [74]. A key role in investigating this behaviour was to look at the EC surface as it could contain vital clues to the migration. The approach to estimate the EC surface denoted as $U(x, y)$ in Eq. 3.2a stems from the field of geography where, for example, the ocean floor is represented as a depth map [75]. The techniques to acquire the depth values may differ but the principles are similar. The following sections explore ways to recover depth values from a blurred stack of images.

4.1.1 Maximum intensity

A fluorescently labelled cell emits light when excited to a certain wavelength. The strength of the signal at each z-level indicates the position of the cell within the volume. A strong signal (i.e. a peak in light from fluorescence molecules) indicates at which z-plane the cell is located. This could be utilised in terms of finding the local position of a cell surface over z. In order to achieve this, the z-level that contained the highest intensity was found for every $< x, y >$ position. Fig 4.1 shows examples of intensity curves. One of them (Fig. 4.1(a)) stems from a strongly labelled region of the cell which results in a sharp peak around the z-level where the surface is located. On the other hand, a weakly labelled region (Fig. 4.1(b)) has high intensity values toward the start- and endpoints of the curve and a minimum in-between. This behaviour is influenced by its neighbouring voxels. Each voxel emits fluorescence light in every direction which affects the neighbouring voxels. The maximum interference is when a voxel is out of focus and the minimum is when it is in focus. Because a

weakly labelled region emits little light of its own, most of its light originates from its neighbours. Therefore, the z-level of the minimum intensity value in Fig. 4.1(b) indicates the surface location of its neighbours and the high intensity values indicate where those are out of focus rather than the surface position.

Using the z-level of the maximum intensity value as an indication of the surface position works well with strongly labelled cells where the intensity plot over z contains a major peak. Problems arise when the cell labelling is less defined and the cell signal is influenced by its neighbours. The z-level of the maximum intensity value in those situations represents a region where the neighbours are out of focus. A solution to this problem would be to have a levelled surface and uniform cell labelling. This is unfortunately not practically feasible because the cells are not uniform and some cells will absorb more of the fluorescence than others.

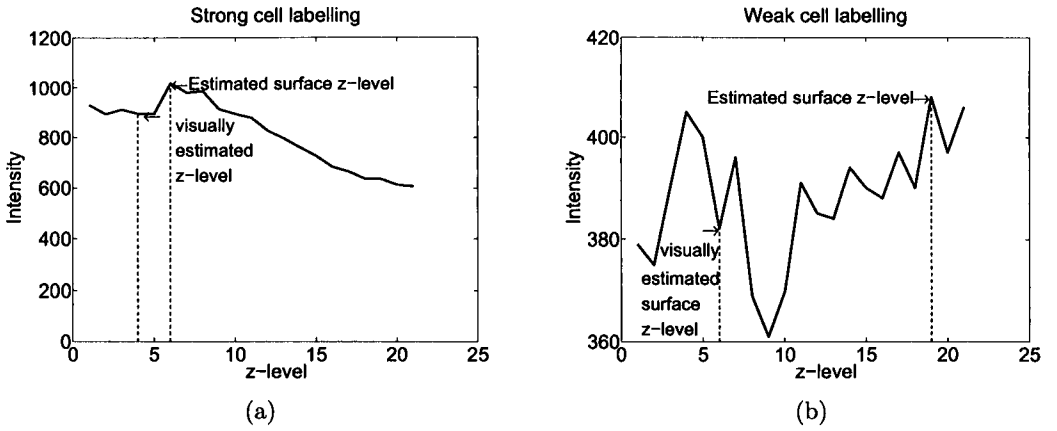

Figure 4.1: **Examples of intensity curves of strongly and weakly labelled areas.** The intensities for two different <x,y> positions were plotted as connected data points over z. The strongly labelled position exhibited a sharp peak in intensity around the surface z-location. The weakly labelled position portrayed high intensity values towards the start and end of the curve and low in-between. The fluorescence in this position was low and therefore most of the intensity values stem from blur originating at its neighbours. The z-level of the minimum intensity indicated where those were in focus and the z-level of the maximum intensity indicated where most of those were out of focus rather than the surface level. The visually estimated z-levels were subjectively found by manually scanning through the image stack for the z-level which contained the sharpest region for each position. **(a)** shows the intensity curve for a strongly labelled position. The z-level of the maximum intensity was close to the visually estimated level ($z = 6$ and 4 respectively). **(b)** shows the intensity curve for a weakly labelled position. The manual surface estimation and the z-level of the maximum intensity were different ($z = 6$ and 19 respectively). This was because of the interference of blur from neighbouring voxels.

4.1.2 Maximum gradient

The image acquisition introduced blur and noise, which made accurate evaluation of the cell interaction difficult. We are interested in the EC surface fluorescence signal and thus we introduced a surface detection technique which described the upper of the EC and aided accurate measurement and visualisation of its exterior properties.

The proposed method to restore the EC surface was based on the gradient and uses the principles of autofocus. A z-stack of ECs is acquired in a top-to-bottom fashion and the Sobel gradient was calculated plane-by-plane. An average filter of 11×11 pixels was applied on each plane separately.

The average gradient value for each plane produced a curve which could be used to determine the in-focus z-plane. In addition to identifying the surface location, we were also able to determine the location of the coverslip by investigating the z-plane where the slope of the gradient curve was steepest. The cell was located above the coverslip and any information below was therefore redundant. This helped to reduce the complexity of the calculations. A typical mean gradient curve is shown in Fig. 4.2(a).

Identifying the location of the surface using mean values of the gradient over z was a new approach designed to estimate the z-position of the endothelial surface. A natural approach would be to use the maximum value which, by inspecting the global gradient, seemed to be a good choice. The image was in focus where the gradient had its maximum. However, the larger the averaging area was, the smaller the interference from the noise. On the other hand, if no filtering was used, the locality would be sustained but then influenced by noise as seen in Fig. 4.2(b) and Fig. 4.2(c). Therefore, a balance was needed in order to keep the localisation and still suppress the noise.

The selection of an average kernel of 11×11 pixels was made and used in the calculation of RI. Fig. 4.2(b) and Fig. 4.2(c) showed that noise could influence the estimation of the surface levels and these errors could be prevented by applying an average filter.

The amount of smoothing highly depends on the data set. The image quality of a data set can easily vary between experiments and may influence the specific decisions initially made concerning the kernel size. Smoothing each plane within the stack with an 11×11 pixel kernel and then finding the maximum gradient value over z for each pixel to locate the monolayer surface was used successfully in these experiments. Chapter 6.2 evaluates the accuracy of the estimation in detail.

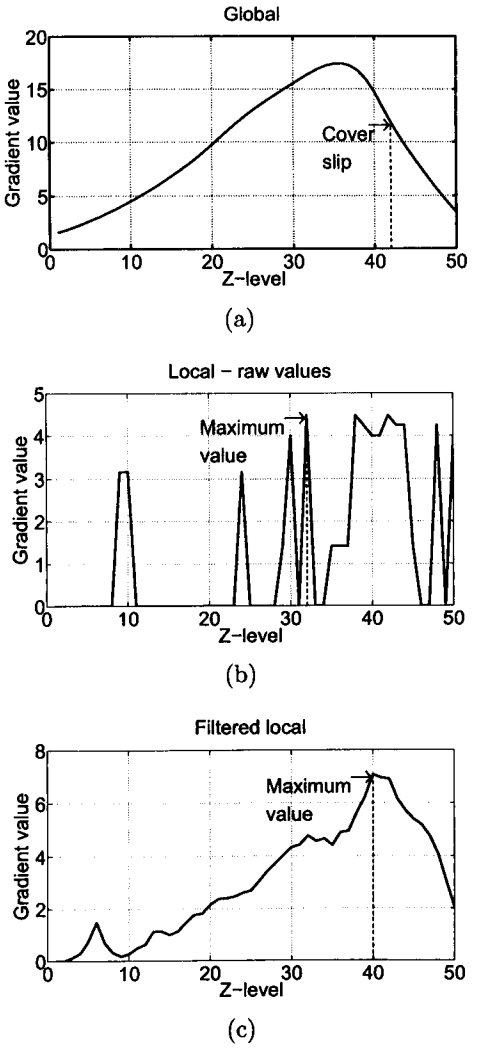

Figure 4.2: **Examples of gradient curves obtained from a blurred stack.** The average gradient value using the Sobel operator was calculated for each plane and plotted as connected data points. The maximum gradient value indicated at which z-level the focus was located. A z-level of 1 represents the top of the stack. The three figures together indicate that the curve needed to be in a local context and filtered with an average filter in order to produce an accurate estimation. **(a)** represents a gradient curve where each data point represents the average gradient value for a plane. The in-focus plane was found at z=35 (maximum gradient value) and the coverslip was found at the position where the slope was steepest, indicated by the dashed line (z=38). **(b)** a raw gradient curve without smoothing for a single pixel over z. Dotted line represents the focus position at z=36. This curve did not undergo any smoothing to remove noise. The peak at z-level = 31 was due to noise. **(c)** a gradient curve filtered with an average kernel of 11×11 pixels. The noise was now suppressed and the accurate surface location was revealed as the z-level where the gradient had its maximum at z=40. Manual inspection confirmed this surface position.

4.1.3 Correlation

The maximum gradient estimated the local surface position axially. As an alternative, the correlation coefficient between two consecutive windows was deployed axially in a similar fashion. The correlation coefficient is defined in Eq. 4.1 and in the 2D case, correlation coefficient r represents the strength and linear relationship between two matrices A and B.

$$r = \frac{\sum_m \sum_n (A_{mn} - \bar{A})(B_{mn} - \bar{B})}{\sqrt{\left(\sum_m \sum_n \left(A_{mn} - \bar{A}\right)^2\right)\left(\sum_m \sum_n \left(B_{mn} - \bar{B}\right)^2\right)}} \tag{4.1}$$

In order to make an estimation of the surface, the correlation coefficient was calculated on the gradient image between two windows of the same $< x, y >$ position but on consecutive z-planes. In this application, a positive factor indicated that both windows had an increasing gradient relative to their respective window average. The theory was that the gradient was stable in the focal plane and that this would be expressed as a high correlation between two consecutive z-planes with a peak at the assumed focal plane. The coefficient expressed a low value in the presence of noise due to the randomness of it. As the calculations progress over the z-planes, the slices became sharper and thus increased gradient values also resulted in an increased coefficient.

However, for a blurred stack, the values did not display a dominant peak because of the blurring, which stretched the information out over neighbouring planes. This resulted in a range of z-slices with high correlation values as seen in Fig 4.3. The depth map, which was the result of the calculations, contained a very wide range of values which did not produce reliable results. Therefore, the correlation coefficient did not provide a unique location of the in-focus position.

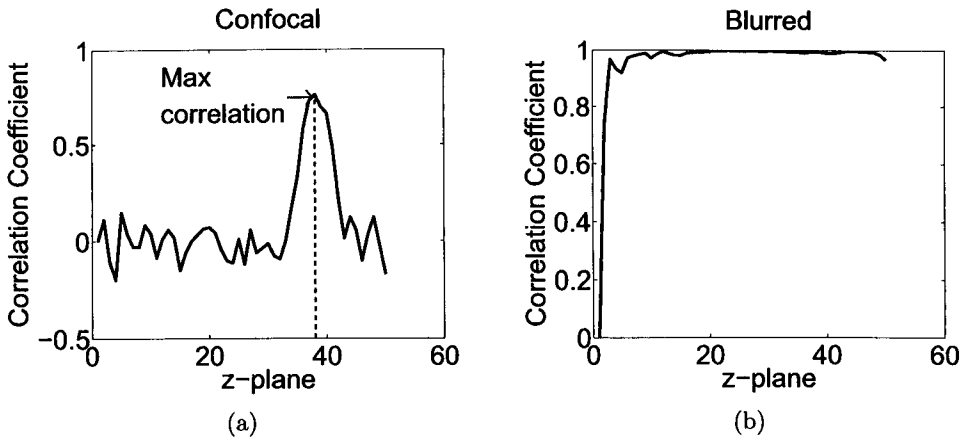

Figure 4.3: **Example of graphs with correlation values obtained from gradient images acquired with a confocal and a wide-field microscope.** The correlation coefficient was calculated between two 11 × 11 pixel windows of consecutive z-planes. The Sobel gradient was calculated prior to obtaining the correlation values. **(a)** Correlation values obtained from a confocal stack. The correlation between two windows expressed a sharp peak at the in-focus position and low values towards the sides. **(b)** Correlation values obtained from a confocal stack, convolved with a PSF to simulate wide-field conditions. The correlation between two windows was believed to increase to a sharp peak at the in-focus position, which was not the case. Instead, the high values were contained in a broader spectrum of z-planes where the sharp peak was smoothed by the blur.

4.2 Identification of unreliable monolayer regions

Identification of openings in the endothelial monolayer is an important step in the surface reconstruction and the quantification of cancer-cell invasion. The surface reconstruction is based on the location of the maximum gradient value of the monolayer. However, in some instances, these readings are false and contain misleading values especially in the invaded areas with no signal. The purpose of the identification was to locate regions where such events occur. These regions were usually characterised by low signal intensities due to a poorly labelled surface or openings with no cell surface. During such instances, the intensity in the current voxel was influenced by neighbouring voxels being high. Some of the problems are shown in

Fig. 4.4. The areas indicated with arrows were examples of dark regions with little cell signal, where the gradient might be unreliable. The identification process was aimed at establishing a method to find these positions and to exclude their gradient values from the surface estimation. Identification of areas with low signal would consist of true openings with no cell signal but also areas with very weak labelling, influenced by blur. Applying the maximum gradient approach on those areas would create a surface that was not truthful and resulted in a level of invasion that may not exist. Identification of unreliable regions solved this problem by excluding any doubtful areas but only worked with sets that were thought to contain cell signal. Segmenting these areas using the histogram seemed to be a good choice since weakly labelled areas were dark and cell signal was bright. In order to explore this, Otsu's segmentation algorithm was applied on a minimum projection image of EC together in order to evaluate histogram-based segmentation.

The manual segmentation seen in Fig. 4.4 was based on the corresponding histogram which exhibits three modes representing the shift in brightness from left to right in Fig. 4.4(a). The manual threshold was not selected at any of these modes but rather before the first peak. The reason was that some of the intensity values located on the edges of the cells were somewhat darker than the intensities representing the first mode. Otsu's method, for example, tries to maximise the within-class variance of each group and the selected threshold was located to the right of the first peak as seen in Fig. 4.4(d). Applying Otsu technique would require that the two groups were fairly well separated. This criterion could not always be met, because the cell labelling procedure did not always deliver an image where the cell signal was very different from the background.

Approaches exist, mainly in Magnetic Resonance Imaging (MRI), to identify certain regions, for example in the brain. This could be translated into the identification

of reliable and unreliable regions among EC monolayers. The unreliable areas would consist of openings mainly introduced by TCs but also areas the monolayer did not cover. However, the approaches in MRI assume some kind of prior knowledge of shape [76] or appearance [77] of the regions and require a training set which will be used as reference examples and specify an average set of shape or appearance. To identify certain features, the new image with unknown features acquired at different times and of different subjects is then compared with the training set, and there is a match if the new, acquired image is similar to those in the training set. It would be adequate if this could be applied to unreliable regions but this idea is not applicable in cancer-cell invasion due to the fact that the monolayer is highly dynamic and can easily change shape and appearance between fields of view. Also, TCs invade the monolayer in pseudo-random fashion in the sense that the shape of the opening and the method by which they invade changes with the individual TCs. For example, white blood cells have been shown to exhibit different modes of invasion such as transcellular (through cells) [78] and paracellular (cell junctions) [79] and it can be assumed that TCs have similar behaviour [80].

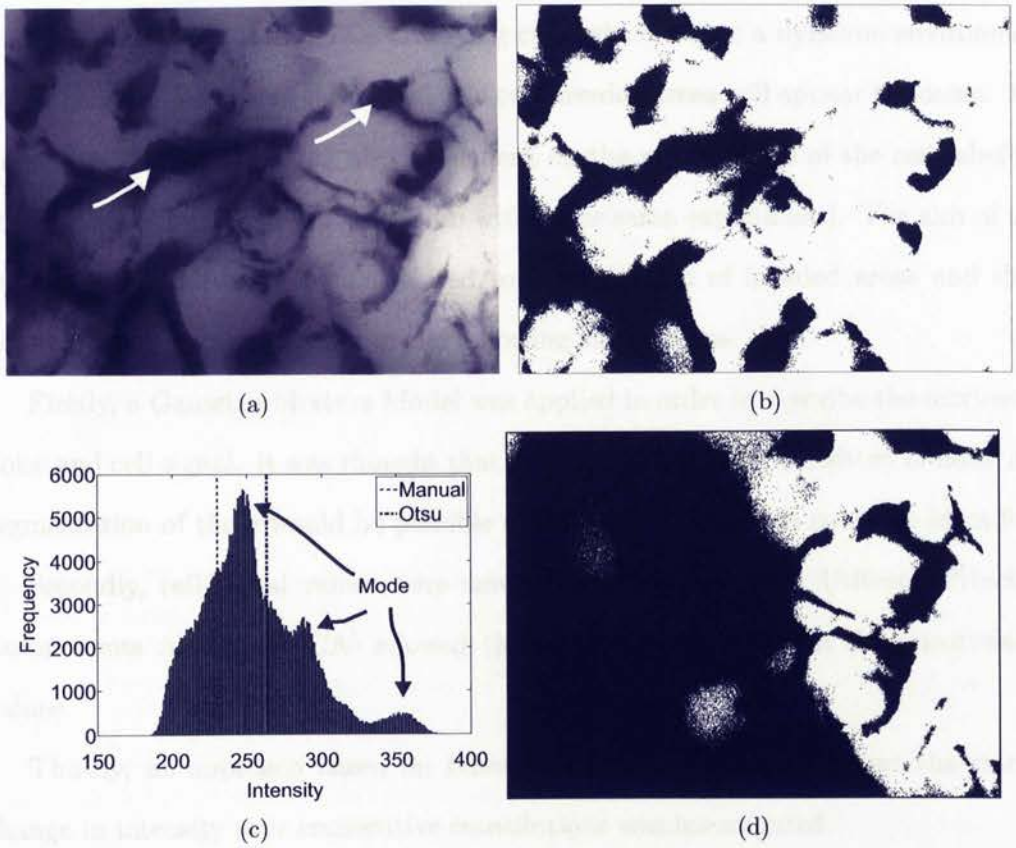

Figure 4.4: **Example of segmentations of a minimum projection obtained from a stack of an endothelial monolayer using thresholding.** The minimum projection emphasises the dark areas, which highlighted areas with low intensity. **(a)** Minimum projection. Arrows indicate examples of regions with low intensity which may cause problems. **(b)** Segmented result of (a) after applying the manually obtained threshold. **(c)** Histogram of the minimum projection. Arrows indicate the three different stages (modes) of brightness seen from left to right in (a). Dashed lines represent the manually selected threshold used to produce (b) and (d) respectively. **(d)** Segmented result after obtaining a threshold using a standard method (Otsu [1]).

So far, no study has addressed the identification of invaded regions with low signal among endothelial monolayers, partly because objective evaluation of invasion has not yet attracted interest. Some of the problems arising in segmenting invaded areas are the fact that the ECs and TCs are living cells which create a dynamic environment where each cell acts as an individual. No two invaded areas will appear the same. The intensities in each stack are also dependent on the performance of the cell labelling which varies from stack to stack (even within the same experiment). The aim of this section is to address problems related to segmentation of invaded areas and show possible solutions. Details are in the following sub-sections.

Firstly, a Gaussian Mixture Model was applied in order to describe the mixture of noise and cell signal. It was thought that invaded areas mainly consisted of noise and segmentation of these would be possible if the noise distribution could be identified.

Secondly, cell signal values were assumed to be correlated. Utilising Principal Components Analysis (PCA) allowed these to be extracted from the uncorrelated values.

Thirdly, an approach based on Linear Diffusion was applied where the rate of change in intensity over consecutive convolutions was investigated.

4.2.1 Gaussian Mixture Model

Noise is a frequent source of errors in microscope images. In fact, it is inevitable due to noise such as electronic noise and photon noise [2]. This can cause an image to contain artifacts and be a source of false measurements. It is therefore important to handle the noise in a correct manner. The noise in a wide-field microscope system is usually Poisson distributed [2]. A Poisson distribution can then be turned into a Gaussian distribution via the Central Limit Theorem.

The Central Limit Theorem states that values from any distribution can be ap-

proximated with a Gaussian distribution provided there are enough samples [3]. The noise distribution from a wide-field microscope, shown in Fig. 4.5, displayed a Gaussian shape. Unreliable areas were believed to contain noise plus some signal which could be modelled with a gaussian mixture. A stack with no cells, containing noise only, was used to estimate the distribution parameters of the noise.

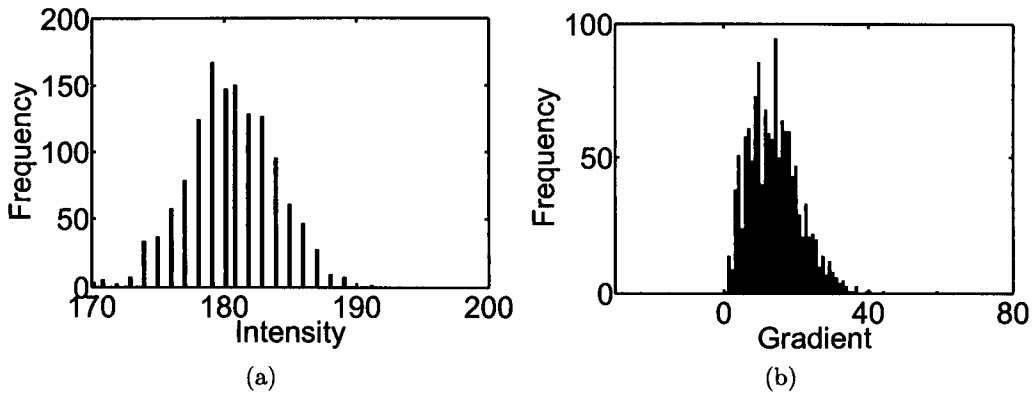

Figure 4.5: **Histograms of a stack with no cells (only background noise) obtained with a wide-field microscope.** The noise in a microscope is usually described as being Poisson distributed [2]. Because a point in a wide-field system is influenced by every other point through diffraction and interference, the Central Limit Theorem [3] approximates the distribution to a Gaussian distribution. The stack contained 520×696 pixels over 76 z-slices (although the histograms shown represent a volume of 11×11×11), with resolution 0.2×0.2×0.2μm/px. Exposure time: 60 ms, binning 2×2. **(a)** The intensity distribution of a sub-volume of the acquired noise. **(b)** The gradient distribution of a sub-volume of the acquired noise.

Invading cancer cells disassemble endothelial cell junctions in their strive to extravasate through the monolayer. The points of invasion are characterised by low signal values and noise because TCs created holes which decreased the endothelial cell signal. A microscopic image with no cell content generally contains noise and forms the basis for the cell signal segmentation using Gaussian Mixture Models (GMM). A cell stack consisted of three types of signal: cell signal, blur and background noise. The blur exhibited smooth characteristics and was suppressed by a

high-pass filter. The result after high-pass filtering could be described by a mixture of two Gaussians: signal and background noise. The distributios from the two groups would overlap each other in different measures depending on the strength of the signal (see Fig. 4.7). The Expectation-Maximisation algorithm is a method to estimate parameters of mixtures of Gaussians [81], i.e. the parameters of each distributions within the mixture. The parameters of the noise part of the distribution would then be compared to the parameters of a measured, acquired stack consisting of noise only.

The endothelial layer usually occupied a very small number of slices inside the stack and, therefore, noise and out-of-focus blur would dominate the distribution. To limit the effect of blur and prevent it from completely dominating, only the 10 z-levels (out of 101 in total) above the coverslip were considered. The pre-processing step consisted first of filtering each plane of the stack with a high-pass kernel (i.e. gradient). This removed blur derived from out-of-focus information which had smooth characteristics. The gradient suppressed the intensities of blur which allowed the signal with higher frequencies to stand out. The blur thus showed low gradient values compared to signal. A gradient stack can then be described as

$$G = G_s + N \tag{4.2}$$

where G is the gradient values, G_s represent signal part and N the noise part. The gradient was filtered subsequently with an average kernel to suppress the noise such that

$$G_f = G \otimes h \approx G_s \tag{4.3}$$

where G is the gradient, h is an average kernel, G_f the filtered version of the gradient and $\otimes$ represents convolution. It could now be assumed that the noise was mainly suppressed and the only remaining values were signal and therefore $G_f \approx G_s$.

Subtracting Eq. 4.3 from Eq. 4.2 and assuming that Eq. 4.3 only contained signal resulted in some noise plus residual signal as shown in Eq 4.4

$$G - G_f = \quad G_s + N - G_s \quad = N + \rho \tag{4.4}$$

where ρ is the residual signal. Fig. 4.6 shows examples of how the noise and residuals in Eq. 4.4 changed between areas with signal and unreliable monolayer regions.

The average filter of 11×11 pixels was deployed on a plane-by-plane basis to suppress the noise and the difference between the original gradient G and the filtered version (G_f) of the same stack was also made plane-by-plane. The next task was to separate the noise from the residual signal and compare the noise distribution with the measured noise. The measured noise was obtained by acquiring an empty stack with no cells.

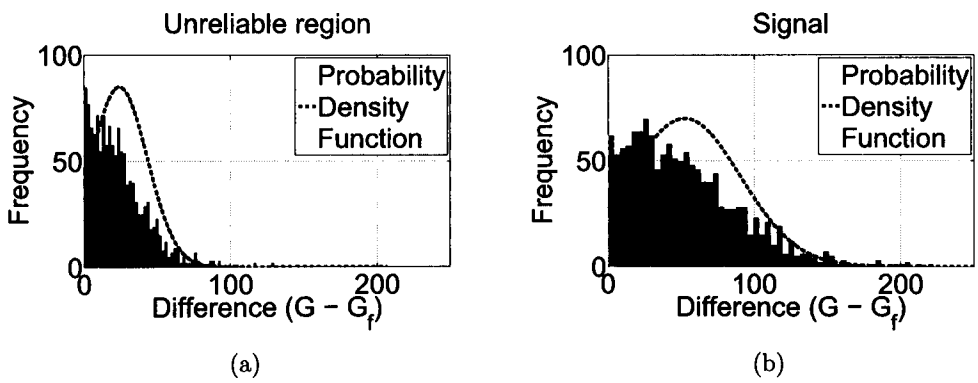

Figure 4.6: **Histogram of a stack of size 11×11×11 pixels containing the difference between the gradient values of a stack of a monolayer and a filtered version of itself.** The gradient for each plane was calculated (denoted by G in Eq. 4.2). An average filter of 11×11 pixels was applied on a plane-by-plane basis to suppress the noise (G_f in Eq. 4.3). The difference between the two ($G - G_f$) is displayed as a histogram which represents the noise plus some residual gradient signal. The histogram in (b) has a wider distribution because the residual signal located in the upper segment of the histogram was stronger. **(a)** Histogram of an unreliable area. **(b)** Histogram of signal (reliable area).

Fig. 4.8 shows the histograms with the two distributions superimposed. The E-M algorithm implemented in Matlab [4] was deployed in order to separate the noise and the cell signal. The 11×11×11 pixel window of the difference stack was reorganised into one dimension before applying E-M. The number of z-slices was limited to 10 above the coverslip due to the fact that the surface is very thin in comparison to the entire range of the stack. If the full range was included, the noise would always be dominant and separation between the two classes would be impossible.

A region was classified as unreliable if the variance of the noise part was less than the variance of the measured noise. The choice of threshold was selected to σ^2 i.e. the variance of the class with the lowest mean had to be $<$ variance of the measured noise. The reasoning behind the choice of variance in favour of standard deviation is that the difference stack was calculated in the presence of monolayers. The out-of-focus signal would then increase the standard deviation as it added high values to the histogram. Instead, if the variance is used, the effect is limited since the thresholds are squared, bringing the values into similar range. An example of segmentation using GMM is shown in Fig. 4.8.

One of the problems with this method is that the sensitivity to disturbances in cell signal is high. The performance of the labelling technique is crucial for this approach. An example of excellent surface definition is found in Fig. 4.8. The details of the surface are well exposed and little excess fluorescence is present. However, if the fluorescence molecules would not adhere thoroughly at the intended positions inside the cell, the amount of fluorescence noise would increase and change the intensity distribution. The consequences would be that the threshold changes depending on the fluorescence, noise which limits the applicability of the method to single experiments. During long-term experiments, the intensity of the laser causes the fluorescent substance to decrease. As a result, the intensity also changes (a.k.a. photo bleaching).

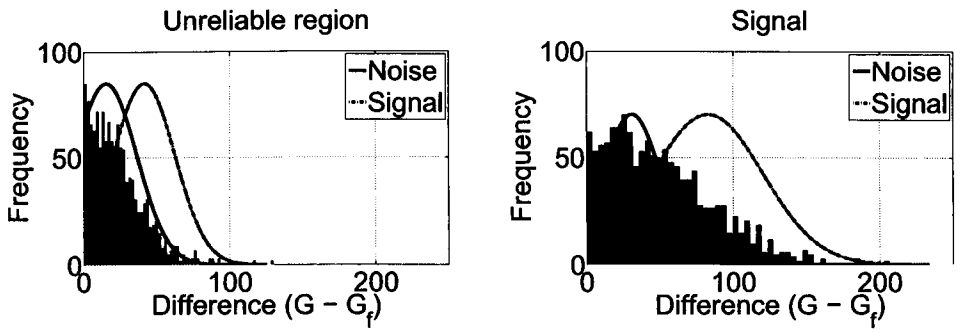

(a) (b)

Figure 4.7: **Histogram with the two mixtures superimposed.** The difference was separated into two clusters using the EM algorithm [4]. A window was classified as unreliable if the variance of the cluster with the lowest mean was < the variance of the measured noise. **(a)** Histogram of an unreliable region. **(b)** Histogram of a more reliable region.

The bleaching is dependent on the intensity of the laser and the length of exposure. The surface labelling (see section 7.1.2), however, produced extended photostability and excellent surface definition during prolonged exposure.

The identification of unreliable regions using GMM was based on the EM algorithm which was applied for every (x, y) over the range of 10 z-slices above the coverslip ($11 \times 11 \times 10$ values). It works well for stacks of images which are acquired with long exposure time and short distance between the z-planes. However, for more noisy image stacks, typically caused by faster acquisition, the noise would be over-represented and all areas classified as unreliable.

4.2.2 Principal Components Analysis

Principal Components Analysis is a common technique in image analysis and this approach has previously been applied to image compression, where regions with similar characteristics (based on the histogram) share the same principal components. For

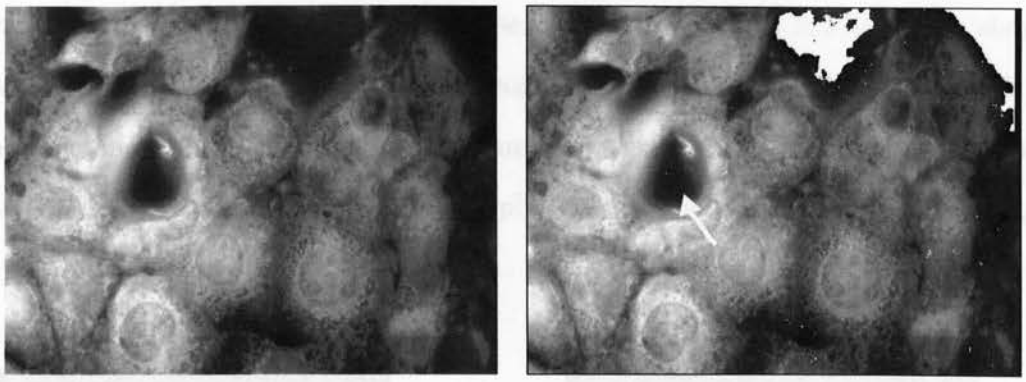

(a) (b)

Figure 4.8: **Example of segmentation of unreliable regions in a monolayer using GMM.** The segmentation was based on separating the Gaussian-like noise from the signal. The noise was obtained by calculating the difference between the original intensity stack and a filtered version of itself. The EM algorithm was applied on 11×11×11 pixel substacks with two classes: signal and noise sourced from the difference. The variance of the separated noise (i.e. the variance of the cluster with the lowest mean) is compared to the variance of an empty stack containing noise only (reference sample). A region was classified as unreliable if the variance of the separated noise < variance of the measured. The size of the original stack containing cell signal was 520×696×101 voxels with resolution 0.2×0.2×0.2μm acquired five hours into the experiment. **a)** Original in-focus plane. **b)** Segmented result. The white areas represent unreliable regions and are superimposed on the in-focus plane. The white arrow indicates an invaded area but correctly segmented as cell surface. This region was actually covered but invading TC forced the surface outside the in-focus plane.

example, Taur *et al* [82] applied it to the coding of medical images and suggested that signal intensities from the same kind of regions in the image are likely to be in the same intensity range. These regions can be classified and each group will share the same Principal Components (PCs) and can therefore be reused. Sychra *et al* [83] had similar ideas and investigated the noise found in MRI images, deriving a noise suppression scheme where the noise and signal were separated by different PCs. The noise could be reduced by using only a subset of the PCs.

The segmentation of unreliable regions in EC stacks proposed here is derived from these theories. It is assumed that similar regions share similar characteristics

and it was shown that the noise in these microscopic images has Gaussian shape (see section 4.2.1). The cell signals are somewhat correlated, unlike noise, which is random, and cell signal values would occupy the first few PCs while noise populates latter PCs. An example of an eigenimage plus manual segmentation of the eigenimage is shown in Fig. 4.9.

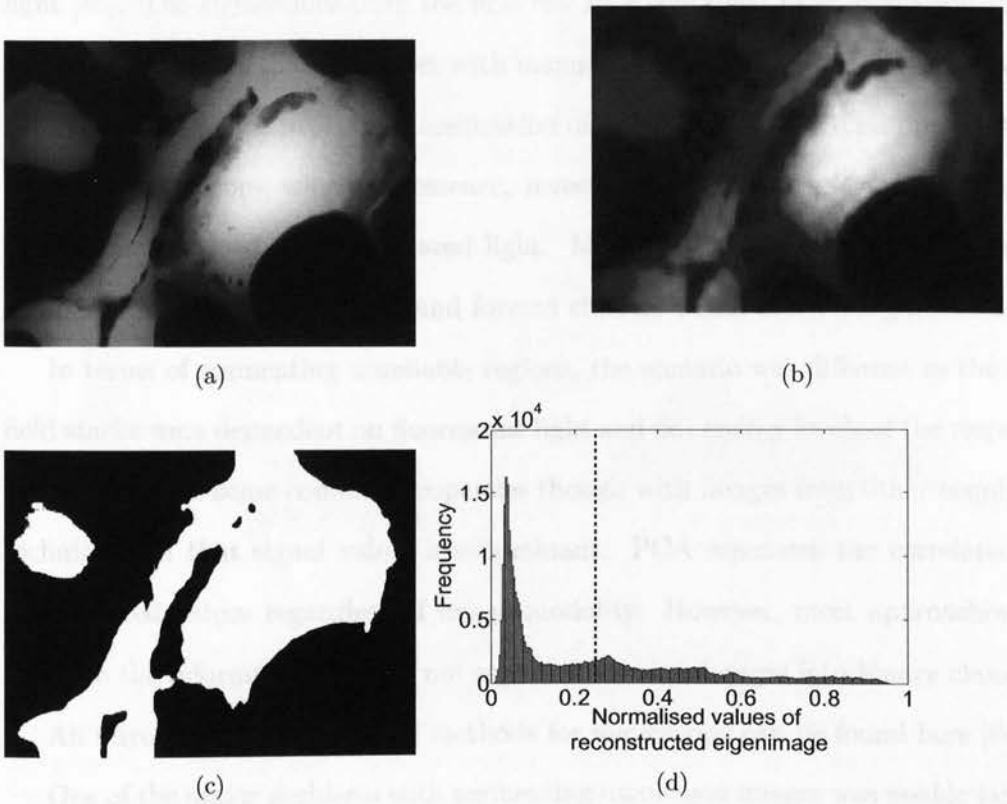

Figure 4.9: **Segmentation of endothelial monolayer using Principal Components Analysis (PCA).** Eigenimages of endothelial monolayer are obtained through PCA and the hypothesis is that cell signal values are correlated and will therefore occupy the same range of PCs. **(a)** Minimum-intensity projection. **(b)** Eigenimage reconstructed by using the first 16 PCs only representing 99.6% of the information. **(c)** Segmented result of (b). The threshold was manually set to 0.25. **(d)** Histogram of the eigenimage shown in (b). The dashed line represents the subjectively and manually selected threshold of (b) to obtain the segmented result in (c). Threshold was set to 0.25.

Pedersen *et al* used this fact to separate objects in positron emission tomography

images [84] which used radioactive labelling where the objects of interest were contained in separate PCs. The images were corrupted by noise and PCA revealed that the objects of interest could be separated from the noise by retaining the first few PCs. This approach is also used in another study for initialisation of the kmeans algorithm to distinguish cancer and non-cancerous tissues using microscopy with infrared light [85]. The eigenvalues from the first few PCs contained most significant signals and formed clusters that - together with manual inspection of the tissue - represented the two classes which provided classification of cancerous tissues. This approach uses Raman spectroscopy which, in essence, investigates the energy levels a sample returns when exposed to e.g. infrared light. Malignant tissues responded differently compared to surrounding tissue and formed clusters which aided a segmentation.

In terms of segmenting unreliable regions, the scenario was different as the wide-field stacks were dependent on fluorescent light and not energy levels of the respective tissue. It shares some common properties though with images from other acquisition techniques in that signal values are dominant. PCA separates the correlated and uncorrelated values regardless of image modality. However, most approaches only separate the information and do not segment the eigenimages into binary classes.

An introduction to statistical methods for microscopy can be found here [86].

One of the major problems with segmenting monolayer images was weakly labelled areas due to poor attachment of fluorescent molecules which give rise to lower intensity values. Segmenting these using the histogram does not work due to overlapping areas between the groups, but PCA has been shown to address this issue. This approach targets this issue because signal values are correlated and PCA groups correlated values into the first few PCs. The more correlation there is, the better segmentation [83]. One can question, though, the quality of these readings in terms of gradient values and surface estimation. The purpose of segmenting the monolayer was to

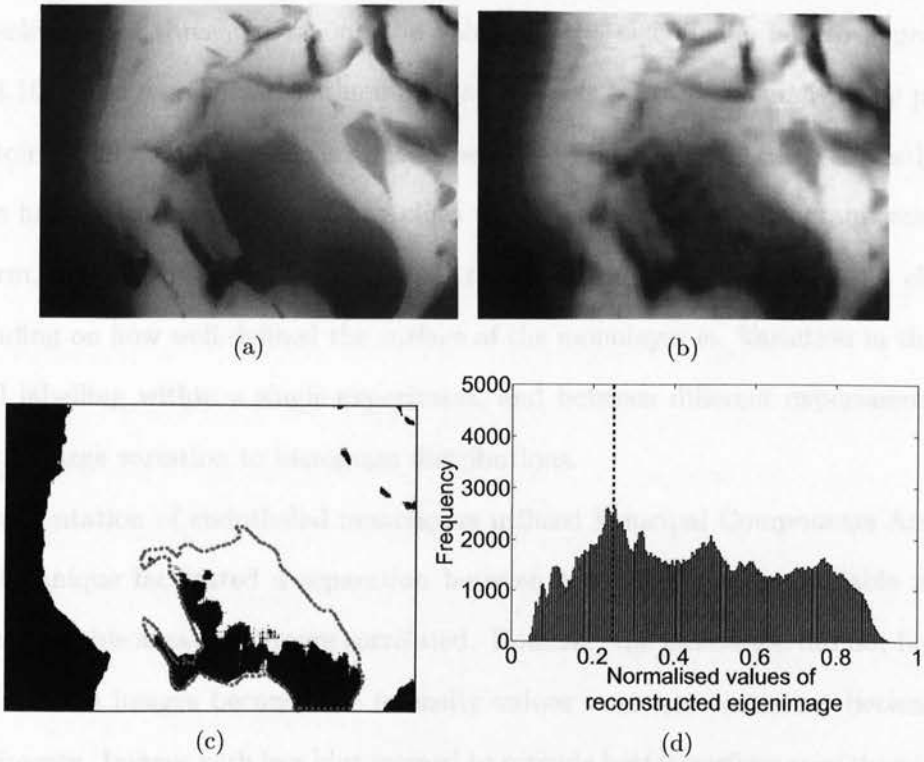

Figure 4.10: **Example of segmentation of a monolayer using PCA.** The minimum projection was transformed into an eigenimage using the first 16 PCs, representing 99.7% of the information. The cell signal would occupy the first few PCs because of its correlation and noise would occupy latter PCs. However, blur affected the distribution of intensity values and caused the segmentation values to fail. The area in the centre of (a) is an example of where certain regions were falsely classified as reliable because the intensities were similar to cell signal. **(a)** Minimum projection of a stack of endothelial monolayers. **(b)** The eigenimage of (a) using the first 16 PCs. **(c)** Segmented result of (b) while applying the threshold of 0.25. Dashed line indicates a manually selected outline to represent the corresponding outline in (a). **(d)** Histogram of the eigenimage. The threshold was subjectively chosen to 0.25 which produced (c).

highlight regions which might give false gradient readings. Cell signals with low intensities are influenced by the blur from neighbouring voxels. Therefore, using the first PC only might reveal more of the cell but would also give more false readings. The selection of threshold among the values in the eigenimage is also a problem. Fig. 4.10 shows segmentation where a threshold was selected manually. The process of automatically obtaining one is difficult because of the lack of features. Investigation of the histogram did not reveal any clues to separation as the histogram was fairly uniform, with no obvious peaks. Also, the histogram of the eigenimage changes depending on how well-defined the surface of the monolayer is. Variation in the level of cell labelling within a single experiment, and between different experiments, can result in large variation to histogram distributions.

Segmentation of endothelial monolayers utilised Principal Components Analysis. This technique facilitated a separation between the reliable and unreliable regions because reliable areas were more correlated. However, the evaluation did not function well for some images because the intensity values were not consistent between the experiments. Images with less blur seemed to provide better performance than images where blur was evident.

4.2.3 Linear Diffusion

Linear diffusion is an approach where the behaviour of signal is investigated over multiple scales. The scales are often referred to as the results after consecutive convolutions. The behaviour is then defined as how the signal changes between each convolution. The result after infinite numbers of convolutions is the average value of the signal/image [72]. Unreliable regions were believed to be predominantly darker than the average value and therefore exhibit a positive diffusion rate over an infinite number of convolutions. The investigation of the sign of the diffusion rate over infinite convolutions forms the basis for monolayer segmentation.

A stack of endothelial cells mostly contained a confluent area of cells, quite opposite to the cancer-cells stacks where background is dominant. We tried to identify areas where the maximum gradient was not reliable enough to estimate the depth of the surface. The questionable regions were predominantly dark with respect to the average value of the stack, due to lack of signal. Therefore, the minimum projection would highlight these properties.

The minimum projection was thus convolved consecutively with a 11×11 pixel (2 $\times$ 2 μm) Gaussian kernel with standard deviation $\sigma = 0.5$ as described in Eq. (4.5). A fairly large n ($n = 500$) was chosen to simulate the approach to infinity ($n \rightarrow \infty$) where intensities tend to approach the average intensity as Fig. 4.11.

$$I(\mathbf{x}, n) = I(\mathbf{x}, n-1) \otimes G(\mathbf{x}, \sigma) \qquad n > 0, \qquad \mathbf{x} \in (x, y) \tag{4.5}$$

This revealed how each pixel is diffused over n. We assumed that dark areas with respect to the image average were unreliable intensity information and bright pixels with respect to the image average were reliable. The diffusion rate (i.e. the difference between two consecutive iterations) would then increase with n for dark areas as the

convolved results converge towards the average [72]. The opposite applies to signal areas which would have a negative diffusion rate.

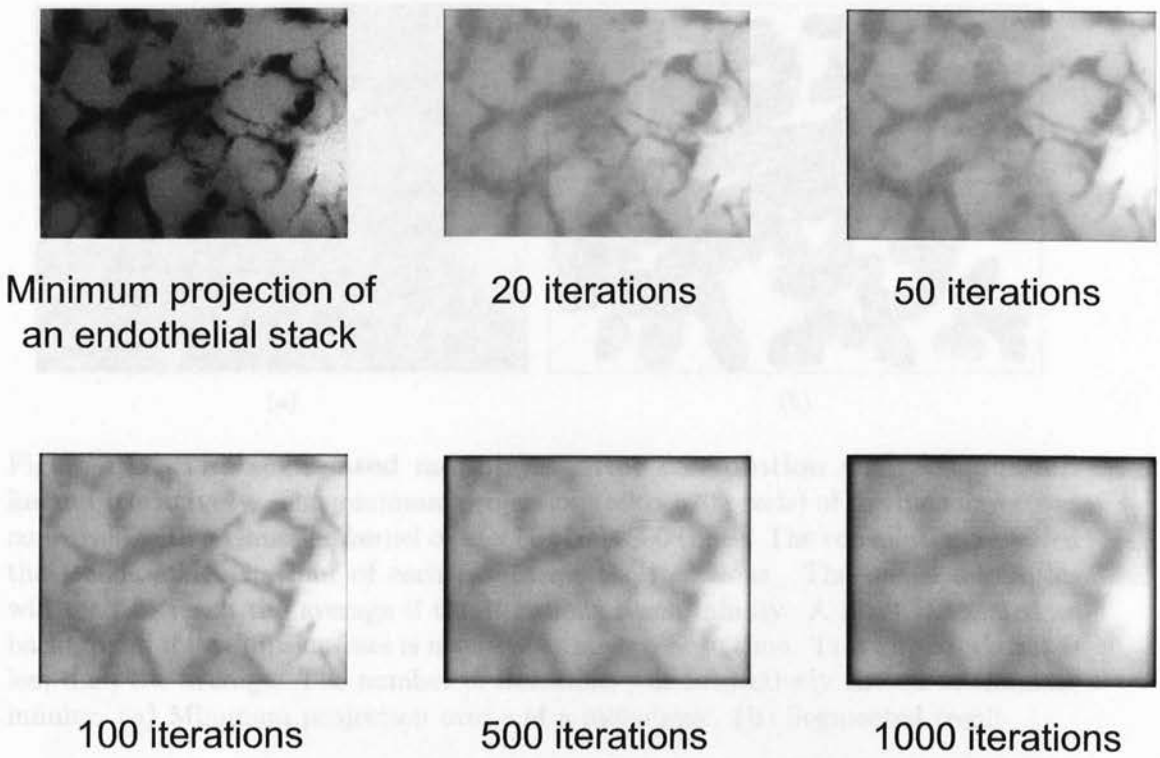

Figure 4.11: **The convolved images after different numbers of iterations.** The image (696×520 pixels) is convolved with a Gaussian kernel of σ=0.5 a number of times. The image gets more diffused with the number of iterations. The changes between 500 and 1000 iterations are small, which is why 500 is considered to diffuse the information enough to distinguish between the trustworthy and not reliable areas.

The investigation of the sign of the diffusion rate provided evidence for the separation of signal and background with noise as described above. The collection of segmented points needed to be robust against noise where sufficient excess of noise was removed. In order to facilitate robust and stable segmentation of monolayers, pixels which, at any point in the scale space, exhibited a positive diffusion rate were classified as background. This approach was needed as the local average in scale space changed between the iterations. Fig. 4.12 shows an example of a segmented

monolayer.

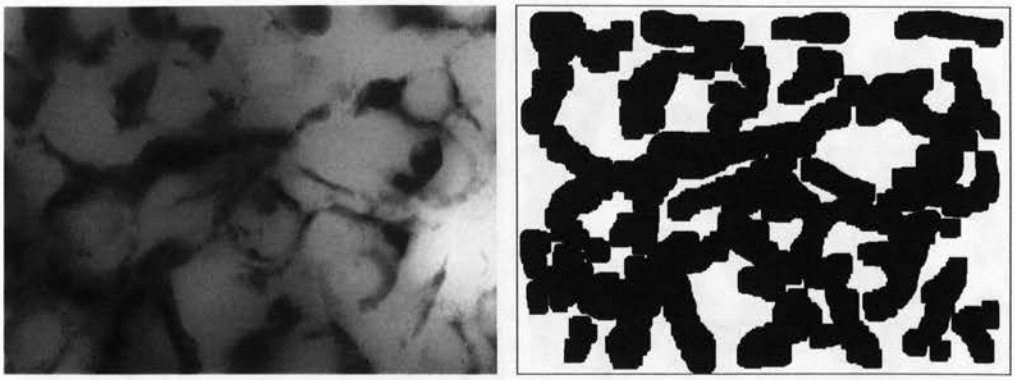

(a) (b)

Figure 4.12: **The segmented monolayer after convolution with a Gaussian kernel iteratively.** The minimum projection (696×520 pixels) of the monolayer was convolved with a Gaussian kernel of 11×11 pixels 500 times. The convolution revealed the trends and behaviour of each pixel over the iterations. The image intensities will tend to reach the average if the iterations reach infinity. A pixel is selected as background if its diffusion rate is negative at any point in time. This implies that it is less than the average. The number of iterations was subjectively chosen to simulate infinity. **(a)** Minimum projection over z of a monolayer. **(b)** Segmented result.

Applying linear diffusion to segment regions in monolayer was a stable and robust approach which provided good separation between the two classes. It targeted difficult features which histogram-based segmentation did not manage to separate. For example, a histogram-based approach needs the intensity to be fairly uniform throughout the group as each feature must belong to the same intensity range. Diffusion investigated the behaviour of the intensity over the number of convolutions such that the intensity value itself was not of immediate importance. The approach over-segmented the monolayer purposely because that ensured that the remaining regions were reliable.

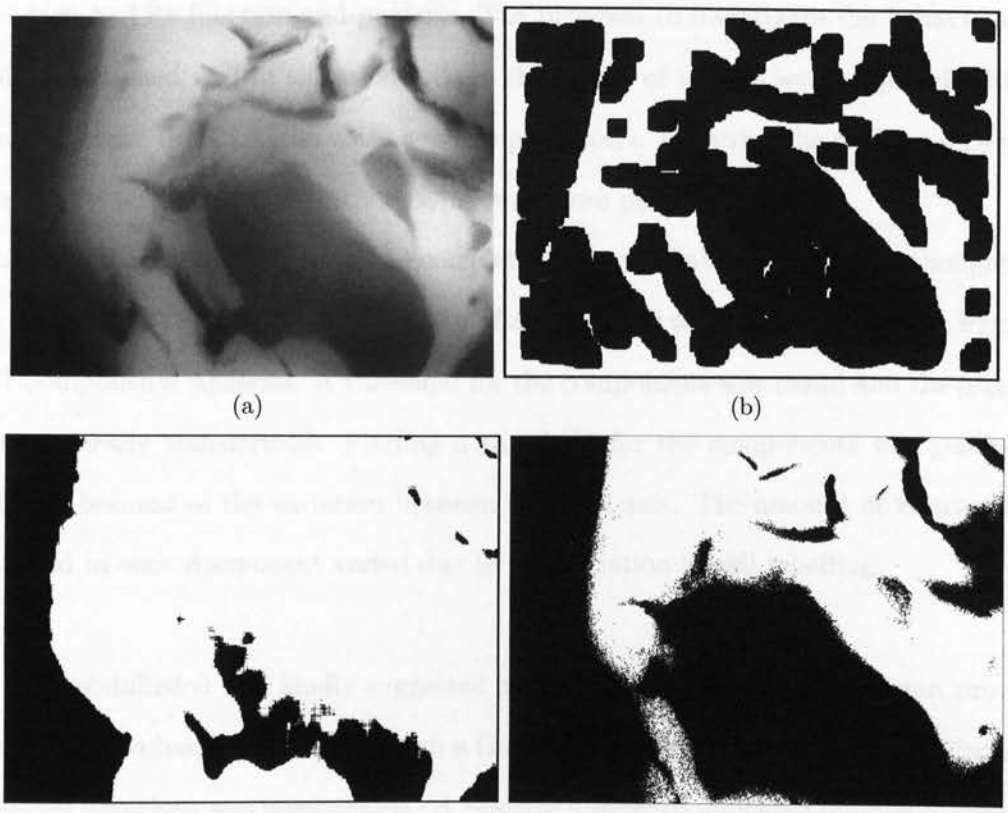

Figure 4.13: **Comparison of segmentations of a minimum projection of an endothelial monolayer stack which PCA did not manage to segment.** The minimum projection over Z was obtained from a stack of endothelial cells. The minimum projection was convolved with a Gaussian kernel 500 times and the rate at which the cell signal diffused was investigated. Linear diffusion managed to segment the large unreliable area in the centre, which PCA did not. The successful segmentation was due to the fact that the behaviour of the cell signals over the iterations was used and not intensity itself. A segmentation using Otsu [1] was included as a comparison and the segmentation performed well due to the fairly uniform labelling. **(a)** Minimum projection **(b)** Segmented result using Linear diffusion **(c)** Segmented result using PCA with 16 PCs and the normalised eigenimage which was thresholded at 0.25 **(d)** Segmented result using Otsu [1].

Separation between reliable and unreliable regions of monolayer was an important step in the analysis of cancer-cell invasion. It featured three different approaches, each of which had its function and purpose. The proposal to investigate the behaviour of noise functioned well in situations where the stacks of images were acquired with a long exposure time, i.e. the noise was less prominent. However, the performance was less impressive in situations where noise was more present.
The second approach was based on correlation where reliable regions were thought to be correlated. The minimum projection of a monolayer was transformed using Principal Components Analysis. A threshold for the components was found and the images were inversely transformed. Finding a threshold for the components was generally difficult because of the variation between the data sets. The amount of information retained in each component varied due to the variation in cell labelling.

Linear diffusion was finally suggested as a third proposition. A minimum projection was convolved consecutively with a Gaussian kernel and the sign of the difference between iterations was investigated. A positive difference indicated unreliable regions and a negative was assumed to be reliable. This path facilitated segmentation of images, which previously suggested proposals did not manage to complete. The advantage with Linear diffusion was that the threshold was based on the local properties of the image rather than a global threshold decided by external factors such as noise distribution. A comparison between two of the techniques can be found in Fig. 4.13. It was then evident that Linear diffusion was superior due to its dependence on the individual images whilst selecting a threshold.

4.3 Surface interpolation

Many interpolation techniques exist for medical imaging, such as nearest neighbour, polynomial or splines [87]. Some advocate that high-order splines are the most suitable image interpolation technique in this field because of their low error rate in both quantitative and qualitative studies [88]. Splines are a good example of where the local information is retained at the same time as the local cues add information to its global shape. Because a polynomial is fitted between each node, its result is more accurate than a regular polynomial interpolation where the best overall fitting is obtained between the interpolated and the true values. Regular interpolation suffers from some misfitting due to the fact that the aim is to find the best global match, which results in increased error. Splines share common problems with other interpolation approaches in the sense that they aim for the interpolant to go through the nodes exactly, which increases the sensitivity to noise and artifacts. This may cause awkward shapes of the surface because the splines are determined by the neighbourhood, and nodes not in a similar level to their neighbours can result in unrealistic shapes. Other approaches estimate surfaces from irregularly spaced points where a kind of triangulation is used to approximate the surface [89] (i.e. explicit surfaces). Explicit surfaces are based on some geometric representation (e.g. triangles) which makes them easy to deform but hard to fit. Implicit surfaces, which represent the surface as weighted distance functions, have also attracted some interest [90]. These are easy to fit because they only fit a weighted distance function between the points. However, deformations of these shapes are difficult because they do not contain any geometrical information which can easily be used to recalculate the new structure. Recent advances combine explicit and implicit surface representation to reconstruct a surface which seems to provide a more accurate result than the individual repre-

sentations respectively [91].

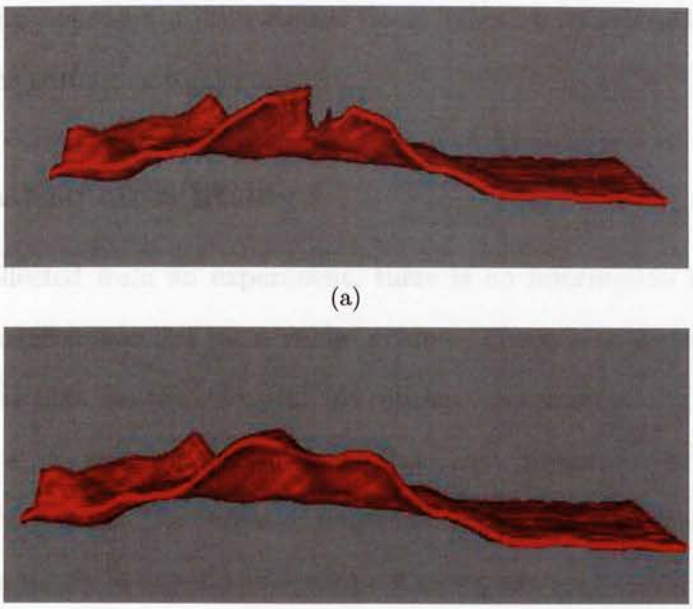

(a)

(b)

Figure 4.14: **Illustration of interpolation over a sarcoma-induced opening.** Sarcoma cells created openings within the monolayer in attempts to exit the flow channel. These openings did not contain enough signal to produce sufficient gradient values. RI measured the amount of cell signal below the monolayer in relation to the total. In order to prepare the surface for such a procedure, the opening was replaced by an interpolated overlay. **(a)** A surface with an opening caused by invading sarcoma cells. **(b)** The surface was restored by interpolating over the opening.

The Relative Invasion quantity captured the percentage of cell signal below the monolayer. Sarcoma cells interrupted the monolayer surface in their strive to exit the flow channel and these regions did not contain well-defined structures. Because of this, the surface values in these regions could not be trusted. In order to handle this situation, the regions needed to be identified and reconstructed by creating an artificial overlay which could be used in the absence of reliable readings. This approach enabled the quantification of the invasion by measuring the cell signal below the reconstructed monolayer surface in comparison to the entire signal.

The first section (4.3.1) describes an approach to fit a function to the data. The

second section explains the use of digital image inpainting to restore the unreliable regions. A third approach utilises Radial Basis Function Interpolation to create an estimate for the surface restoration.

4.3.1 Least-squares fitting

If data are collected from an experiment, there is no information about what behaviour (i.e. mathematically) these values exhibit. There is no description in terms of a polynomial that fits these values. To estimate parameters of a function which match the data, we would fit a line to the data that minimises the errors between the line and the points. The choice of polynomials depends on the spreading of the data. Most commonly in one-dimensional problems a line (regression line) is fitted to the data. The problem is most easily approached by setting up a linear system and solving for k and m as described in equation 4.6 where k is the slope of the line and m is the translation parameter.

$$y(x) = kx + m \tag{4.6a}$$

$$\begin{bmatrix} y_0 \\ y_1 \\ \vdots \\ y_n \end{bmatrix} = \begin{bmatrix} x_0 & 1 \\ x_1 & 1 \\ \vdots & \vdots \\ x_n & 1 \end{bmatrix} \begin{bmatrix} k_0 & k_1 & \dots & k_n \\ m_0 & m_1 & \dots & m_n \end{bmatrix} \tag{4.6b}$$

Once the parameters are found, the function is evaluated at the unknown data points. This produces an approximation that minimises the error between the fitted line and the data points.

This can be extended to a multidimensional case by using the equation for a plane

in a linear 2D case or e.g. a parabola in a non-linear case. The linear system is set up in the same fashion as for a one-dimensional case.

In terms of surface interpolation, only the two-dimensional case is considered as the surface is represented as a 2D depth map. The main purpose was to place a lid over the created opening and then measure the amount of cell above and below the surface according to Eq. 3.2a. The first attempt considered a plane that was fitted to the edges of the opening. The edges acted as nodes and contributed to the fitting. This technique performed well if all edges around the opening were of roughly the same height. The surface would fit nicely on top of the opening. However, problems occurred if one side was lower than the opposite because there would be an area where the plane was much higher than the actual surface. A plane is not locally flexible and cannot deform according to its surrounding nodes. Because the openings do not always have a rigid shape, the result may be a space between the fitted plane and the actual surface which may affect the quantified migration. Measuring RI in this fashion is not ideal as the parts of the cell would falsely appear to have migrated. Other interpolants have related problems.

4.3.2 Image inpainting

Image inpainting is a technique aimed at restoring damaged images which may contain e.g. cracks or loose paint due to age-related or mistreatment issues. Bertalmio *et al* pioneered *digital* image inpainting by developing algorithms to automate this task [92]. The tasks can range from repairing scratches to erasing entire objects and the objective is to adjust the destructed sections so that the previous state is invisible. The authors conclude four universal keys obtained from manual inpainting techniques [93] [94] [95]:

- The global picture determines how to fill in the gap
- The structure of the area surrounding the gap is continued into it
- The different regions inside the gap are filled with colours which match those of the boundary
- The small details are painted, e.g. bright spots on a dark background

This implies that the restoration process must take the entire picture into account, but also the information around the border. The purpose of the work is to restore the gap so it becomes invisible in conjunction with the rest of the art. Therefore it is reasonable to suggest that information on the borders provides the basis for values used for propagation into the gap. The algorithm the authors suggest propagates information into the gap in the direction of the isophotes (contour line) because lines arriving at the boundary should continue into the gap. The direction of the incoming line is found by rotating the gradient 90° which reveals the direction in which an edge is travelling. The value of the Laplacian is an image smoothness measure and is inpainted as the new value for each coordinate. The Laplacian is chosen to produce a smooth estimate. A new set of coordinates which describes

the gap is computed and the process is re-iterated until the difference between two iterations is zero. A summation of their techniques can be found in [96]. This approach provides reasonable results which are also pleasing to the eye. However, visual investigation of the results showed that only the structures were successfully restored and the algorithm has problems with correcting the texture of large regions.

The approach suggested by Bertalmio *et al* was extended to provide improvements regarding large regions. Previously, filling in large regions could introduce blurring due to the diffusion process [97] and the texture was missing. Criminisi *et al* [97] targeted this issue by combining the approaches from image inpainting and texture synthesis and used a block-based approach. The method is semi-automatic and requires input of the window size (which is suggested to be a little bit larger than the smallest texture element) and the region in which the inpainting will take place. The area to be filled is outlined manually and should preferably be selected to be tight around the object to maximise the input from the source region. It then searches for patches (blocks) that best match the border according to a patch priority derived from the product of intensity similarities and the direction of the isophote (gradient). The information from the best patch is copied into the block which is to be filled. The patch priorities consist of a confidence term and a data term. The confidence term measures how certain the values within the patch are and the data term ensures that the linear structures (e.g. edges) are propagated first. The confidence term consists of the pixels in a patch that have already been filled divided by the patch area. The pixels which belong to the source region are set to 1 and 0 for the fill region. The data term is the dot product of the normal to the contour and the gradient of the pixel rotated 90°. For each pixel that lies on the border, the confidence term is calculated and the patch with highest confidence is selected so that the sum of the squared intensity values is minimised. This is repeated until all pixels

are filled. The confidence values are recalculated after each iteration. The original values from the source region are inserted into the new position inside the hole which avoids dilution of the values. This approach handles the problem of blurring since there is no smoothing involved. However, it gives preference to line structures as the search looks for values similar to those at the edge.

Bertalmio *et al* also extended their work to incorporate a combination of structure and texture [98] where structure and texture were separated, reconstructed individually and then assembled into a reconstructed image. The algorithm comprised three steps: image decomposition, structure inpainting and texture synthesis. The image was decomposed into structure and texture by applying a framework derived in [99]. Using this approach the structure elements could be separated and reconstructed as described earlier [92]. The texture synthesis procedure defined a small $n \times n$ template with known pixel values outside the empty region Ω but in its neighbourhood. The image is then scanned for another window in the image with the smallest sum of the squared difference. The pixel value located in the missing area is replaced by the corresponding pixel value in the selected window. The two reconstructed images are added to form the final restored image.

Restoration and object removal in video sequences have also been of interest because a video sequence can be seen as a series of still images which can be inpainted. However, the temporal information as well as the spatial information needs to be incorporated because of the correlation between sequential images. An extension to still-image inpainting explores these opportunities [100]. This includes the removal of moving objects where background and foreground were handled separately. The background is extracted by investigating the optical flow and all stationary pixels throughout the sequence are classified as background. The stationary pixels are filled in through the temporal information and are taken into account using a priority

term, derived from [97]. A copy and paste operation is performed for the patch with highest priority nearest to the unknown pixel. This is performed throughout the entire sequence and each frame has a hole with equal size and position. A similar approach is suggested for moving objects so that the information from moving pixels within the patch with highest priority is copied into the new location. The stationary pixels within the patch at the new location are set to zero. This is repeated until all the pixels within the unknown region are of zero priority.

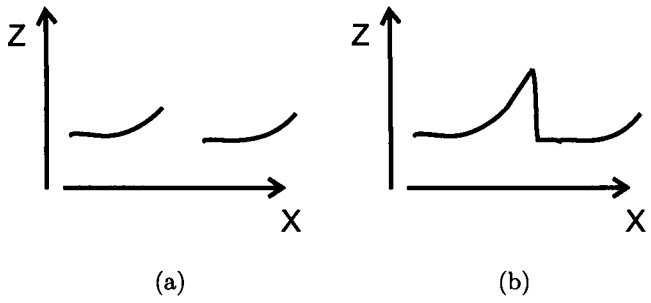

Figure 4.15: **Illustration of the disadvantage of Inpainting in the context of surface interpolation.** The main concept of inpainting is to propagate the gap with values from the boundary. The inpainting techniques gave rise to unrealistic surface reconstructions due to the fact that they inpaint in the direction of the gradient. The merging between the two sides may create very sharp transitions, which is not a good representation of the endothelial monolayer. **(a)** Illustration of a gap induced by a TC. **(b)** The inpainting algorithm tries to inpaint in the direction of the gradient which may cause sharp transition when the two edges of the surface merge.

All these approaches share the same principles and therefore also the same problems. In terms of depth maps and surface reconstruction the values are similar and seem fairly easy to recover. The depth map had no texture to account for because of the nature of the maps but structure is also the important component. The depth map itself does not contain any texture. However, restoring the values accurately is of importance. Photographs contain a wide range of intensity values and express a dynamic behaviour. The tone and the colour can vary within the image and create, for example sharp edges. They also have details which need to be accurately

restored. A depth map is simpler in its construction because it lacks these characteristics. A depth map is an image without any of the difficulties a photograph exhibits. Therefore inpainting seems to be a suitable technique for restoring missing values. Nevertheless, inpainting can produce incorrect results due to the fundamental principle of the technique. The values in a depth map represent, obviously, depth. The depth in this application is the location of the surface of the endothelial monolayer within a z-stack. The principle of inpainting is that it replaces values in the direction of the isophotes (contour lines). This is a valid assumption for photographs as the intensity values have to merge gently over the gap in order to produce a smooth output. Among endothelial cells, the occurrence of unlevelled junctions, especially in sarcoma-induced opening of the monolayer, are common and one side may have a positive slope and the other side a negative slope as illustrated in Fig 4.15(a). Because inpainting follows the direction of the isophote, the negative slope tries to reach the coverslip and the positive aims for the top of the stack. The merging of these two sides causes an unrealistic reconstruction of the monolayer which can be seen in Fig. 4.15(b). Inpainting works very well for photographs and has a valid scientific approach but is not suitable for reconstruction of a depth map of endothelial cells.

4.3.3 Radial basis function for surface interpolation

Reconstructing data from incomplete meshes of scattered data points is a common task and many problems are redefined to fit into this framework. For example, estimating 3D objects from range data is seen as an interpolation of irregularly spaced data points [101] [102] because the shapes of these objects are most commonly irregular and are not suitable for e.g. polynomial interpolation. The spacing within the object may also be irregular due to the non-linear acquisition of the data points. Polynomial interpolation, though, often requires that the data points lie on some kind of grid which limits the underlying type of data the interpolation can handle.

However, RBF interpolation is usually considered for data points < 2000 [103] because of the computation time and memory space required for larger sizes. Some argue that compactly supported RBFs are the preferred choice because of their finite size and limited area [104]. An RBF with compact support uses a finite mapping function which generates a sparse matrix with only partially filled cells. In contrast, a global RBF - which the RBF implementation in Matlab uses [105] - creates a dense matrix with values in every cell. A compactly supported RBF requires knowledge of the radius of the support where the mapping function is defined, which limits the values included in the interpolation and the values outside the radius are zero. In terms of monolayer interpolation, the assumption is that the opening in the monolayer is of finite radius, which cannot be guaranteed because the shape varies with the individual cells. In such situations, an RBF with global support is the preferred choice even though it limits the interpolation nodes and increases computation time because it does not impose any limits on the size of the region. A short formal description derived from [106] [103] [107] of the technique is given here. Readers are referred elsewhere for more details [108] [109].

Let $f : \mathbb{R}^d \rightarrow \mathbb{R}$ be a function containing real values in d dimensions and $s : \mathbb{R}^d \rightarrow \mathbb{R}$ be the function approximation of f. $f(\boldsymbol{x_i}) : i = \{1, 2, \ldots n\}$ are the known values at a distinct set of points, $\{\boldsymbol{x}_i : i = 1, 2 \ldots, n\}$ in $\mathbb{R}^d$. f is called nodes of interpolation and represents the function values at the obtained data points. A traditional Radial Basis Function is given by

$$s(\boldsymbol{x}) = p_m(\boldsymbol{x}) + \sum_{i=1}^{n} \lambda_i \phi(\| \boldsymbol{x} - \boldsymbol{x}_i \|), \qquad \boldsymbol{x} \in \mathbb{R}^d, \quad \lambda_i \in \mathbb{R} \tag{4.7}$$

where p_m is a low degree polynomial, $\| \boldsymbol{x} - \boldsymbol{x}_i \|$ the Euclidian norm and ϕ a mapping function from $\mathbb{R}^d \rightarrow \mathbb{R}$. s is now our radial basis function consisting of values from the radially symmetric function $\phi(\| \ldots \|)$ plus a polynomial. Typical choices for ϕ are Linear $\phi(r) = r$, thin-plate spline $\phi(r) = r^2 logr$, Gaussian $\phi(r) = e^{-ar}$ and multiquadratic $\phi(r) = \sqrt{(r^2 + c^2)}$. a and c are constants. We also say that $s(\boldsymbol{x}_j) = f(\boldsymbol{x}_j), \quad \forall \quad 1 \leq j \leq n$ with side conditions

$$\sum_{j=1}^{n} \lambda_j(\boldsymbol{x}_j) = 0 \tag{4.8}$$

for all polynomials q at no more than d dimensions, i.e. the basis function runs through the nodes exactly. The side condition is an optional requirement and only applies to linear and thin-plane spline and to assure a unique solution to the equation.

It is then possible to set up a linear system defined by

$$\begin{bmatrix} A & P \\ P^T & 0 \end{bmatrix} \begin{bmatrix} \lambda \\ c \end{bmatrix} = \begin{bmatrix} f \\ 0 \end{bmatrix} \tag{4.9}$$

where $A_{i,j} = \phi(\boldsymbol{x}_i - \boldsymbol{x}_j)$, $\boldsymbol{P} = \begin{bmatrix} 1 & x_1 & y_1 \\ \vdots & \vdots & \vdots \\ 1 & x_n & y_n \end{bmatrix}$, $\boldsymbol{\lambda} = (\lambda_1, \ldots, \lambda_n)^T$, $\boldsymbol{c} = (c_i, \ldots, c_i)^T, 0 \leq i \leq 2$.

The coefficients λ and c can then be used to evaluate the RBF for arbitrary points.

The definition of how the Relative Invasion was measured was defined in section 3.4. Openings along the monolayer provided false measurements related to the depth which caused the measurement to fail. Tackling this problem was achieved by interpolating over the identified regions and intentionally creating a local, artificial overlay. To achieve this we treated our depth map as scattered data points because the vertices were not equally spaced around the boundary due to irregular shapes of the unreliable regions. Radial Basis Functions (RBF) interpolation is a technique with this aim in mind [106]. An RBF interpolation in the general case is defined in Eq. 4.7 where $\phi(\| \boldsymbol{x} - \boldsymbol{x}_i \|)$ represents a univariate function and $\boldsymbol{x} - \boldsymbol{x}_i$ the Euclidean distance between two vector points. The sign of the distance is not of importance as the function ϕ is radially symmetric (hence Radial Basis Function) and gives the same value regardless of the sign. The distance is multiplied by some weights, λ which are obtained by fitting the function to some known data points. The weights which are a result of the fitting will then be used to calculate the interpolation value at the unknown data points. This approach is suitable for interpolation of noisy data as the least-squares solution decreases the influence of the noisy point. It interpolates and extrapolates over an area in an averaging sense by solving a linear system of equations which makes it robust to outliers and noise. The distance between each coordinate to every other coordinate is translated from R^d dimensions to R using the mapping function ϕ. The translated distance is multiplied with a common parameter λ for which we are trying to solve.

Because λ is calculated using a least-square solution, λ is an optimal representation of the existing surface values. Using λ to obtain the interpolated values ensures that these integrate well. Most least-square solutions such as fitting a plane to the data points create a static interpolation that can not adapt to local changes. The RBF interpolation is different in this sense as it has the ability to adapt to local data determined by the radially symmetric distance function ϕ. Data points far away from the interpolation node have a low impact (i.e. low ϕ value) and values in the local area have high influence. This creates a surface that is sensitive to its local environment as well as the global scope.

The RBF implementation in Matlab [105] was used in these experiments. The outputs from the segmentation of unreliable regions were used as a mask and multiplied with the depth map obtained with the maximum gradient (see sec 4.1.2). The depth map was smoothed with a 5×5 median filter to remove salt-and-pepper noise. The multiplication resulted in a depth map (call it S) with depth values from reliable regions and NaNs in unreliable positions. A Gaussian weighting function was selected as a mapping function as it retained local features. Points with short distances received high function values for ϕ and points with long distances received low function values. This emphasised points close to the evaluation point. The linear system was first set up and solved with the known coordinates obtained from the depth map S to retrieve some common parameters, (in this instance λ). These common parameters were then used to evaluate the RBF at the unknown coordinates. The results were depth values at the unreliable coordinates. We used every 10th value of the depth map in each dimension to reduce the complexity.

Chapter 5

Image segmentation of sarcoma cells

Image segmentation is often referred to as dividing images into groups which share similar characteristics. Characteristics could be intensity or colour and indicate that it forms an entity. One of the most common methods of segmentation is based on the histogram. If an image has bright objects on a dark background, the histogram will contain one peak for low intensity values and another peak for the high intensities with a considerably lower area in-between. The threshold is then chosen to be in the lower area and intensities below the threshold are classified as belonging to one class and the values above to another class. Estimating the threshold can either be done automatically or manually by inspecting the output while setting the threshold to a certain value. Segmenting these images is of importance to remove out-of-focus information which otherwise portrays a sarcoma-cell presence which does not reflect the true values.

Chen *et al* [110] segment the nucleus of cells from single confocal images by using Otsu's method and then watershed to separate cells close to each other. Objects are

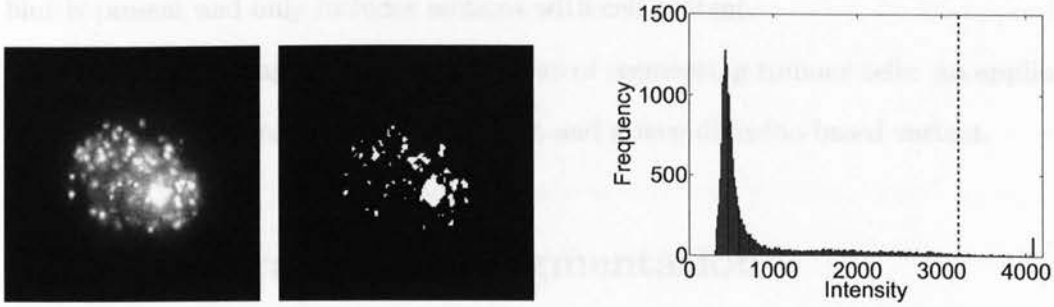

(a) (b) (c)

Figure 5.1: **Example of a manual segmentation of a sarcoma cell.** The classification was made subjectively and the thresholds were set to include the maximum amount of cell signal and minimise the out-of-focus blur. **(a)** Maximum projections of raw intensity image stacks. **(b)** The thresholded result. **(c)** Histogram of the maximum projection. The dashed line indicates the chosen threshold (3200).

then either deleted or merged depending on their size and shape. This approach does not take into account any volumetric information and, because of that, blur is not evident as in fluorescence images.

A TC cell image contains two classes: background/blur and cell signal. These have different characteristics although the intensity values of blur are very similar to those of signal. Examples of a manual segmentation of a maximum projection of a TC can be seen in Fig. 5.1. Background is predominantly darker than the others and contains noise generated from the camera, sampling noise etc. These are shown to have a Gaussian distribution (see Fig. 4.5). This assumption is altered when blur is present. Intensity values of blur are positioned in the range between signal and background and have a large variation, which is dependent on the strength of the signal. However, the highest intensity of blur will never be greater than the highest intensity of signal. Because blur does not contain any structures or any physically meaningful information, it displays predominantly a smooth structure. Cell signal values however, because of the punctate staining, display high intensities in relation to their surroundings. The segmentation of sarcoma cells excludes the areas where

blur is present and only includes sections with cell content.

The following chapter explores two areas of segmenting tumour cells: an application of a known histogram-based approach and a new diffusion-based variant.

5.1 Histogram-based segmentation

Otsu [1] developed a method for determining a threshold value in an image automatically. It is based on the histogram and tries to minimise the intraclass variance, i,e minimise the variance of the two classes. In terms of cell imaging, the two classes would represent cell signal and blur/background noise. The threshold is chosen as the intensity where the combined variance for the two classes has its minimum. This is realised by adding the variances of the two classes together for each threshold and then choosing as threshold the intensity which produces the minimum variance. It is a fast and easy-to-implement algorithm as long as the grey levels are small (i.e. ≤ 256). An example of cell segmentation can be seen in Fig. 5.2. Otsu's approach assumes though that the illumination within the two classes is uniform and does not change from object to object. This could cause issues in terms of cell segmentation where the intensity can easily vary between cells and also within the cell itself. This is caused by the fact that the fluorescence molecules (whose response to light is represented in an image as intensities) do not necessarily adhere uniformly throughout the cell. The molecules will attach to the membrane at different locations and not spread evenly. Clusters of molecules will also alter the histogram as the integrated intensity of the group appears as a higher intensity value than it is supposed to be. Lower values which actually belong to the cell will then be treated as background and cause a misclassification. This may be acceptable if those areas are few and do not form an integral part of the cell.

A histogram of a fluorescence image of a cell was neither uniformly nor normally distributed as Fig. 5.1 explains. This was due to the fact that the cell signal occupied a minor fraction of the image area. Also, the labelling of the cell in this instance was focused on the mitochondria (because mitochondria generally provide stable labelling) which only revealed a fraction of the cell itself. These features created an image with predominantly dark values and caused the histogram to be skewed. Applying Otsu's method to a skewed histogram with a long tail forces the threshold to approach the central intensity of the histogram. The minimisation of the intra-variance increases the threshold in an attempt to compensate for the large tail. For segmenting the entire cell this approach may very well be applicable (see Fig. 5.2(c)). However, such a procedure is not valid because it does not exclude the blur within the cell. Segmenting the entire cell body would then give the blur more emphasis than it deserves and cause false readings.

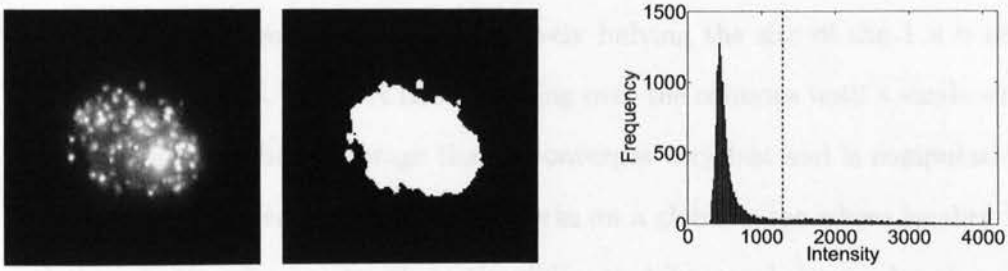

(a) (b) (c)

Figure 5.2: **Example of a segmentation of a sarcoma cell using Otsu's method. (a)** Maximum projection of a raw intensity image stack. **(b)** The thresholded result. **(c)** Histogram of the maximum projection. The dashed line indicates the calculated threshold (1285).

5.2 Diffusion-based segmentation

Linear diffusion is a process which describes how values diffuse with time and this idea has been applied to images. For microscopy, it can be used to separate out-of-focus light from true signal. Linear diffusion is seen as a convolution process where an image is convolved with a Gaussian kernel [73]. At an infinite number of iterations, the resulting image will converge towards the average value and any object present will disappear at some point. Background and noise, which are more in range with the average values of the image, will converge faster than cell signal which expresses a higher intensity. This facilitates a method of analysing diffusion rates of signal and background.

Baradez *et al* [111] describe a multi-scale method for finding a threshold in strong unimodal histograms. The image convolution is performed by arranging the image into a one-dimensional vector and iteratively halving the size of the $1 \times n$ matrix, reorganise it to a $2 \times \frac{n}{2}$ matrix and averaging over the columns until a single element remains. This has the advantage that it converges very fast and is computationally efficient. The negative aspect is that it works on a global scope where locality is lost and there is no reference to where the different diffusions belong. Another aspect is that the method is particularly designed for unimodal histograms. It assumes that a majority of the relevant information is located around the major peak. In a scenario where the mitochondria is labelled, the information in the upper segment of the histogram with very low frequencies contains the important information. The multi-scale approach assumes - because of the unimodality - that all values in the histogram greater than the first intensity with zero frequency are also zero which cannot be guaranteed with a wide-field image.

The following section describes a new cell segmentation method based on Linear diffusion.

5.2.1 Linear diffusion applied to tumour cells

The maximum projection of each TC stack was convolved with a Gaussian kernel of 11×11 pixels (2×2 μm) with $\sigma = 0.5$ for 20 iterations and a common threshold was obtained. The threshold was then applied to convolved versions of maximum projections, containing pixels above and below the surface, separately. Signal areas possess negative diffusion rates when converging towards the average of the image and therefore only pixels with negative diffusion rates were considered (although inverted to positive for calculation and representation purposes). The number of iterations was subjectively chosen to 20 which proved to provide enough information to distinguish between blur and signal. This segmented the blur and background from the signal as described in section 5.2. The threshold for diffusion rates was calculated automatically by investigating the diffusion rate after n iterations (see section 5.2.2 for details). Briefly, the diffusion rates were represented as an image and the intensity corresponded to the diffusion rates. The relative diffusion rate was plotted against the relative number of diffusion rates and the crossing of the two indicated the threshold.

This retained the highest intensities and discarded the low intensities which aided an accurate segmentation.

The objects inside the convolved images alter its shape dynamically over the iterations [112] and subsequently the diffusion rates. This means that every object changes but there would eventually exist a level of degradation where the objects are smooth and the diffusion is low. Background areas reach this level quicker than cell signal because of the similarities in intensities the background possesses.

Our approach, however, maintained the locality of each diffusion and the rate

of change indicated the content of each pixel, which aided the segmentation. The penalty was the number of iterations, where our approach had longer convergence compared to Baradez [111] but was still the preferable option as location was crucial.

5.2.2 Thresholding diffusion rates

The diffusion rates were obtained using the method described in section 5.2.1 and were represented as an image. The out-of-focus rates were different from rates of signal areas in such a way that out-of-focus had low rates. The segmentation algorithm was applied to separate the two groups. The method to segment these areas was inspired by the SURE procedure [113] and found a balance between the integrated number of pixels below a diffusion rate and the sum of the diffusion rates above. The method is explained more formally in Eq. 5.1

$$threshold(t; x) = argmin \left(\underbrace{\#\{x_i : i \leq t\}}_{a} > \underbrace{\{\sum I_i : i > t\}}_{b} \right) \tag{5.1}$$

where (a) represents the normalised number of diffusion rates below the threshold t and (b) is the normalised sum of the diffusion rates above t. This is repeated for every t. # represents cardinality, i.e. number of elements in a set. Both quantities are normalised respectively. From an implementation point of view, Eq. 5.1 could be seen as two curves (see Fig. 5.3(c)), normalised respectively, which are plotted against each other and the threshold is equal to the index where both curves cross. This procedure found a trade-off between the number of diffusion rates and the strength of them, which highlighted the punctate staining of the mitochondria. The equation might be subject to a data-scaling factor. For instance, the size of the image decreases but the size of the cells stays the same. One of the prerequisites is that the background is dominant. The threshold would change slightly if the number of background pixels

decreased and the segmentation would fail if the maximum projection contained cell signal only. However, this was not an issue because the TC images contained very few cells with a large background.

The normalisation is an important property. The values in the histograms needed to be normalised respectively as this will ensure that both features are in the range of 0-1. The total intensity then corresponds to zero number of pixels below a diffusion rate. Finding the crossing between the two curves emphasised high diffusion rates in combination with a high number of them. The procedure can be summarised as follows:

1. Ensure the levels in the diffused projection are integers.
2. Create cumulative histograms of the diffused projection for both the intensity level and the corresponding number of pixels.
3. Normalise the values of the two histograms respectively. This creates two vectors in the range of 0-1.
4. Choose as threshold the first index where the integrated number of pixels below t is greater than the integrated intensity above.

The prior knowledge about the maximum projection was that the cell signal was generally brighter than blur/noise and it was in minority within the image. Many diffusion rates with low values generated a low integrated sum of diffusion rates. On the other hand, cell signal consisted of high diffusion rates but very few in number. The two curves approached each other as the threshold candidate increased so the majority of the blur (i.e. high quantities and low integrated value) would then have been discarded. Locating the crossing was a solution which segmented the cell signal.

It is preferable to find a threshold for the diffusion rates rather than an intensity threshold of the maximum projection. Thresholding the histogram in terms of intensity excluded cell signal with low intensity. Obtaining the diffusion rates and then using this information to segment the pixels into two different classes captured this event independent of the intensity value. The important feature was that the cell signal was brighter than its surroundings. This made the segmentation independent of the intensity value itself. As such, even weakly labelled cells would be segmented correctly even though the intensity of the punctate staining might vary. Thresholding the diffusion rates ensured that weakly labelled areas were also segmented.

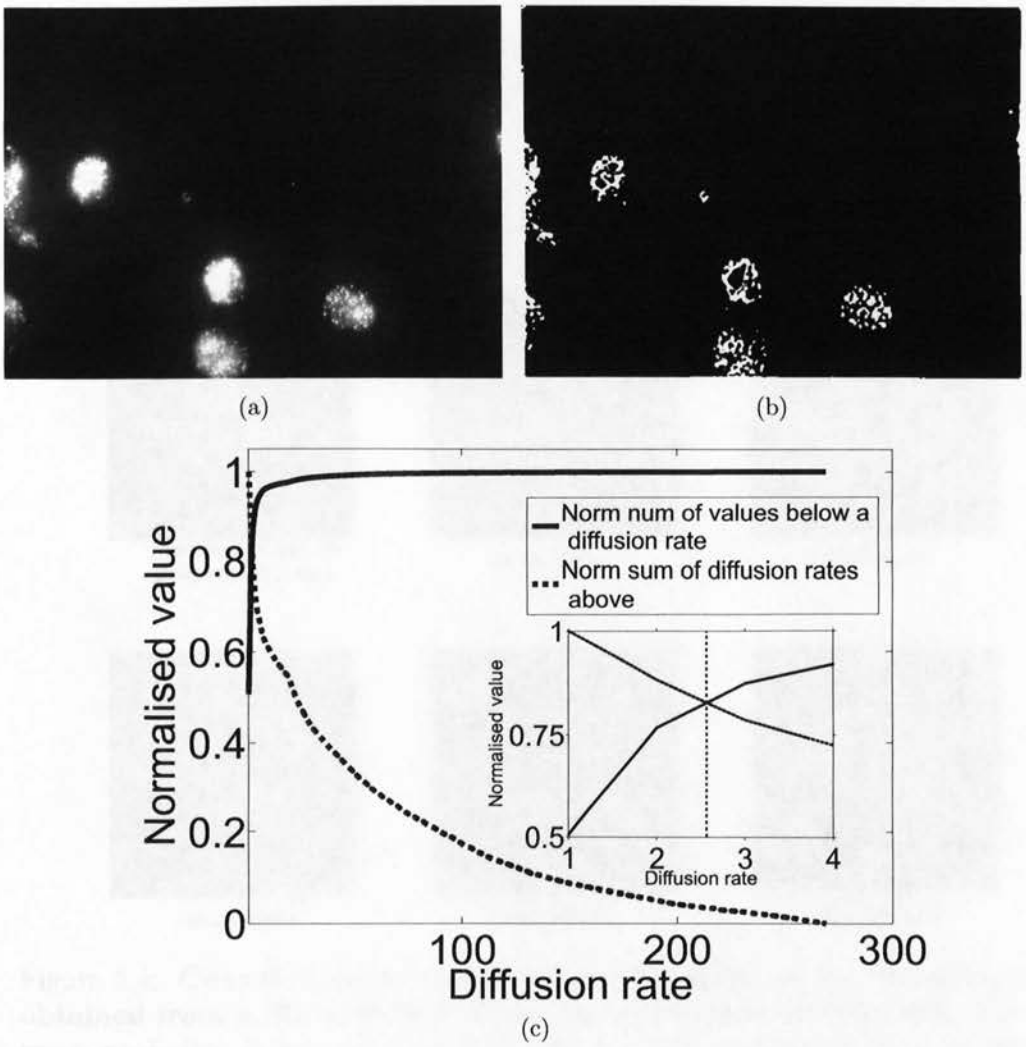

Figure 5.3: **Segmentation of a maximum projection of cells using linear diffusion.** The maximum projection image was convolved with a Gaussian kernel for t iterations (in this case t was subjectively chosen to 20). The projections over the t iterations containing the minimum value of the diffusion rate for each $< x, y >$ over the iterations were obtained. All positive rates were discarded as those represented blur and noise. For calculation purposes, though, the negative rates were inverted. To find a threshold, a normalised histogram of the diffusion rates was created and the normalised number of pixels below a threshold was plotted against the normalised sum of diffusion rates above. The threshold was selected where the number of pixels was greater than the sum of diffusion rates which in practice represented the nearest integer. The number of pixels below a diffusion rate (solid line) starts at 0.5 because 50% of the values have a maximum diffusion rate of zero (rounded to the nearest integer). **(a)** The maximum projection of the diffusion rates after 20 iterations. **(b)** The segmented result on the basis of thresholding diffusion rates. **(c)** A threshold for the diffusion rates was found by plotting the normalised number of rates below consecutive thresholds against the normalised sum of diffusion rates above the potential threshold. The threshold was chosen at the crossing of the two curves, where number of rates > the integrated sum (see inset). The vertical dashed line indicates the selected threshold which in practice is rounded to the nearest integer (in this instance a value of 3).

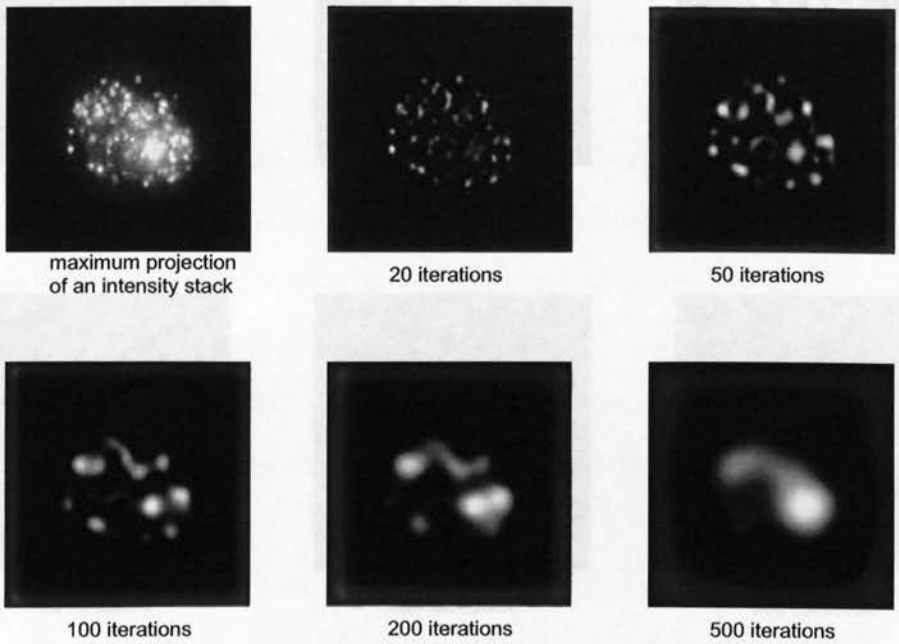

Figure 5.4: **Convolutions of a maximum projection of an intensity image obtained from a 3D wide-field stack representing a sarcoma cell.** The maximum projection image was convolved with a Gaussian kernel of 11 × 11 pixels (2 × 2 μm). Bright pixels in the maximum projection exhibited a higher diffusion rate compared to background/blur with lower diffusion rate (represented as dark values) after n iterations. However, a high number of iterations merged some features (see 100 iterations) into larger objects. This was an unwanted property and 20 iterations were found to be suitable. Values are inverted for visualisation purposes. Field size is 27 × 27 μm.

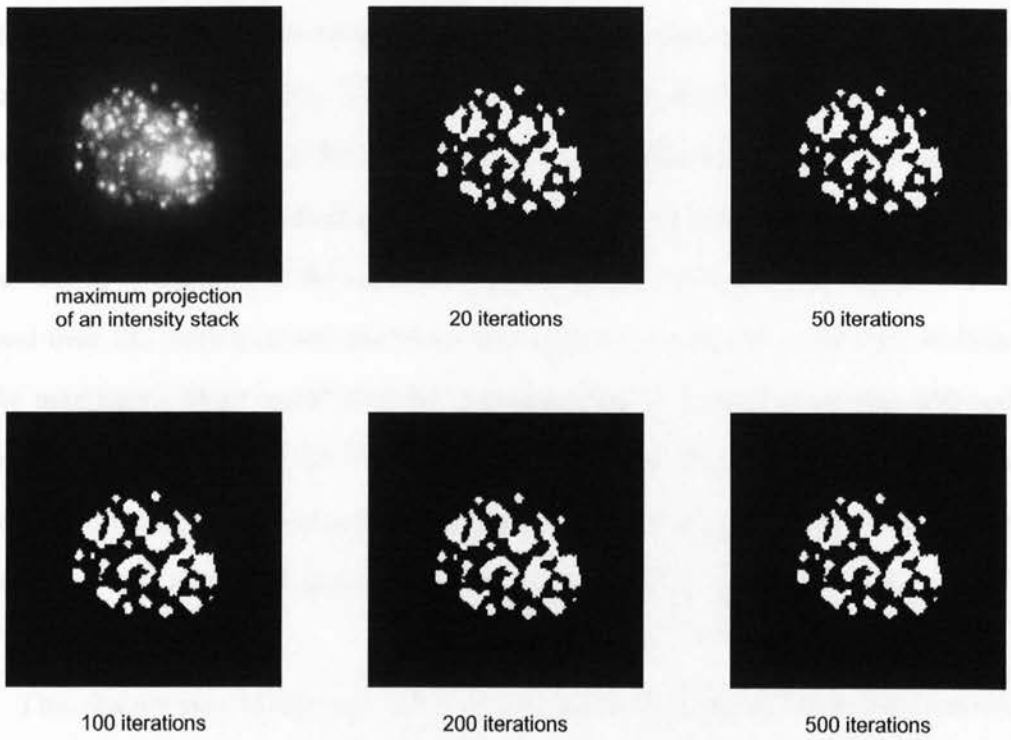

Figure 5.5: **Segmentation results of a maximum projection image containing a sarcoma cell based on linear diffusion and thresholding for a selection of iterations.** The maximum projection obtained from a 3D stack of images was convolved with a Gaussian kernel of 11 × 11 pixels (2 × 2 μm) n number of times (σ=0.5). The rate at which each pixel diffused was investigated and formed the basis for segmentation as cell signal values were different and diffused more quickly than blur and background. The maximum rate for each <x,y> was represented as intensity in an image. A threshold for this image was selected at the intensity level where the normalised number of pixels below a threshold candidate was greater than the normalised integrated intensity above (see Fig. 5.3(c)). The segmentation results look similar because the maximum values over the iterations are chosen which were the same in each case. Therefore, 20 iterations were chosen. Each result was also filtered with a 5 × 5 median filter to remove noise. Field size is 27 × 27 μm.

The number of iterations was subjectively chosen to 20. The number of iterations needed to be high enough so that cell signal stabilised to a low value where the maximum diffusion rate differentiated between the two groups. Choosing the maximum diffusion rate over 20 iterations highlighted the fact that cell signal diffused slower than unreliable regions. Fig. 5.4 evaluates the number of iterations. The figure shows the segmentation after a different number of convolutions and 20 iterations showed to be satisfactory. The fact that all iterations showed very similar segmentation results was due to the fact that the maximum projections were used. The values were diffused over the iterations and therefore approaching lower rates until they stabilised. The maximum values would then be the same after 20 iterations as after 500 and it was then concluded that 20 iterations were adequate. Fig. 5.5 shows that the segmentation results after n iterations and 20 iterations produce similar results as after 500 iterations. Iterations above 20 were therefore considered unnecessary.

This chapter described a new approach to segmenting tumour cells from a stack of images acquired with a wide-field microscope. The mitochondria appeared as small bright elements which were significantly different from their surroundings. The rate at which these elements were diffused formed the basis for the segmentation. A high rate indicated cell signal. The segmentation was made independent of the intensity value because it utilised the diffusion rate. This was necessary because cell signal could in some areas be similar to non cell signal in other areas. Investigating the diffusion rate provided a reliable segmentation.

Chapter 6

Validation of image-processing procedures

Validation of the different approaches is an important step in the process of verifying that a technique actually is accurate. Evaluation in many cases utilises some kind of truth, particularly data sets where the true data is provided. For example, to estimate the position of humans in images, wireless markers can be placed at different locations on the subject's body and the marker's local position is captured along with the image sequence [114]. The data captured from the markers form a true estimation of the position, which can be used for evaluation.

The validation procedure described in this chapter validated the recovery of the upper surface using maximum gradient, surface interpolation with $RBFs$, tumour-cell segmentation with Linear diffusion and Relative Invasion. This was achieved by using confocal stacks for reference. Artificially generated image stacks designed to represent the signal of the cell mitochondria were also created and subsequently convolved with a PSF to simulate wide-field conditions.

This chapter validates the correctness of the suggested methods and describes

how the validation data was obtained and used.

6.1 Validation data set

In our scenario, true values are not available due to the nature of the wide-field acquisition technique. The wide-field microscope uses a large pinhole which introduces blur in the stack of images and true surface z-levels are therefore difficult to obtain. To validate the techniques applied to wide-field images, a ground truth or true value based on a confocal stack and stacks with artificially created mitochondria was generated. A confocal microscope provides optical sectioning which reduces the out-of-focus information normally present in the wide-field technique [61]. Therefore, fluorescence signals obtained with a confocal microscope originated from their respective z-levels only and could form a ground truth for the evaluation.

A laser scanning confocal microscope LSM 510 (Carl Zeiss MicroImaging GmbH, Jena, Germany) with 63× 1.4 NA lens for imaging cells fixed with 4% paraformaldehyde solution was used in order to complement the dynamic studies. The fixed cells were imaged in their fixed solid state to provide a test bed for the surface reconstruction. Because the confocal microscope reduces the out-of-focus light to a minimum, the captured intensity in the confocal stack could be assumed to originate from the surface only. Therefore the axial position of the maximum gradient corresponded to the surface and the confocal stack was then used as reference or ground truth.

The acquired confocal stack was subsequently convolved with a PSF representing the set-up used in the dynamic experiments and resulted in a new stack with wide-field properties. Fig. 6.1 explains the procedure. The PSF was constructed by acquiring a 3D image stack ($0.1\times0.1\times0.2$ μm/pixel) of a small fluorescence bead of size 175nm using identical equipment as in the dynamic studies. Three stacks of acquired beads

were processed in Huygens (Scientific Volume Imaging, Netherlands) to output one 3D stack which described the Point Spread Function.

The confocal stack with fixed specimen was acquired with resolution <x,y,z> = 0.07×0.07×0.2 μm/pixel. It was adjusted to <0.1×0.1×0.2> μm/pixel to have the same resolution as the PSF. These two were convolved but scaled further to <0.33×0.33×0.2> μm/pixel prior to convolution in order to reduce computation time. The convolved result with resolution <0.33×0.33×0.2> μm/pixel now resembled a stack acquired with a wide-field microscope. The maximum gradient and corresponding depth maps were calculated for the confocal and the convolved result.

The surface reconstruction was confirmed by locating the surface manually in a set of wide-field stacks of monolayers. The result was then compared to the interpolation results.

The tumour-cell segmentation was validated by creating a test stack which simulated cells acquired with the wide-field microscope.

To simulate mitochondria as closely as possible, random numbers of bright boxes of size 4×4×12 pixels (1.6×1.6×2.4μm) were inserted artificially into empty stacks (80×80×76 pixels at resolution 0.4×0.4×0.2μm/pixel) at random (but normally distributed) positions. The size of the objects was determined by investigating a wide-field stack containing TCs and a representative size for mitochondria was concluded. The normally distributed positions ensured that the boxes had the possibility of forming clusters, similar to mitochondria. These were further convolved with a PSF with matching resolution to replicate wide-field conditions. Both stacks were normalised between 0-1 prior to convolution so that the intensity values of the convolved result would not be excessively high. Fig. 6.2 shows a diagram of the creation process. Manual inspection of wide-field stacks suggested that the intensity for mitochondria was around 100 for an 8-bit stack. Therefore, the stacks were normalised again in

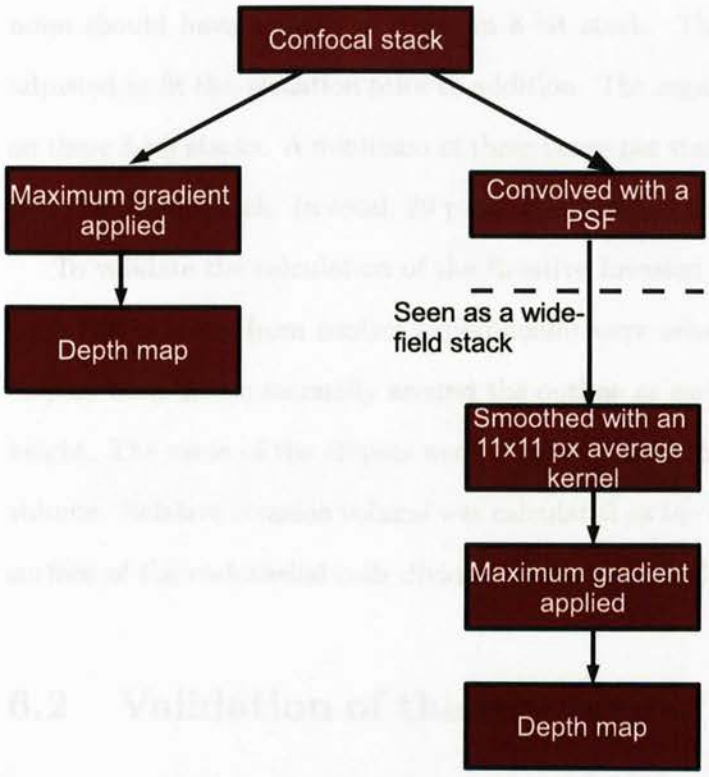

Figure 6.1: **Procedure of the creation of a validation data set for the maximum gradient.** The validation of the maximum gradient featured a data set based on a confocal stack. A confocal stack of a monolayer with fixed specimen was acquired with resolution <x,y,z> = 0.07×0.07×0.2 μm/pixel. The resolution of this stack was adjusted to match the resolution of a PSF (0.1×0.1×0.2). These were convolved and the result was a new stack which resembled wide-field conditions. The new convolved stack contained images with <0.33×0.33×0.2 > μm because the <x,y> resolution of the two stacks was decreased by 1/3 prior to convolution to reduce computation time. The maximum gradient was applied on both the adjusted and the blurred confocal stack where the confocal acted as a reference sample, i.e. ground truth. The depth maps obtained as a result were then compared.

that range after the convolution.

In order to achieve more realistic conditions, samples were obtained from a sequence of z-planes acquired with a wide-field microscope without cells to represent noise. The noise was added to the original and the convolved after the convolution. Manual inspection of wide-field stacks suggested that the intensity distribution for

noise should have a mean of 5 for an 8-bit stack. Therefore, the distribution was adjusted to fit this situation prior to addition. The segmentation was then performed on these 8-bit stacks. A minimum of three boxes per stack was generated and inserted into the empty stack. In total, 29 pairs were created and used in the evaluation.

To validate the calculation of the Relative Invasion (RI) parameter, 12 cells (six from flow and six from control experiments) were selected randomly. For each cell ellipses were drawn manually around the outline at each z-plane throughout the cell height. The areas of the ellipses were integrated over the z-stack to approximate cell volume. Relative invasion volume was calculated as the volume underneath the upper surface of the endothelial cells divided by the entire cell volume.

6.2 Validation of the recovery of the upper surface using maximum gradient

A stack of images obtained with a wide-field microscope introduce blur which alters the estimated surface z-levels. In order to assess the accuracy of the surface recovery the validity of the depth map produced by the surface reconstruction needed to be addressed.

The surface of the blurred confocal stack was estimated by locating the axial position of the gradient for each $< x, y >$ (see Fig. 6.4) as described in section 4.1.2 and compared to a surface map reconstructed from the maximum intensity values in the original confocal stack (see Fig. 6.3). The stack was convolved with a smoothing kernel with an 11×11 on a plane-by-plane basis to decrease noise. Table 6.1 evaluates the error between different sizes and shows that and 11×11 gave a higher error than 19×19 but the smaller size was selected because the difference in error was tiny. The average error for 11×11 was 3.16 z-levels ($0.63\mu m$). A rendering of the two stacks

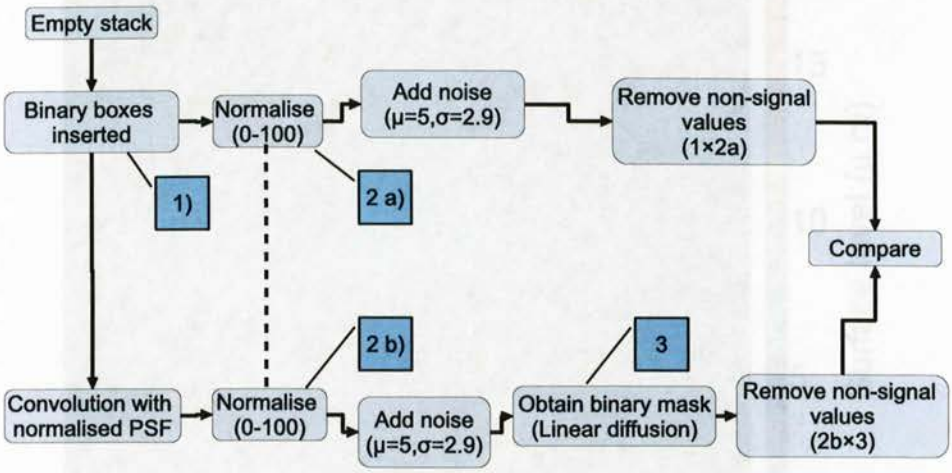

Figure 6.2: **Flow chart of the construction of the sarcoma-cell validation data set.** Boxes of size 4×4×12 pixels with intensity of 1 were inserted into an empty stack at random <x,y> positions. This stack was convolved with a normalised PSF where the convolved result simulated wide-field conditions. The number of boxes in each stack was selected randomly but the minimum number of boxes was set to three. Noise at randomly selected locations was sampled from a stack acquired with a wide-field microscope containing no cells. The noise was added to the original stack with binary boxes and to the convolved stack after the convolution procedure (2a and 2b). The stacks were normalised between 0-100 so that a comparison could be made. Manual inspection of stacks with sarcoma cells suggested the intensity for cell signal should have a value of around 100. The segmentation procedure was applied to the maximum projections of the wide-field stacks and produced a binary mask. The binary mask (marked 3) was multiplied with the maximum projection of the intensity (marked 2b). The maximum projection of the stack with binary boxes (marked with 1) was multiplied with the maximum projection of the same stack but with noise added (marked 2a). This ensured that non-signal values were excluded. Correlation was then calculated on the remaining signal values.

can be seen in Fig. 6.7. Fig. 6.5 shows the corresponding error map. The error is seen to be large at areas with high edges which is caused by influence from neighbouring edges. Fig. 6.6 also shows a profile plot over z of the centre y-position and the values

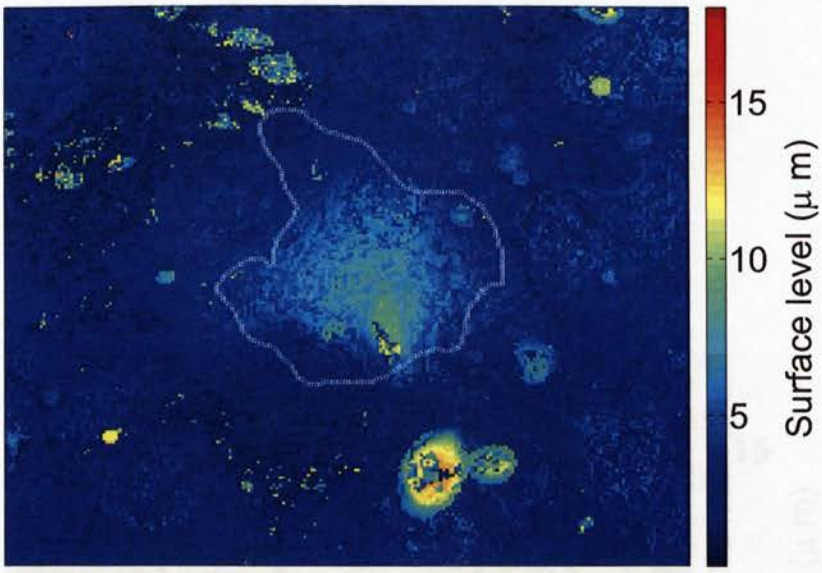

Figure 6.3: **Reconstructed surface using maximum gradient from a stack obtained with confocal microscopy containing a monolayer of endothelial cells.** The surface of the monolayer was reconstructed by finding the z-position of the maximum axial gradient for each $< x, y >$. The image stack contained image planes of 73×73 μm at 50 different z-levels (0.33×0.33×0.2 μm /pixel). The white border line indicates the border of the sarcoma cell.

seem to correlate well (Spearman r=0.86, p-value <0.0001)

Kernel size (pixels)	Error (avg z-levels)	Error (avg μm)
11×11	3.16	0.63
19×19	3.14	0.62
25×25	3.28	0.65

Table 6.1: **Average error of surface estimation using maximum gradient with different average kernels.** A confocal stack was blurred with a PSF obtained with a wide-field microscope. Each plane in the blurred stack was filtered with a 2D average kernel to smooth out noise. The depth map consisted of the z-location of the maximum gradient value for each <x,y>. The depth map from the blurred stack was compared with the depth map from the original confocal depth map and the error shows that smoothing did not have a direct impact.

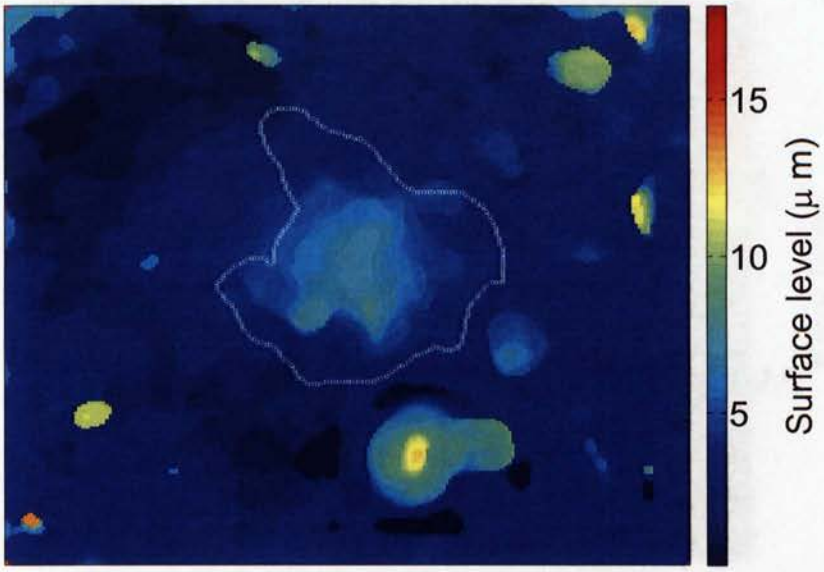

Figure 6.4: **Reconstructed surface using maximum gradient from an intentionally blurred confocal stack containing a monolayer of endothelial cells.** A stack acquired with confocal microscopy was blurred with an acquired PSF. The surface of the monolayer was reconstructed by finding the z-position of the maximum axial gradient for each $< x, y >$. The image stack of the source contained image planes of 73×73 μm at 50 different z-levels (0.33×0.33×0.2 μm /pixel). The white border line indicates the border of the sarcoma cell.

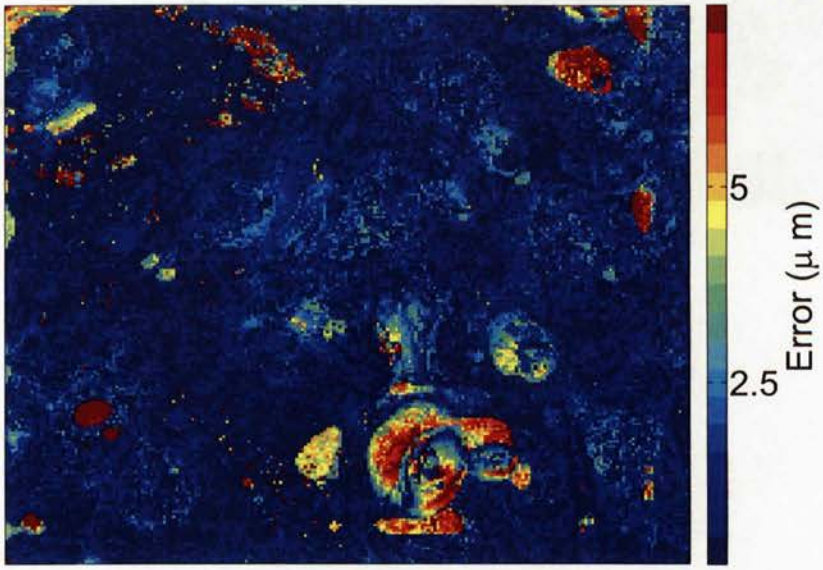

Figure 6.5: **Error map of depth values obtained with the maximum gradient technique between a confocal stack and a convolved version of itself.** A stack acquired with confocal microscopy was blurred with a measured PSF to enable wide-field properties. The maximum gradient was applied in both instances and the error is displayed as a map. Manual assessment determined the thickness of the monolayer to 8 z-levels (1.6 μm). Mean value of absolute difference: 3.16 slices (0.63 μm), standard deviation: 4.4 (0.63±0.88 μm). Manual assessment determined the thickness of the monolayer to 8 z-levels (1.6 μm).

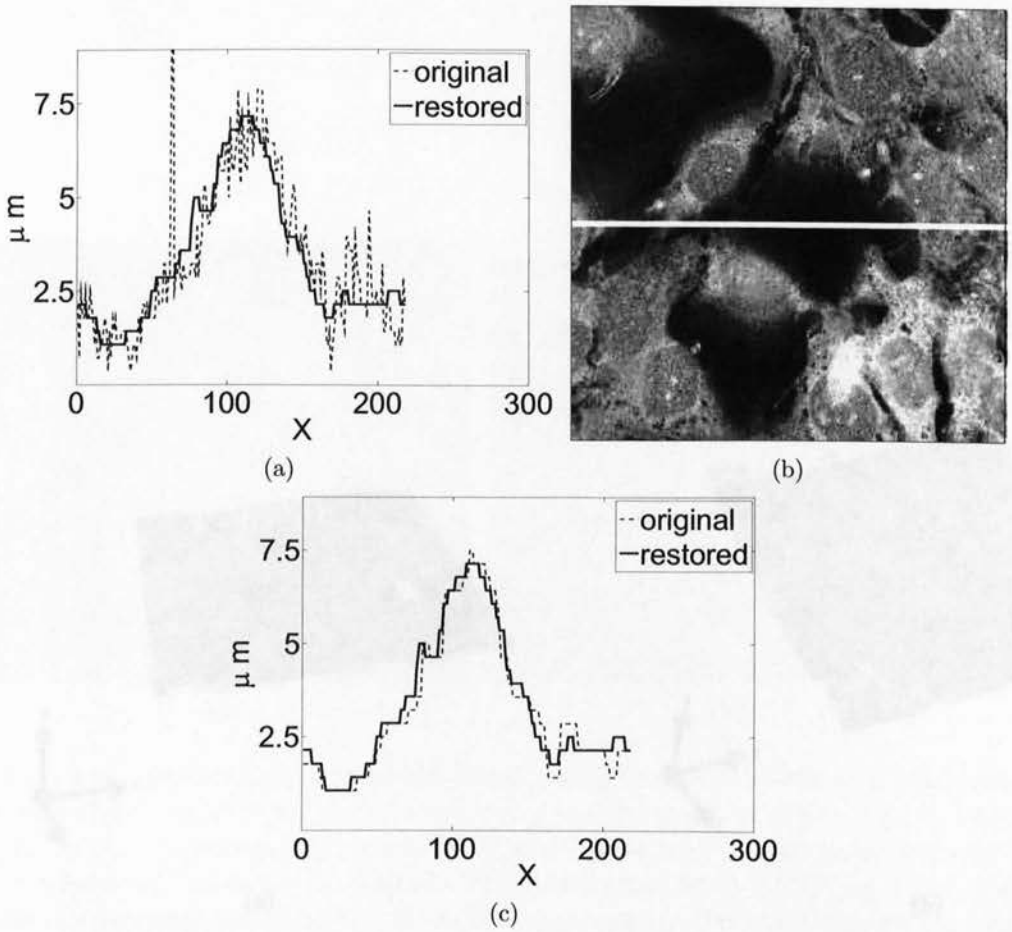

Figure 6.6: **Graph of depth values of a cross-section obtained from a stack.** A confocal stack was convolved with a PSF to simulate a wide-field acquisition and depth values were obtained using the maximum gradient over z. The units are in relation to the coverslip. **(a)** Depth values are plotted over a cross-section. Dashed line indicates values from the confocal stack and solid line represents the convolved version where the values from the confocal stack then acted as a reference. The two versions seem to correlate well (Spearman correlation, r=0.86, p-value < 0.0001). **(b)** Image of the in-focus plane of the confocal stack. The white line in the centre indicates the location of the cross-section. **(c)** shows a profile plot of the same position but both stacks have been smoothed with an 11×11 prior to obtaining the maximum gradient.

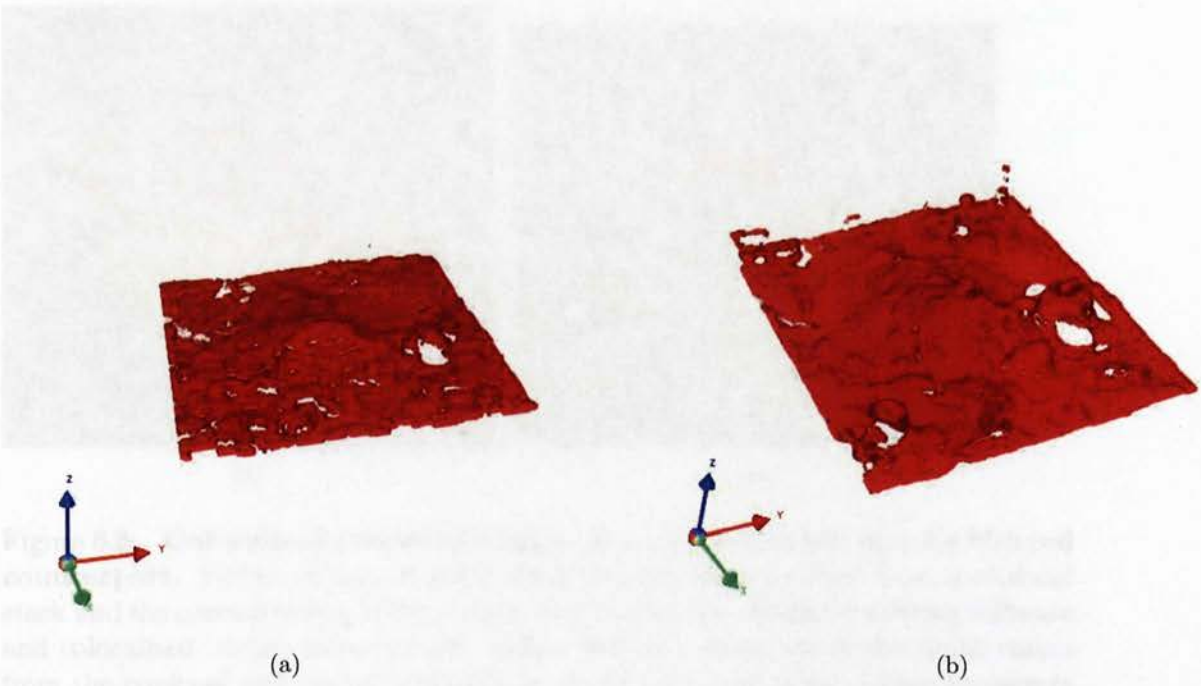

(a) (b)

Figure 6.7: **Surface rendering of confocal stacks restored using the maximum gradient.** The maximum gradient technique applied for each <x,y> over z to produce depth values. The depth values are presented as a 3D surface volume and both seem to agree well. The images were rendered using Volocity (Improvision, UK). **(a)** The original confocal surface rendering. **(b)** Surface rendering from a restoration of a blurred confocal stack.

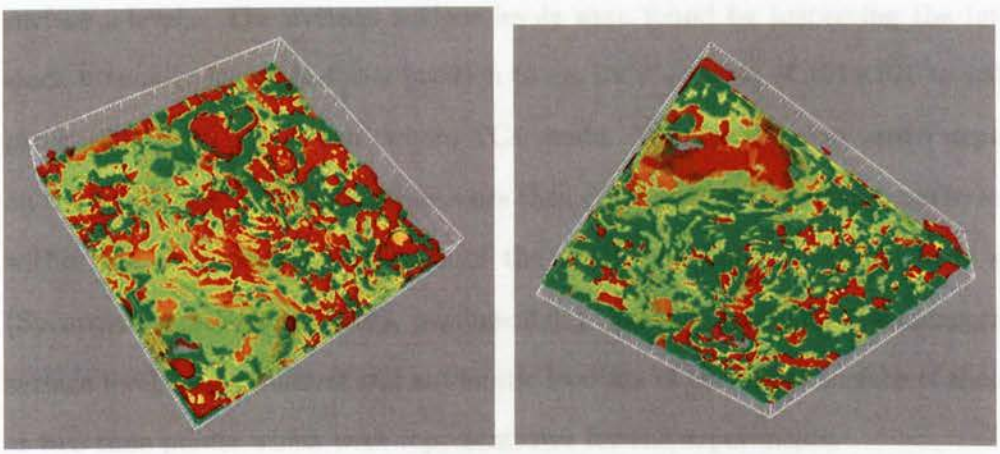

(a) (b)

Figure 6.8: **Colocalised rendered images of a confocal stack and its blurred counterpart.** Surface values obtained using the maximum gradient from a confocal stack and the corresponding blurred stack were loaded into volume-rendering software and colocalised images were created. Yellow indicates areas where the depth values from the confocal and the blurred version were exactly the same. Green represents areas where the confocal surface values were higher and red represents areas where surface values obtained from the blurred stack were higher. The surfaces represent ±3 z-levels around the estimated value. The values are not always identical because the surface values fluctuate (see Fig. 6.6). Images rendered using Imaris. **(a)** Top view. **(b)** Bottom view.

6.3 Validation of surface interpolation

The surface interpolation was made using RBFs. A manual inspection of the data set was made in order to validate the assumptions and we estimated the surface of a number of selective stacks of monolayer at two time points. The stacks were selected so that the set of the ECs comprised images with good contrast around the surface z-levels. The average surface levels were found by inspecting the intensity stack manually for its in-focus position in an <x,y> region of 101×101 to 155×155 pixels (20×20 to 31×31 μm) where TCs reside. The window size varied depending on the size of the TC. The z-values were then compared to the average surface values within the corresponding windows of the depth map and the values were similar (Spearman correlation, r=0.95, p-value<0.01). Table 6.2 presents the comparison of surface levels using manual and automatic location of the upper surface of three cells at two time points which were representative for the experiments.

		avg z-levels	
Cell no	Time (min)	Manual	automatic
s2c	30	5	5
	90	3	3
s3c	30	4	5
	90	3	3
s4c	30	5	5
	90	3	4
s6f	30	14	14
	90	15	15
s12f	30	15	16
	90	17	16
s16f	30	16	16
	90	16	15

Table 6.2: **Comparison of the surface interpolation technique with manual estimation.** The surface interpolation technique was compared to manual estimation in order to test its accuracy. The manual values was obtained by inspecting selective intensity stacks manually for their in-focus position in the region where the invading cells resided and the interpolation was based on RBFs. These two correlated well (Spearman r=0.95, p-value<0.01). The values represent average surface values and a z-plane of 1 is top of stack.

6.4 Validation of tumour-cell image segmentation

To evaluate the accuracy of the semi-automatic tumour-cell segmentation, a comparison was made between a reference stack (ground truth) and a convolved version of the same stack. Random numbers of bright boxes of size 4×4×12 pixels were inserted into binary stacks at random positions. The sizes of the objects were determined by investigating a wide-field stack containing TCs and a representative size for mitochondria was concluded. These stacks were convolved with a PSF to replicate wide-field conditions as described in section 6.1 and noise was added. This resulted in two image stacks where the original, created prior to convolution, was used as a reference sample to evaluate the segmentation performed on the convolved stack. Noise from an empty stack with no cells, acquired with a wide-field microscope, was added to both stacks after the convolution.

The segmentation procedure was performed on maximum projections of the convolved stacks using Linear diffusion as described previously (section 5.2.1). The segmentation resulted in a binary image which - when multiplied with the maximum-intensity projection - acted as a mask to mask out non-signal values. The maximum projection of the binary stack acted as a mask to remove non-signal values. Examples of maximum projections and masks can be seen in Fig. 6.9.

The Gaussian kernel used in the Linear diffusion process was adjusted to a size a little bit bigger than the simulated mitochondria and set to 7×7 pixels during the validation process. This value was different compared to the kernel size used to segment real wide-field images in chapter 5. The creation of the validation data set was time consuming and the <x,y> resolution was therefore decreased to reduce computation time. The kernel size needed to be adjusted accordingly so that all processing was performed at the same resolution.

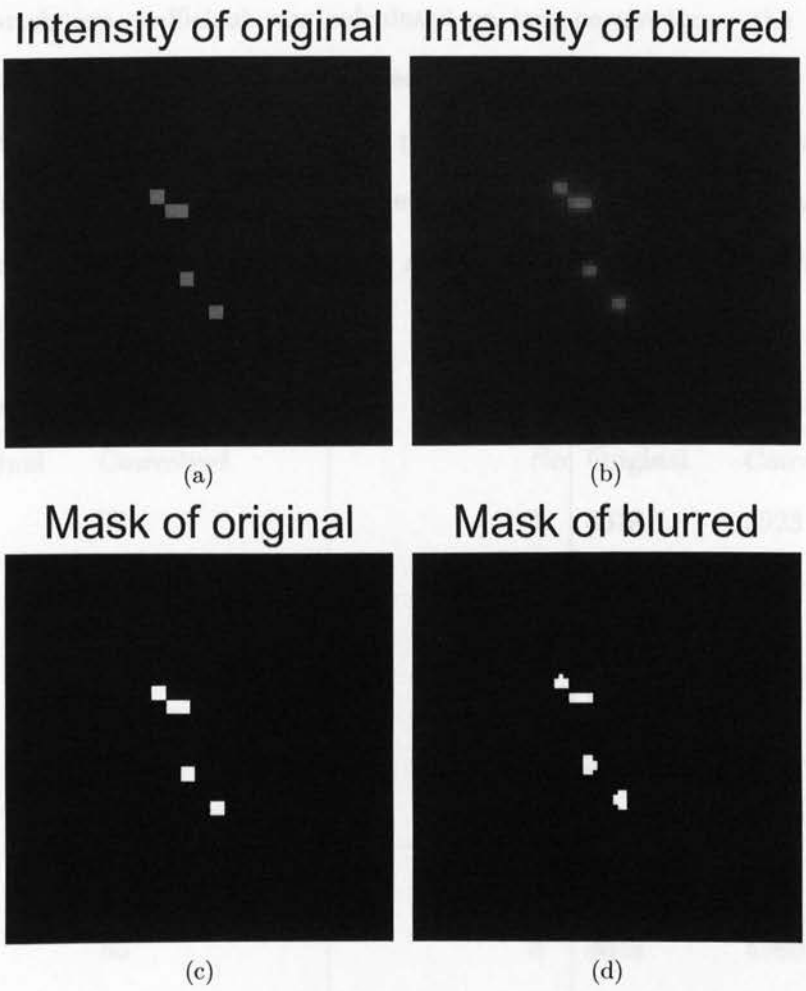

Figure 6.9: **Examples of maximum-projection images and their respective masks.** Boxes were inserted into an empty stack to mimic mitochondria and form some kind of ground truth. This stack was convolved with a PSF to resemble sarcoma cells obtained with a wide-field microscope. The segmentation was applied on maximum-projection images of the convolved version and resulted in a binary mask. The mask related to the original stack was given by the maximum projection of the stack prior to convolution. The two binary masks were multiplied with their maximum-intensity projections respectively. The correlation between the sum of the intensities before and after convolution was calculated as well as the correlation between the number of segmented pixels in the masks. Noise was added to both stacks after the convolution. **(a)** Maximum-intensity projection of the original stack with added noise. **(b)** Maximum-intensity projection of the convolved stack with added noise. **(c)** The binary mask of the original. This is also the maximum projection prior to convolution. **(d)** The binary mask produced by the segmentation of the maximum projection of the convolved stack.

The correlation coefficient was calculated on two parameters - the number of segmented pixels and the intensity of the segmented pixels - by evaluating 29 pairs of image stacks. The number of segmented pixels in the original image was compared to the number of segmented pixels in the convolved image as well as the intensity of the segmented pixels respectively. The result is shown in Table 6.3 and suggested that the segmentation was significant.

Number of segmented pixels

No	Original	Convolved
1	54	54
2	34	31
3	36	43
4	42	37
5	45	43
6	54	60
7	45	49
8	54	55
9	36	38
10	54	54
11	34	31
12	45	43
13	54	60
14	45	49
15	54	55
16	36	38
17	54	54
18	34	31

Sum of intensity

No	Original	Convolved
1	4578	5923
2	2581	3747
3	3459	3974
4	3035	4631
5	3681	4932
6	4885	5947
7	4075	4970
8	4648	5960
9	3165	3947
10	4578	5923
11	2581	3747
12	3681	4932
13	4885	5947
14	4075	4970
15	4648	5960
16	3165	3947
17	4578	5923
18	2581	3747

19	36	43
20	42	37
21	45	43
22	54	60
23	45	49
24	54	55
25	36	38
26	54	54
27	34	31
28	36	43
29	42	37

r = 0.9151,

p-value < 0.001

Table 6.3 **a)**

19	3459	3974
20	3035	4631
21	3681	4932
22	4885	5947
23	4075	4970
24	4648	5960
25	3165	3947
26	4578	5923
27	2581	3747
28	3459	3974
29	3035	4631

r = 0.9375,

p-value < 0.001

Table 6.3 **b)**

Table 6.3: **Results obtained from the validation of tumour-cell segmentation.** Boxes of size 4×4×12 were inserted at random <x,y> positions into an empty stack. This stack was convolved further with a PSF where the convolved result simulated wide-field conditions. The TC segmentation was applied on the maximum projection of the convolved which produced a binary image (i.e. a mask). The mask was multiplied with the maximum-intensity projection of the convolved stack in order to remove non-signal values. The mask of the original was obtained by using the maximum projection of the binary stack with boxes created in the first instance. This was multiplied by the stack obtained prior to convolution. This meant a stack with noise plus some cell signal values. The results after multiplication were compared. The number of segmented pixels (6.3a) in the original maximum projections correlated well against the number of segmented pixels in the convolved version (r=0.91). Similarly, the sum of the intensities of the maximum projections (6.3b) before and after convolution also showed good correlation (r=0.93). Fig.6.10(a) , Fig.6.10(b) show example images on which the sum of the intensities in each image was correlated and Fig.6.10(c) and Fig.6.10(d) show examples of segmented images where the number of segmented pixels were correlated.

The shape and position of the segmented boxes were slightly altered, evident from Fig. 6.10, which was caused by the asymmetric shape of the PSF but still correlated well. For information about PSFs and image degradation, McNally *et al* [59] is a good starting point.

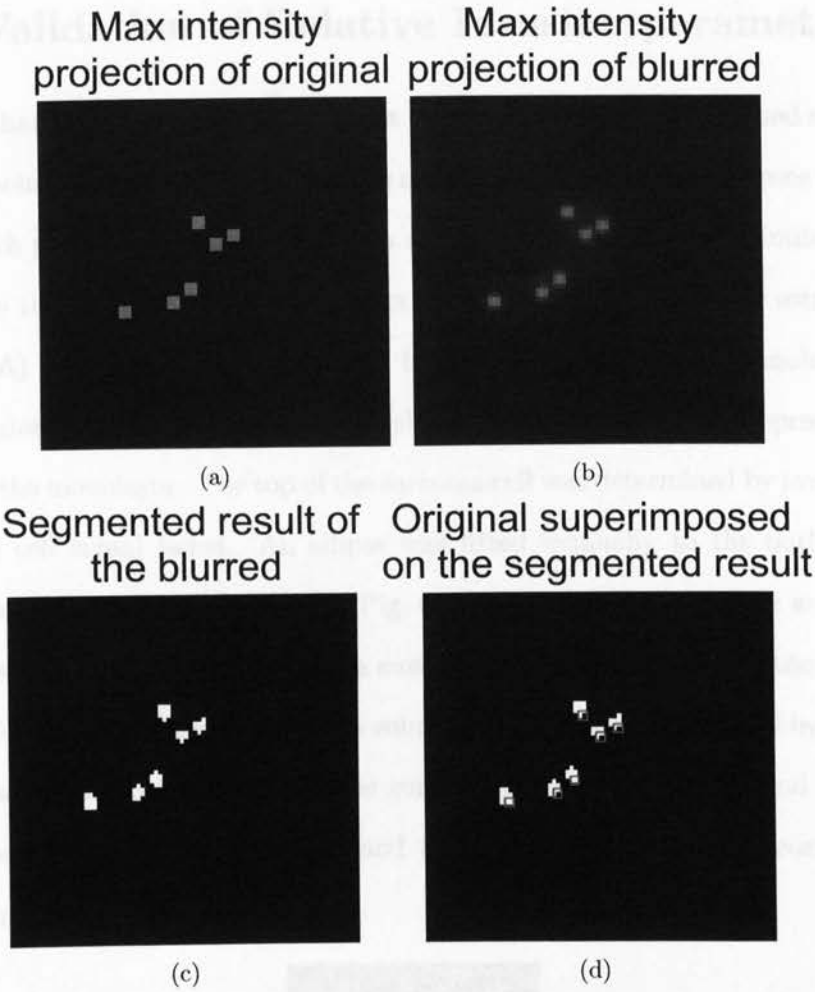

Figure 6.10: **Example of a segmentation result of the validation of tumour-cell segmentation.** Boxes of size (4×4×12) were inserted into an empty stack at random <x,y> positions. This stack was convolved with a PSF obtained from a wide-field microscope which used the same equipment as the actual experiments. The resulting stack was segmented using Linear diffusion (section 5.2.1). The segmented image acted as a mask and was multiplied with the maximum projection of the convolved stack to remove out-of-focus blur. To evaluate the result of the removal, the correlation coefficient between the intensity of the original unconvolved maximum projection and the intensity of this new image was compared. The segmentation procedure slightly altered the location of the boxes due to the asymmetric shape of the PSF. However, the intensities and the number of segmented pixels in the original maximum projection and the convolved seemed to correlate well (see Table 6.3).**(a)** shows the maximum projection of the original image (i.e. the reference) prior to convolution. **(b)** Maximum projection of the convolved stack. **(c)** Segmented result. **(d)** The boundary of the original boxes (green) superimposed on the segmented result.

6.5 Validation of Relative Invasion parameter

To verify that the automatic measurement of RI was accurate we analysed six cells at two time points, in total 12 measurements manually where we fitted ellipses to the cell data of each plane in the stack. Ghodsnia *et al* [49] previously used a similar method to quantify the invasion. The image stacks were first inspected visually using ImageJ (NIH, USA) to locate the coverslip and the upper surface of the monolayer. The desired region was examined for the z-level that was sharpest which, represented the surface of the monolayer. The top of the sarcoma cell was determined by investigating where the cell signal faded. An ellipse was fitted manually to the outline of the sarcoma cell (an example is shown in Fig. 6.11) at each z-level and the area of each ellipse was calculated respectively. The sum of these areas represented the volume of the cell. To determine RI manually, the volume below the surface divided by the entire volume was used as measurement. The comparison between manual and automatic measurements is shown in Table 6.4 and the measurements seem to correlate well (Pearson r=0.89, p-value<0.005).

Figure 6.11: **Example of manual fitting of an ellipse to the intensity in a z-plane of a TC stack.** An ellipse was fitted manually to the intensity of each z-plane. The area of each z-plane represented the volume of a cell which was used to quantify the invasion and as a validation of the *RI*. The manual *RI* was quantified as the volume below the surface in relation to the entire cell volume.

		RI	
Cell id	Time (min)	Manual	Our method
s2c	30	0.27	0.28
	90	0.51	0.52
s3c	30	0.46	0.44
	90	0.52	0.65
s4c	30	0	0
	90	0.82	0.71
s6f	30	0.50	0.53
	90	0.41	0.52
s12f	30	0.52	0.46
	90	0.52	0.63
s16f	30	0.25	0.27
	90	0.64	0.54

Table 6.4: **Comparison of semi-automatic estimation of *RI* with manual estimation.** *RI* was compared to manual estimation in order to test its accuracy. The manual values were obtained by inspecting selective intensity stacks for cell signal and monolayer surface manually and the number of slices a TC covered above and below the surface was calculated and shown to correlate well (Pearson r=0.89, p-value<0.005).

Chapter 7

Experimental results

Our direct viewing assay used a flow chamber with a custom-made Nylon insert fitting tightly into a 35 mm glass-bottom MatTek dish as shown in Fig. 3.2. Such a design allowed for convenient cell culturing of the monolayer and assembly of the chamber. The glass-bottom dish enabled the specimen to be viewed in high-resolution fluorescence microscopy. The chamber comprised an inlet and outlet, a flow channel and an aperture in the centre to allow for easy introduction of sarcoma cells in suspension. The inlet and outlet were connected to a peristaltic pump to provide shear flow in the chamber.

We have used $OREM$ and RI to investigate the modulation of cancer-cell invasion under flow. Lymphocytes express increased invasiveness during exposure to flow [115] and it was believed that TCs would have similar behaviour. To evaluate this, we conducted two types of experiments: one where cells did not experience the shear forces and one in which the flow was present. The invasiveness was quantified by two parameters, $OREM$ and RI, which combined provided evidence for flow-mediated invasion of TCs. $OREM$ targeted the initial opening of the monolayers and RI quantified the TC invasion. We also conducted statistical measurements on these

parameters to support the quantitative studies.

7.1 Experimental set-up

7.1.1 Cell culture

Our direct viewing assay required two cell types: sarcoma cells in suspension and endothelial cells that formed confluent monolayers. Sarcoma cells, T15 and K2, were derived from inbred rats [52]. The sarcoma cells were maintained in MEM with Hanks salts supplemented with 10% bovine serum (SML, Germany), 0.09% sodium bicarbonate, 0.12 g/l Na-pyruvate (Sigma) and 1 mM glutamine, at 37°C with 5% CO2 using vented 25 cm^2 tissue culture flasks. Cells were detached from flasks by brief exposure to trypsin-versene solution (1:5) and suspended in 37°C phenol red-free medium prior to recording. Cells were not used beyond passage 14. Rat brain endothelial cells RBE4 were obtained as a kind gift from Professor Joan Abbott, Centre for Neuroscience Research, GKT School of Biomedical Sciences, King's College London, UK. Stock RBE4 cells were cultured in vented 25 cm^2 collagen-coated BD BioCoat flasks (Becton Dickinson Labware, Two Oak Park, Bedford, UK) with medium containing 45% Hams F 10 (GibcoBRL), 45% α MEM (GibcoBRL), 10% foetal calf serum (Sigma), 1mM Glutamax-1 (Invitrogen), 1 ng ml-1 bFGF (Boeringer) and 100 mg ml-1 Geneticin (Sigma) and then seeded at a concentration of 2×10^4 on 35 mm glass-bottom culture dishes pre-coated with type I collagen (MatTek Corp., MA, USA). Confluence was reached after five days of incubation at 37°C with 5% CO2. Early experimentation suggested that higher seeding densities lead to confluence in a shorter time period (e.g. two to three days), but the resulting layer did not remain intact under flow. A period of five days was established as being a suitable time period for strong cell adherence under flow conditions.

7.1.2 Cell labelling

The sarcoma cells were labelled with 10 μM green Vybrant DiO solution (Invitrogen, USA). The supplied solution was diluted in 2 ml of the culture medium then placed into a nearly confluent flask with approximately 2×10^6 sarcoma cells, which were subsequently incubated for 15 min at 37°C. The cells were then washed with pre-warmed medium and trypsinised. The sarcoma cells were then suspended in phenol red-free medium ready to be introduced into the flow chamber. The endothelial cells were labelled by a new protocol we developed using CellTracker Orange CMTMR (Invitrogen Ltd). Fig. 7.1 is an example of a monolayer labelled according to the new procedure.

Figure 7.1: **Example of an image of an endothelial monolayer at the in-focus position of a stack labelled with the described technique.** The described procedure for surface labelling provided excellent surface definition and prolonged photostability.

In order to assess the invasion by sarcoma cells, the surface membrane of the endothelial cells needed to be labelled uniformly and specifically without significant internalisation and cross-leakage to the invading sarcoma cells for long time periods. In order to meet these requirements, we developed a new labelling procedure for a commercially available cell dye, CellTracker Orange CMTMR (Invitrogen Ltd). The labelling reagent was diluted to a 100 μM concentration in high-quality DMSO

(Sigma), aliquoted into 100 μl units and kept at -20°C for at least 2 weeks before use. For labelling, 30 μl of the prepared reagent was evenly spread over the adherent monolayer of endothelial cells in a MatTek dish with 2 ml of culture medium and mixed using a pipette. The adherent cells were then incubated for 5 min at 4°C and subsequently washed twice with pre-warmed medium and incubated for another 15 min at 37°C. This technique provided prolonged photostability and excellent definition of the endothelial cell monolayer surface.

7.2 Results

7.2.1 Novel flow chamber assay with image-processing-based quantitation

We devised two new imaging-based parameters to quantify the invasion process using z-stacks of images of labelled cells in the flow chamber acquired by time-lapse fluorescence microscopy. The first parameter, RI, measured the penetration of the monolayer of endothelial cells by a sarcoma cell. The RI parameter was calculated as the ratio of the sum of the projected signal of an invading sarcoma cell below the upper monolayer surface over the total projection signal in the stack of sarcoma-cell images.

The second parameter, $OREM$, quantified the change in the fluorescent signal of the endothelial cells in a 4 μm$\times$ 4 μm area where invasion occurred. In this area, the signal was measured from the minimum projection of the image z-stacks of endothelial cells for each time point. The decreasing intensity was normalised over the monitoring period and thus comparable with other experiments.

7.2.2 Metastatic sarcoma cells invade the monolayer of endothelial cells by creating openings between endothelial cells while non-metastatic sarcoma cells do not

The newly developed invasion assay was used to study the invasion of metastatic rat sarcoma cells T15 into monolayers of rat brain endothelial cells over a time period of 90 min. We observed the sarcoma cells invading the monolayer by inducing openings between the endothelial cells from as early as 15 min after initial adherence to the monolayer. The invading sarcoma cells extended underneath the surface of the monolayer Fig. 7.5 a. An example of a 3D-reconstruction of an adhering sarcoma cell and an invading sarcoma cell interacting with a monolayer of endothelial cells is shown in Fig. 7.5 b and Fig. 7.5 c. Sarcoma cells were also observed to have almost completely invaded underneath the surface of the monolayer as shown in the 3D-rendering of confocal images in Fig. 7.2.

In addition we applied the invasion assay to compare the invasion potential of another sarcoma cell population K2. It was previously reported from *in vivo* experiments that the T15 sarcoma cells have a significantly higher metastatic potential compared to the non-metastatic K2 sarcoma cells [74]. Using our direct viewing invasion assay, we observed that there was no invasion into the monolayer of endothelial cells by the non-metastatic K2 sarcoma cells in two experiments without flow.

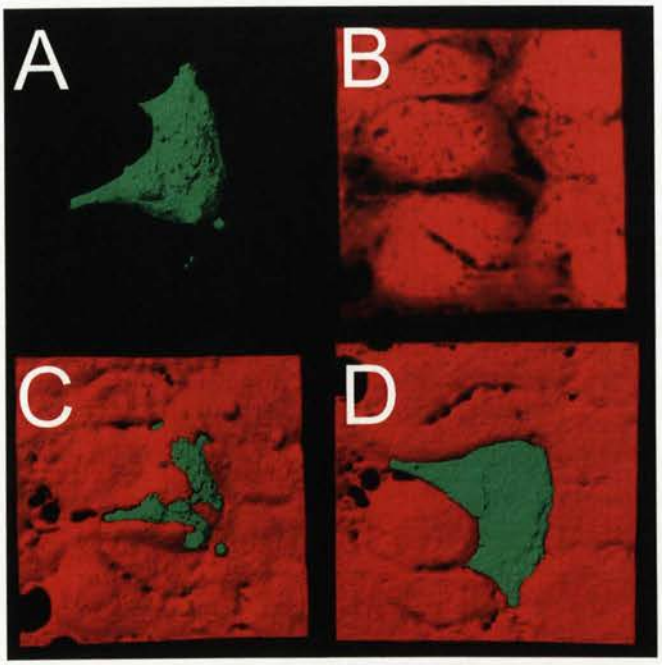

Figure 7.2: **Images of a sarcoma cell invading a monolayer of endothelial cells without flow where the sarcoma cell had invaded almost completely underneath the surface of the monolayer.** The images present renderings of a z-stack of images (field size 73μm×73μm) acquired from 50 z-levels at 0.2 μm separation by a laser-scanning confocal microscope LSM 510 (Carl Zeiss MicroImaging GmbH, Jena, Germany). Endothelial cells labelled with CellTracker Orange CMTMR were imaged using a 543 nm line of a HeNe laser and are represented in red, and the sarcoma cell labelled with green DiO was imaged using a 488 nm line of an Argon laser and is represented in green. (A) Shows the isosurface rendering of the sarcoma cell. (B) presents the maximum-intensity projection of the endothelial monolayer where the individual cells and openings between them can be identified. (C) and (D) show the top view and the bottom view of combined isosurfaces. The images were rendered using Imaris (Bitplane AG, Switzerland).

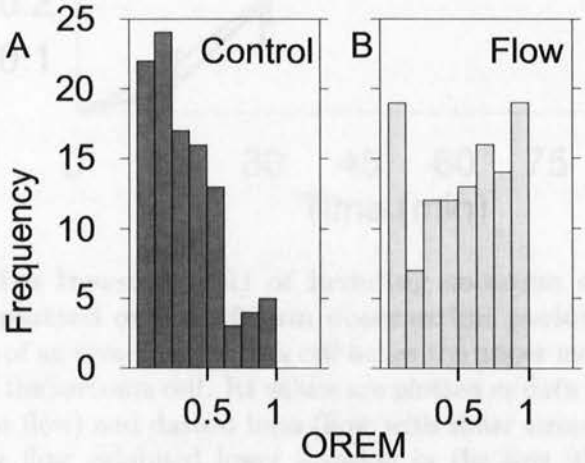

Figure 7.3: **Histograms of sarcoma-cell induced Opening Rate of the Endothelial Monolayer (OREM) between 0 and 30 min in conditions without and with flow.** The control cells without shear flow showed a decreasing trend of the number of cells with increasing opening rate (Pearson correlation P value < 0.01). The sarcoma cells exposed to flow showed an increasing trend of the number of cells with increasing opening rate with the exception of a small subset of late-responding cells which did not exhibit any activity during this initial period. The statistical significance of the difference between the two groups is presented in Table 7.1. The total number of evaluated cells was 104 without flow and 112 under flow.

7.2.3 Non-linear invasion response to shear flow

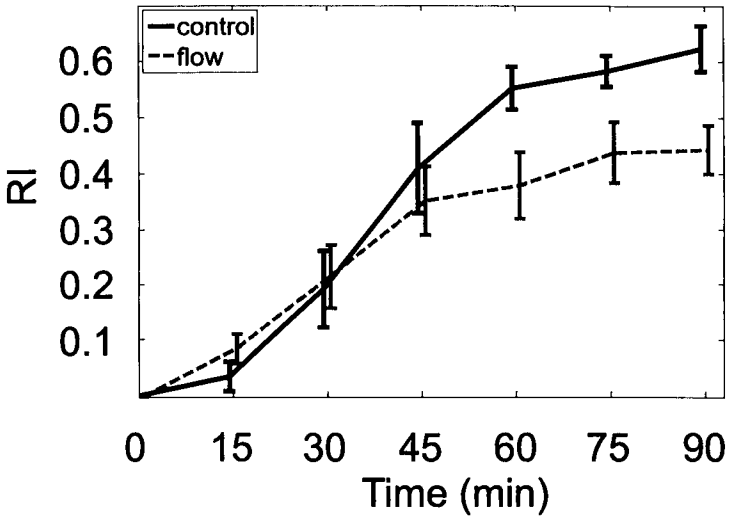

Figure 7.4: **Relative Invasion (RI) of invading sarcoma cells without and with shear flow plotted over a 90 min observation period.** *RI* measures the ratio of the volume of an invading sarcoma cell below the upper monolayer surface and the total volume of the sarcoma cell. RI values are plotted as data points connected by solid lines (no shear flow) and dashed lines (flow with shear stress). Control sarcoma cells without shear flow exhibited lower invasion in the first 45 min compared to sarcoma cells exposed to shear flow. The significant difference of the invasion rate at this early stage is described in Table 7.1. Later on, the situation reversed and the control cells showed a significantly higher level of invasion in comparison to the sarcoma cells exposed to shear flow. Graph represents data from nine control cells without flow and 13 cells under flow conditions. Error bars represent standard errors of the mean.

To quantitatively assess the invasion process, we calculated RI values for the invading sarcoma cells. Fig. 7.4 shows a graph of *RI* values plotted as connected data points for control experiments and flow experiments with shear stress over 90-min observation period. Sarcoma cells without shear flow exhibited lower mean invasion in the first 30 min compared to sarcoma cells exposed to shear flow. After 30 min, the situation changed and the sarcoma cells without flow eventually showed significantly higher levels of invasion in comparison to the sarcoma cells exposed to shear flow. Mean $\pm$ standard error values of *RI* at 90-min time point were 0.6226 $\pm$ 0.0408 (N

= 9) for no flow and 0.4430 ±0.0432 (N = 13) for flow conditions (Mann-Whitney P-value $\leq$ 0.014). This indicated that shear flow stimulated the sarcoma-cell invasion in the early stages but the sarcoma cells could not sustain this activity over long periods. The level of invasion significantly decreased during prolonged exposure to shear flow in comparison with the control situation without flow.

To assess whether shear flow influenced significantly the initial part of the invasion process, i.e. the opening of monolayers, the OREM parameter was calculated for the time interval between 0 and 30 min after the acquisition began. Sarcoma cells exposed to shear flow expressed overall higher OREM compared to sarcoma cells without shear flow. The incidence of sarcoma cells with high ($\geq$ 0.5) and low ($\leq$ 0.5) OREM values are shown in Table 7.1. In the three paired experiments, the incidence of sarcoma cells with high OREM was significantly increased under shear flow (Chi^2 P-value $\leq$ 0.005) compared to a situation without flow.

The standard error was calculated as

$$SEM = \frac{\sigma}{\sqrt{n}} \tag{7.1}$$

where σ is the standard deviation and n is the number of sarcoma cells.

The segmentation algorithm using Linear diffusion segmented the parts of the TC which were brighter with respect to its neighbours as described previously (see section 5.2.1). Fig. 7.7 shows graphs of the number of segmented pixels above and below the surface in two different situations: one used as a control experiment without shear flow and the other with applied shear forces. The number of segmented pixels varies between the two experiments and is much lower in the control experiment. This is caused by the quality of the labelling being different. In one situation, labelled flow in Fig. 7.7, the mitochondria was well labelled which produced good separation

Table 7.1: **The incidences of sarcoma cells with high (>= 0.5) and low (< 0.5) Opening Rates of the Endothelial Monolayer (*OREM*) under conditions without and with shear flow from three paired experiments.** The *OREM* values were calculated from data acquired at 0 and 30 min time points in the experiments using a total number of 104 cells without flow and 112 cells with flow. In each of the three paired experiments, the incidence of sarcoma cells with high *OREM* was significantly higher under shear flow (χ^2 p-value < 0.01).

OREM value	< 0.5			>= 0.5		
Experiment no	1	2	3	1	2	3
Control incidence	24	29	26	6	9	10
Flow incidence	19	18	13	21	21	20

between the labelled areas, resulting in more pixels classified as part of the cell. The increasing trend in numbers over time reflected the increase in invasion. However, counting the absolute number of segmented pixels is not an accurate measurement of invasion since it is influenced by the performance of the labelling technique. It is therefore heavily biased and thus not comparable between different experiments.

We also investigated the spreading of the sarcoma cells. Chothard-Ghodsnia *et al* [49] assessed the spreading by manually fitting an ellipse around the outline of the cell. In their study, TCs experienced increased axial spreading when exposed to flow. This can be explained by the shear forces pressing on to the cell. A sarcoma cell mostly exhibited a round or elongated shape which made an ellipse well suited. This approach was adopted with some modifications. An ellipse was fitted [5] automatically to each of the maximum projections above and below the surface of the monolayer.

The parameters given from the fitting which described the ellipse were used to assess the spreading. The average number of segmented pixels (Fig. 7.7) could also be interpreted in terms of spreading. Because the TC signal represented mitochondria, a small number of segmented pixels would then represent a cell with a tight boundary. As the cell spread the mitochondria were separated from their neighbours and resulted

in cell signal with a higher number of segmented pixels. The rate of spreading was lower in situations without flow compared to shear experiments and the spreading above the monolayer in conditions with flow was higher initially compared to below but later on reached similar levels. A similar trend was found in Fig. 7.6. This can be explained by the shear forces pressing on the upper parts of the cell which squeezed the cell towards the surface. This event is particularly evident in the beginning because the cell is fairly upright. The decline in speed of this event occurred when TCs were flat and close to the monolayer as TCs reached their minimum height. The spreading in control experiments, however, showed a steady increase both above and below the upper surface and may be related to the stress-free environment the control experiments provided.

However, the absolute values cannot be compared in terms of spreading due to variation in the performance of the cell labelling between the cells.

The relative spreading (RES) below the monolayer was also investigated to address this problem. The fitted ellipse below the monolayer was compared to an ellipse fitted to all segmented pixels in all time points (see Fig. 3.8). The spreading followed in principle the pattern of RI. During the first 75 min, cells exposed to flow exhibited a higher mean spreading below the monolayer compared to situations without flow. This can possibly be related to the increased invasiveness flow had on TCs where TCs try to exit the flow channel (see Fig. 7.8). Experiments without flow showed a steady increase throughout the observation period. Such situations provide the invading cells with a stable environment in which they can invade uninterrupted. With shear forces, however, the environment is uncomfortable and the cells consume energy in their strive to escape these conditions. The rate of spreading above the monolayer was also higher with shear compared to situations without, which would indicate that shear forces pressed on to the TCs and created unpleasant surroundings which they

were ready to avoid. The decrease in spreading between 75 and 90 min (see Fig. 7.8) could possibly be explained by lack of energy. *RI* also expressed a decrease in a similar manner. The cell labelling technique with prolonged photostability used the mitochondria as a carrier of the fluorescence. However, mitochondria are important in the production of cell energy within the cell [116]. Early experimental set-ups included long periods of fluorescent excitation and for these samples, invasion was rarely seen. This may have been caused by interference in energy production by the labelling/fluorescence emission. Later experiments with shorter periods of fluorescence excitation showed more invasion, possibly explained by less interference and increased energy levels.

The control experiments without flow express a steady increase in spreading, similar to the invasion of control cells (see Fig. 7.8 and Fig. 7.4).

Some may argue that the invasion parameter *RI* actually reflects lateral spreading above the monolayer, i.e. the quantity of *RI* does not show invasion but actually spreading. This would be caused by the TCs spreading to be very thin and because of the limited z-resolution, the signal lands on the "incorrect" side of the monolayer surface occupying z-levels below the monolayer. An increased spreading also increased the amount of visible mitochondria which could then be mistaken for an increased invasion. To investigate this, we compared Fig. 7.8 and Fig. 7.4 which showed that Relative Spreading (*RES*) also has a non-linear behaviour under flow conditions. However, the cross-over occurred much later in time compared to *RI* and the spreading was therefore not related to the invasion. The morphology between the two types of experiments was also compared to determine the spreading patterns and found that cells in both experiments exhibited similar shape. (see Fig. 7.9).

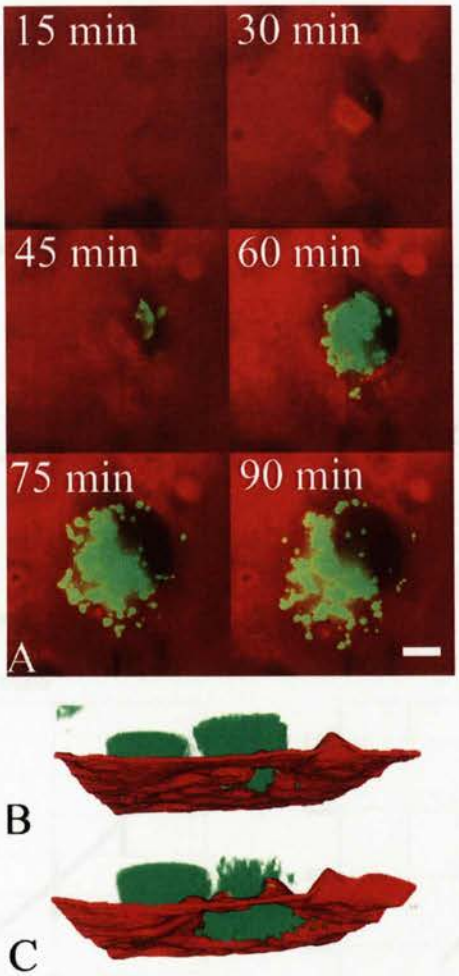

Figure 7.5: **Images illustrating sarcoma cells invading monolayers of endothelial cells.** Endothelial cells labelled with CellTracker Orange CMTMR, using the protocol described in 7.1.2, are represented in red and sarcoma cells labelled with Vybrant DiO solution are represented in green. The Vybrant DiO dye produces punctate staining throughout the cytosol. (A) presents images from a time-lapse recording of a sarcoma cell invading a monolayer of endothelial cells. Images of the endothelial cells show minimum z-projections and images of the sarcoma cell show maximum z-projections of optical sections obtained between the surface of the monolayer and the substrate. The invasion was monitored over 90 min and the sarcoma cell was found to partially extend under the monolayer after 30 min. Scale bar represents 5 μm. (B) and (C) show 3D-reconstructions, at early and late stages of invasion respectively, of an adhering sarcoma cell (left) and an invading sarcoma cell (right) interacting with a monolayer of endothelial cells. The raw data were acquired as stacks of wide-field images. The surface of the endothelial cells was reconstructed by locating the in-focus level at each <x,y> position. The images of the sarcoma cells were processed by high-pass filtering and soft thresholded to reduce out-of-focus blur. The images were pre-processed by custom-developed software in MATLAB and the resulting data were presented using Volocity (Improvision Inc) .

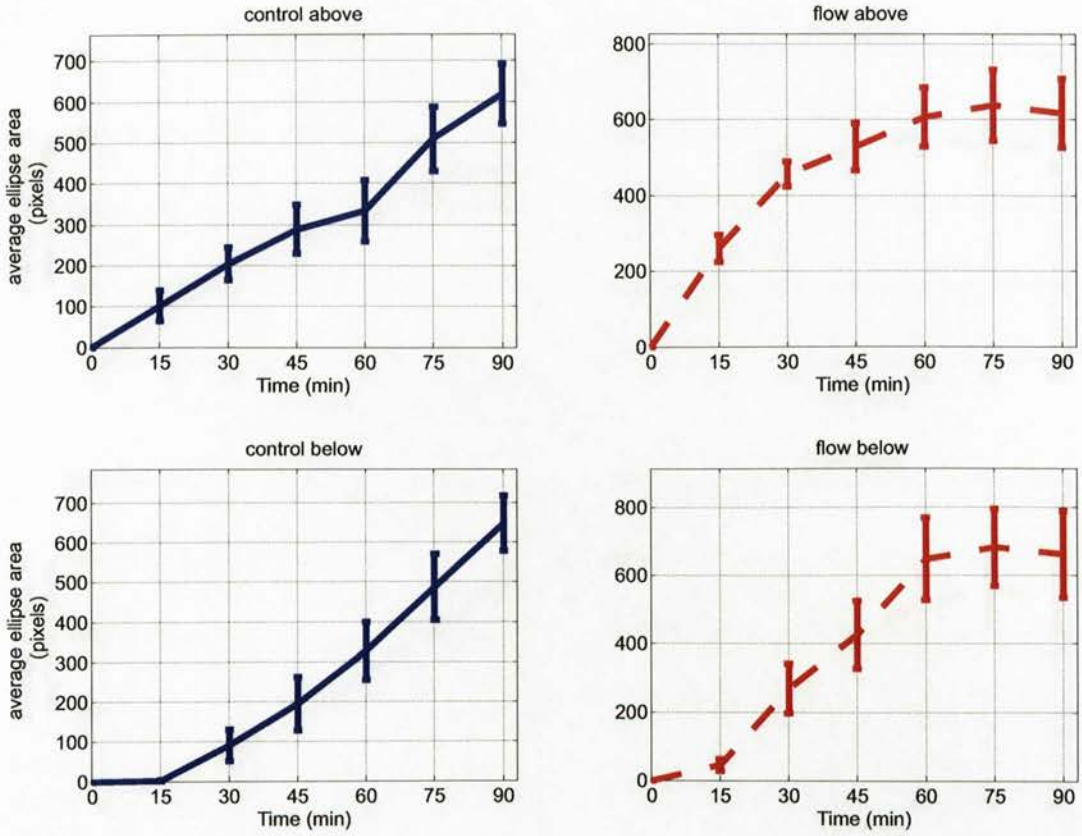

Figure 7.6: **Average area of the fitted ellipses above and below the monolayer.** Ellipses were fitted to the segmented pixels above and below the monolayer in MATLAB [5] and the area of these was computed. The experiments without flow expressed a higher rate of spreading both above and below the monolayer in the earlier stages. After a while, the situation reversed and the cells exposed to flow could not sustain the pace of spreading. Note that the actual area cannot be compared because the performance of the labelling technique may vary between cells.

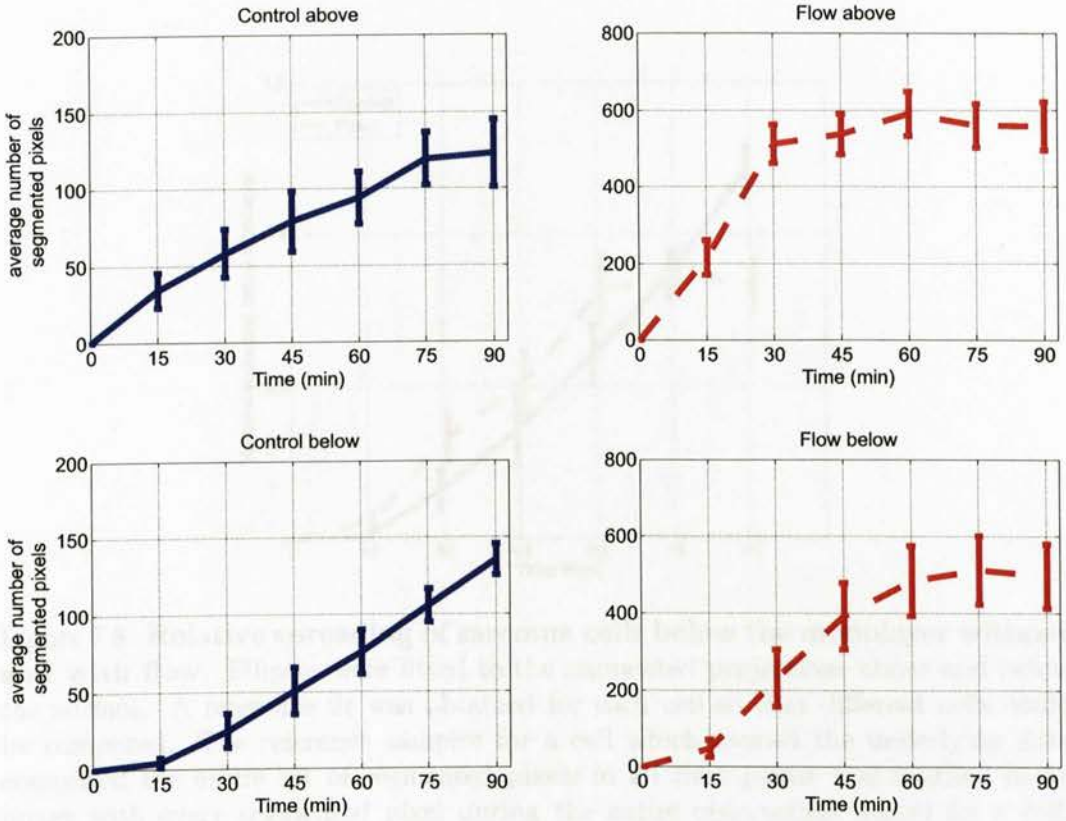

Figure 7.7: **Average number of segmented pixels of a sarcoma cell over a 90-min time period.** The numbers of segmented pixels from the two experimental situations (control and flow) are different. Situations with flow have a higher amount compared to control. The amount of labelling substances attached to the mitochondria was different and therefore produced different segmentation results. The error bars represent the standard errors of the mean (Eq. 7.1).

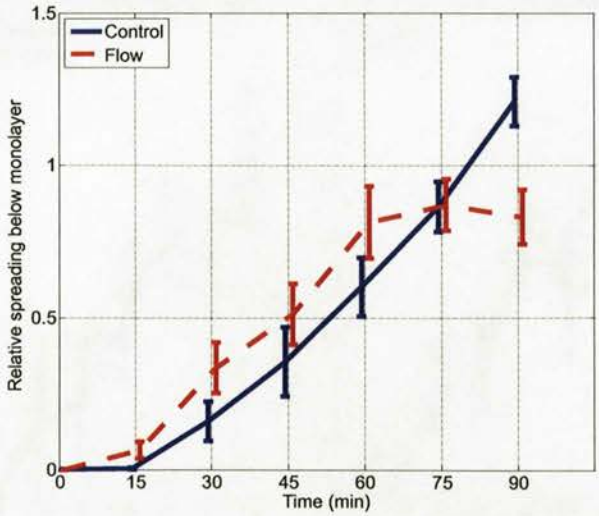

Figure 7.8: **Relative spreading of sarcoma cells below the monolayer without and with flow.** Ellipses were fitted to the segmented projections above and below the surface. A reference fit was obtained for each cell so that different cells could be compared. The reference samples for a cell which formed the underlying data comprised the entire set of segmented pixels in all time points and resulted in an image with every segmented pixel during the entire observation period for a cell. An ellipse was fitted to this set and acted as a reference. The fitted ellipse of the segmented pixels for each time point was then divided by the reference. One detail to note is that the Relative Spreading may have a value > 1 because the area of the reference ellipse can be smaller than the area of each time point. Error bars represent standard error of the mean.

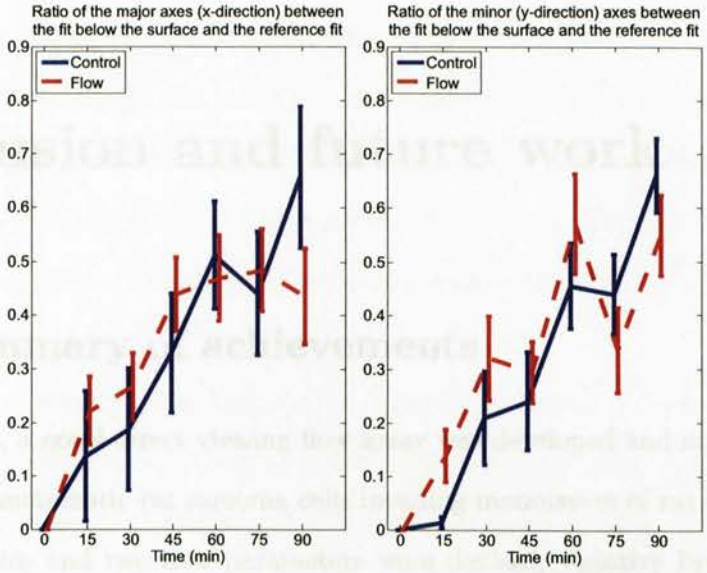

Figure 7.9: **Ratio of major/minor axis below the monolayer.** The spreading of cells, described by the major and minor axis, was investigated below the monolayer surface. An ellipse was fitted to all segmented pixels for a cell during all time points and used as a reference. The major or the minor axis for each individual cell was divided by the respective axis of the reference fit (x/x_{ref},y/y_{ref}) in two experimental situations to depict the shape changes that may have occurred. A value of one indicates that the shape of the reference fit and the individual cells are the same. The value at the first acquisition time point (0 min) is zero because sarcoma cells were introduced after the first acquisition time point. The spreading patterns in control and flow experiments were similar. Error bars represent standard error of the mean.

Chapter 8

Conclusion and future work

8.1 Summary of achievements

In this project, a novel direct viewing flow assay was developed and applied to an investigation of metastatic rat sarcoma cells invading monolayers of rat brain endothelial cells *in vitro* and two new parameters were devised, Relative Invasion RI and Opening Rate of the Endothelial Monolayer $OREM$, to quantify the invasion. The novel shear flow assay with a newly developed flow chamber provided a set-up where the cancer cell invasion *in vitro* could be assessed objectively and semi-automatically by measuring the sarcoma-cell signal during the invasion process. This assay comprised a custom-made flow chamber, specially developed cell labelling and image-processing-based quantitation of cell invasion. This assay was applied to metastatic sarcoma cells derived from an inbred rat model where the cells invaded monolayers of rat endothelial cells. This approach required new techniques to restore the monolayer surface as well as segmentation of tumour cells.

The areas where the invasion took place usually incorporated confluent monolayers but tumour cells disrupted the confluence on their path to exit the flow chan-

nel by pushing the endothelial cells aside. The cell signal of the monolayer inside the void that occurred as a result produced unreliable monolayer readings which were influenced by neighbouring out-of-focus information. The invaded areas needed to be identified and replaced by interpolated values in order to calculate the Relative Invasion correctly. The identification of unreliable regions investigated the rate of convergence during iterative convolutions which was based on Linear diffusion. The segmentation utilised this property and explored the fact that unreliable regions would exhibit a positive diffusion rate during iterations. The diffusion process over-segmented the monolayer slightly because the diffusion explores the changes related to neighbouring pixels. The sign of the change varies depending on the behaviour of the neighbourhood.

The surface interpolation replaced the unreliable values in invaded areas with values from a Radial Basis Function (RBF) interpolation. The interpolation solves a linear system where the distance from each point to every other point is weighted by the RBF. The RBF is a radially symmetric function and acts as a weighting function to the distance between the points. The result of the weighting function is that points close to each other have a higher impact on the interpolation value than values far away. This allows the interpolated surface to acquire a non-linear shape, similar to that of a monolayer surface. From the reconstruction, the cell signal values above and below the reconstructed surface were used to calculate the Relative Invasion.

The Relative Invasion was quantified as the percentage of cancer-cell signal below the monolayer and $OREM$ as the rate at which tumour cells open the monolayer between 0 and 30 min into the experiment. The sarcoma cells exposed to shear flow expressed a significantly higher rate of invasion after the first contact with the endothelial monolayer compared with sarcoma cells not exposed to shear flow. However,

after 30 min the sarcoma cells with no shear forces exhibited higher levels of invasion, eventually achieving significant differences. This non-linear response to shear flow has not been reported previously.

8.2 Discussion

The system described in this thesis provided an improvement to manual assessment of cancer-cell invasion *in vitro* because of its objective assessment. In previous studies, the effect of shear flow on the invasion process was quantified by means of counting and/or manual quantification of the cells that had invaded in transwell [16] [39] or parallel-plate chambers [49]. In static experiments, the invasion has been quantified manually by visualising the cell volume from confocal stacks and providing each individual cell with a score [50]. Our flow chamber invasion assay allowed the analysis of invading tumour cells in high-resolution 3D wide-field microscopy using image-processing-based quantitation. The analysis was validated by inspecting the image stacks and calculating the cell volume manually. The assessment of the invasion process under flow conditions was made right from the moment shear flow was applied. The endothelial cell surface reconstruction enabled the quantitation of the levels of invasion from the signal of the invading sarcoma cells at consecutive time points. The sarcoma cells invaded the endothelial monolayer by opening gaps between endothelial cells. Our observations were also evaluated through our second measurement parameter, the Opening Rate of the Endothelial Monolayer. The evaluation of the two image-processing-based parameters in combination revealed the non-linear invasion response of sarcoma cells to shear stress.

Dong et al. [39] reported a decreasing number of invading tumour cells exposed to shear forces in relation to situations with no shear using transwell assays while count-

ing the cells that had invaded. Although a reduction of invasion with our sarcoma cells at later time points was observed, the results described here showed that the flow can stimulate the metastatic sarcoma cells to higher rates of invasion in a similar way to white blood cells, such as neutrophil leucocytes [117] and lymphocytes [115]. This observation can be explained by shear stress initially activating signalling pathways, which induce changes in cell motile behaviour. This proposed hypothesis is supported by some reports. Chotard-Ghodsnia et al. [49] used time-lapse fluorescence microscopy to manually classify and measure the cell behaviour under shear forces and concluded that the extent of tumour-cell spreading was increased by shear flow in a similar way to leukocytes, which increased pseudopodia activity while exposed to flow [118]. Changes in endothelial polarisation and migration in response to shear stress were also described by Wojciak-Stothard et al. [119]. In addition, esophageal tumour cells expressed a similar behaviour where shear forces increased the lamellipodia activity compared to no shear [120]. Furthermore, the authors reported an increase in the invasiveness of these tumour cells using a Boyden chamber assay after cells had been pre-exposed to shear flow. In their study, cells were not exposed to shear flow during the invasion process. Signalling pathway activation by mechanical forces was also reported by Bershadsky et al. [121] who found induction of DNA synthesis as a consequence. Our assay showed that the higher rate of the invasion process is not sustained under flow, which indicates that the shear-stress-activated signalling may be transient. The fact that the cells under control conditions without flow eventually achieve higher invasion might be explained by a gradual accumulation of more proteolytic enzymes in their local microenviroment than under flow conditions. This is a plausible explanation since proteolytic activity was shown to be increased in the metastatic cells T15 compared to the non-metastatic cells K2 [122] and has been shown to play a general role in invasion and metastasis [123] [124]. Also, the type

of endothelial cells that interact with the tumour cells may also play a part in the invasion. It is, for example, known that some tumour cells metastasise to certain organs. The capillary endothelial cells show heterogeneity in different organs which may attract different types of metastasing cells. This may be depending on the type of adhesion molecules that the endothelial cells express [125].

The time of the initiation of the invasion observed was similar to that of previous studies in related processes. Peng et al. [35] reported that human melanoma cells begin the opening of gaps in the endothelial monolayer after 45 min and Lewalle et al. [33] observed the invasion through the opening of gaps between endothelial cells after 30 min. Experiments in vivo show that rat colon carcinoma cells adhere 15 min after intravenous injection [126].

It has been reported that lymphocytes can use a transcellular route in order to extravasate [127] and this phenomenon is linked to certain proteins. Carman *et al* [78] explain that adhesion molecules are involved in the migration of e.g. monocytes across ECs and act as a guide for the invasive cells. If the assumption can be made that TCs have similar behaviour, these events would occur. However, transcellular invasion was not observed.

8.3 Future work

The work in this thesis sets the ground and offers paths for exploring new areas.

The effect of shear forces on lymphocytes [115], leukocytes [128] and neutrophils [117] have been examined in previous studies and provided evidence that flow alters the invasion rate. The highest invasion occurred during continuous, steady flow and a decline for monocytes was clearly observed at the point of switch between no flow and flow. Similar paths regarding sarcoma cells could be explored. Additional permu-

tations could be added such as different pulsating flow strengths of different lengths and rate to explore these properties further. The invasion of e.g. lymphocytes is, in some sense, insensitive to the magnitude of the shear but, rather, the presence of shear acts as the main activator for the increase [115]. Investigating this further would reveal any similarities.

The system described here would benefit from an automatic instead of a semi-automatic assessment. That includes automatically locating the tumour cells in an image stack and then segmenting it in 3D. This would eliminate the user-guided component of selecting the cells manually, which would increase the speed of the analysis. It also allows for a more accurate estimation of the invasion since the analysis would be performed in three dimensions. Problems that then would arise are accurate segmentation of closely located cells, reducing blur within the cell volume so that RI can be estimated and segmenting weakly labelled cells. The cells - in some instances - settle close to each other and interfere. Determining which part belongs to which cell needs to be solved. This would also be an issue with weakly labelled cells. This would allow for high-content screening of invading cells.

It would also be an advantage to segment the individual cells of the monolayer. This would allow for a more detailed study of the interaction with sarcoma cells. The benefits are that more analysis parameters of the cell behaviour can be obtained. Invading cells are known to push the endothelial cells aside in their strive to exit the flow channel. Segmenting individual endothelial cells would easily explain if sarcoma cells target specific parts of the monolayer or if the invasion pattern changes due to e.g. treatments. One complication includes locating the individual cells as the borders between them are weakly defined. Segmenting individual endothelial cells

would add an extra component to the analysis and allow for more details about the invasion process to be explored.

8.4 Final words

The quantitative image-processing flow assay described a development of a novel direct viewing flow assay on the basis of live cell imaging and new quantitative image-analysis techniques. This assay enabled measurements of the invasion of individual sarcoma cells into monolayers of endothelial cells exposed to shear flow. It was found that cells from a non-metastatic population were not able to invade into the endothelial monolayer. Experiments with the metastatic cells showed that shear forces significantly increased the initial sarcoma-induced invasion into the monolayers of endothelial cells. The invasion of sarcoma cells under flow conditions expressed a non-linear behaviour whereby the rate of invasion increased initially but later decreased over time compared to a situation without shear. This system showed that metastatic cancer cells can be stimulated to enhance extravasation by shear flow in a similar way to white blood cells. With this system it is possible to investigate the invasion behaviour of metastatic cells in response to treatments.

References

[1] N. Otsu, "A threshold selection method from gray-level histograms," *IEEE Trans on Systems, Man And Cybernetics*, vol. 9, no. 1, pp. 62–66, 1979. xvi, xix, 62, 77, 94

[2] E. Stelzer, "Contrast, resolution, pixelation, dynamic range and signal-to-noise ratio: fundamental limits to resolution in fluorescence light microscopy," *J Microsc*, vol. 189, no. 1, pp. 15–24, 1998. xvi, 63, 64

[3] M. H. DeGroot and M. J. Schervish, *Probability and statistics.* Addison-Wesley, 3rd ed., 2002. xvi, 64

[4] P. Tsui, *Fast EM GM.* Matlab File Exchange, accessed 2008-08-20. xvii, 67, 68

[5] R. Halir and J. Flusser, "Numerically stable direct least squares fitting of ellipses," in *The Sixth International Conference in Central Europe onComputer Graphics and Visualization*, pp. –, 1998. xxix, 49, 138, 142

[6] A. Ahmad and I. R. Hart, "Mechanisms of metastasis," *Crit Rev Oncol Hematol*, vol. 26, no. 3, pp. 163–173, 1997. 1

[7] T. Meyer and I. R. Hart, "Mechanisms of tumour metastasis," *Eur J Cancer*, vol. 34, no. 2, pp. 214–221, 1998. 1

[8] L. A. Liotta, "Cancer cell invasion and metastasis," *Sci Am*, vol. 266, pp. 54–63, 1992. 1, 5

[9] I. J. Fidler, "Critical factors in the biology of human cancer metastasis: Twenty-eighth G. H. A. clowes memorial award lecture," *Cancer Res*, vol. 50, pp. 6130–6138, 1990. 1, 5

[10] T. Sobue, T. Suzuki, M. Matsuda, T. Kuroishi, S. Ikeda, and T. Naruke, "Survival for clinical stage i lung cancer not surgically treated," *CANCER*, vol. 69, pp. 685–692, February 1992. 5

[11] L. A. Liotta, J. Kleinerman, and G. M. Saidel, "Quantitative relationships of intravascular tumor cells, tumorvessels, and pulmonary metastases following tumor implantation," *Cancer Res*, vol. 34, pp. 997–1004, 1974. 5

[12] I. J. Fidler, "Metastasis: Quantitative analysis of distribution and fate of tumor emboli labeled with ^{123}i-5-lodo-2'-deoxyuridine ^{1,2,3}," *Journal of the National Cancer Institute*, vol. 45, no. 4, pp. 773–780, 1970. 5

[13] D. A. Lauffenburger and A. F. Horwitz, "Cell migration: A physically integrated molecular process," *Cell*, vol. 84, pp. 359–369, Feb 1996. 5

[14] E. C. Woodhouse, L. A. Chuaqui, and L. A. Liotta, "General mechanisms of metastasis," *Cancer*, vol. 80, no. S8, pp. 1529–1537, 1997. 6

[15] S. Boyden, "The chemotactic effect of mixtures of antibody and antigen on polymorphonuclear leukocytes," *J Exp Med*, vol. 115, pp. 452–466, 1962. 6, 7

[16] C. Dong, M. J. Slattery, B. M. Rank, and J. You, "In vitro characterisation and micromechanism of tumor cell chemotactic protrusion, locomotion and extravasation," *Ann Biomed Eng*, vol. 30, pp. 344–355, Mar 2002. 7, 8, 148

[17] S. H. Zigmond, "Ability of polymorphonuclear leukocytes to orient in gradient of chemotactic factors," *J Cell Biol*, vol. 75, pp. 606–616, 1977. 6, 7

[18] D. Zicha, G. A. Dunn, and A. F. Brown, "A new direct-viewing chemotaxis chamber," *J Cell Sci*, vol. 99, no. 4, pp. 769–775, 1991. 6, 7, 8

[19] R. M. Hochmuth, N. Mohandas, and P. L. Blackshear Jr, "Measurement of the elastic modulus for red cell membrane using a fluid mechanical technique," *Biophys J*, vol. 13, no. 8, pp. 747–762, 1973. 7, 9

[20] M. B. Lawrence, L. V. McIntire, and S. G. Eskin, "Effect of flow on polymorphonuclear leukocyte/endothelial cell adhesion," *Blood*, vol. 70, pp. 1284–1290, Nov 1987. 7, 9

[21] R. Chotard-Ghodsnia, A. Drochon, and R. Grebe, "A new flow chamber for the study of shear stress and transmural pressure upon cells adhering to a porous biomaterial," *J Biomech Eng*, vol. 124, pp. 258–261, 2002. 7

[22] J. Cao, S. Usami, and C. Dong, "Development of a side-view chamber for studying cell-surface adhesion under flow conditions," *Annals of Biomedical Engineering*, vol. 25, pp. 573–580, 1997. 7, 9

[23] D. C. Brown and R. S. Larson, "Improvements to parallel plate flow chambers to reduce reagent and cellular requirements," *BMC Immun*, vol. 2, Sep 2001. 9

[24] J. Leyton-Mange, S. Yang, M. H. Hoskins, R. F. Kunz, J. D. Zahn, and C. Dong, "Design of a side-view particle imaging velocimetry flow system for cell-substrate adhesion studies," *J Biomech Eng-T ASME*, vol. 128, pp. 271–278, Apr 2006. 9

[25] L. A. Liotta, "Tumor invasion and metastases - role of the extracellular matrix: Rhoads Memorial Award Lecture," *Cancer Res*, vol. 46, pp. 1–7, January 1986. 10

[26] A. Takada, K. Ohmori, T. Yoneda, K. Tsuyouka, A. Hasegawa, and M. Kiso, "Contribution of carbohydrate antigens sialyl lewis a and sialyl lewis x to adhesion of human cancer cells to vascular endothelium," *Cancer Res*, vol. 53, no. 2, pp. 354–361, 1993. 10

[27] R. Lafrenie, S. G. Shaughnessy, and W. F. Orr, "Cancer cell interactions with injured or activated endothelium," *Cancer Met Rev*, vol. 11, pp. 377–388, November 1992. 10

[28] L. A. Liotta and W. G. Stetler-Stevenson, "Tumor invasion and metastasis: An imbalance of positive and negative regulation," *Cancer Res*, vol. 51, pp. 5054s–5059s, Sep 1991. 10

[29] P.-L. Tremblay, F. Auger, and J. Huot, "Regulation of transendothelial migration of colon cancer cells by e-selectin-mediated activation of p38 and erk map kinases," *Oncogene*, vol. 25, pp. 6563–6573, 2006. 10

[30] M. J. Slattery and C. Dong, "Neutrophils influence melanoma adhesion and migration under flow conditions," *Int J Cancer*, vol. 106, pp. 713–722, Jun 2003. 10

[31] L. Hodgson, A. J. Henderson, and C. Dong, "Melanoma cell migration to type iv collagen requires activation of nf-k b," *Oncogene*, vol. 22, pp. 98–108, Jan 2003. 10

[32] E. Dejana, M. Corada, and M. G. Lampugnani, "Endothelial cell-to-cell junctions," *The FASEB journal*, vol. 9, no. 10, pp. 910–918, 1995. 10

[33] J.-M. Lewalle, K. Bajou, J. Desreux, M. Mareel, E. Dejana, A. Noël, and J.-M. Foidart, "Alteration of interendothelial adherens junctions following tumorcell-endothelial cell interaction in vitro," *Exp Cell Res*, vol. 237, pp. 347–356, 1997. 10, 150

[34] H. Ohigashi, K. Shinkai, M. Mukai, O. Ishikawa, S. Imaoka, T. Iwanaga, and H. Akedo, "*In vitro* invasion of endothelial cell monolayer by rat ascites hepatoma cells," *Jpn J Cancer Res*, vol. 80, pp. 818–821, Sep 1989. 10

[35] H.-H. Peng, L. Hodgson, A. J. Henderson, and C. Dong, "Involvement of phospholipase c signaling in melanoma cell-induced endothelial junction disassembly," *Frontiers in Bioscience*, vol. 10, pp. 1597–1606, 2005. 10, 150

[36] K. V. Honn, D. G. Tang, I. Grossi, Z. M. Duniec, J. Timar, C. Renaud, M. Leithauser, I. Blair, C. R. Johnson, C. A. Diglio, V. A. Kimler, J. D. Taylor, and L. Marnett, "Tumor cell-derived 12(s)-hydroxyeicosatetraenoic acid induces microvascular endothelial cell retraction," *Cancer Res*, vol. 54, pp. 565–574, Jan 1994. 10

[37] G. N. Naumov, S. M. Wilson, I. C. MacDonald, E. E. Schmidt, V. L. Morris, A. C. Groom, R. M. Hoffman, and A. F. Chambers, "Cellular expression of green fluorescent protein, coupled with high-resolution *in vivo* video microscopy, to monitor steps in tumor metastasis," *J Cell Sci*, vol. 112, pp. 1835–1842, 1999. 10

[38] R. H. Kramer and G. L. Nicolson, "Interactions of tumor cells with vascular

endothelial cell monolayers: A model for metastatic invasion," *Proc. Natl. Acad. Sci.*, vol. 76, pp. 5704–5708, November 1979. 10

[39] C. Dong, M. Slattery, and S. Liang, "Micromechanics of tumor cell adhesion and migration under dynamic flow conditions," *Frontiers in Bioscience*, vol. 10, pp. 379–384, 2005. 10, 148

[40] C. Dong, M. J. Slattery, S. Liang, and H.-H. Peng, "Melanoma cell extravasation under flow conditions is modulated by leukocytes and endogenously produced interleukin 8," *Mol Cell Biomech*, vol. 2, no. 3, pp. 145–159, 2005. 10

[41] M. J. Slattery, S. Liang, and C. Dong, "Distinct role of hydrodynamic shear in leukocyte-facilitated tumor cell extravasation," *Am J Physiol Cell Physiol*, vol. 288, pp. 831–839, 2005. 10

[42] S. Liang, M. J. Slattery, and C. Dong, "Shear stress and shear rate differentially affect the multi-step process of leukocyte-facilitated melanoma adhesion," *Exp Cell Res*, vol. 310, pp. 282–292, Nov 2005. 10

[43] C. Heyder, E. Gloria-Maercker, W. Hatzmann, K. S. Zaenker, and T. Dittmar, "Visualization of tumor cell extravasation," *Infection and Inflammation: Impacts on Oncogenesis. Contrib Microbiol.*, vol. 13, pp. 200–208, 2006. 11

[44] F. Kebers, J.-M. Lewalle, J. Desreux, C. Munaut, L. Devy, J.-M. Foidart, and A. Noël, "Induction of endothelial cell apoptosis by solid tumor cells," *Exp Cell Res*, vol. 240, pp. 197–205, 1998. 11

[45] E. Voura, M. Sandig, K. V. I, and C.-H. Siu, "Cell shape changes and cytoskeleton reorganization during transendothelial migration of human melanoma cells," *Cell Tissue Res*, vol. 293, pp. 375–387, Aug 1998. 11

[46] Y.-H. Li and C. Zhu, "A modified boyden chamber assay for tumor cell transendothelial migration *in vitro*," *Clin. Exp. Metastasis*, vol. 17, pp. 423–429, 1999. 11

[47] S. Hazgui, N. Bonnet, J. Cutrona, B. Nawrocki-Raby, L. Polette, Myriamand Chouchane, P. Birembaut, and J.-M. Zahm, "3d culture model and computer-assisted video microscopy to analyze migratory behavior of noninvasive and invasive bronchial epithelial cells," *Am J Physiol Cell Physiol*, vol. 289, pp. C1547–C1552, 2005. 11

[48] Z. N. Demou and L. V. McIntire, "Fully automated three-dimensional tracking of cancer cells in collagen gels: Determination of motility phenotypes at the cellular level," *Cancer Res*, vol. 62, pp. 5301–5307, 2002. 12

[49] R. Chotard-Ghodsnia, O. Haddad, A. Leyrat, A. Drochon, C. Verdier, and A. Duperray, "Morphological analysis of tumor cell/endothelial cell interactions under shear flow," *J Biomech*, vol. 40, no. 2, pp. 335–344, 2007. 12, 35, 126, 138, 148, 149

[50] C. Hart, M. Brown, S. Bagley, and N. Clarke, "Invasive characteristics of human prostatic epithelial cells: understanding the metastatic process," *Br. J. Cancer*, vol. 92, pp. 503–512, 2005. 12, 13, 148

[51] N. A. Pawlowski, G. Kaplan, E. Abraham, and Z. A. Cohn, "The selective binding and transmigration of monocytes through the junctional complexes of human endothelium," *J Exp Med*, vol. 168, pp. 1865–1882, 1988. 13

[52] E. Pokorna, P. W. Jordan, C. H. O'Neill, D. Zicha, C. S. Gilbert, and P. Vesely, "Actin cytoskeleton and motility in rat sarcoma cell populations with different

metastatic potential," *Cell Motil. Cytoskeleton*, vol. 28, no. 1, pp. 25–33, 1994. 13, 129

[53] F. J. Bueche, *Introduction to physics for scientists and engineers.* McGraw-Hill, Singapore, 1986. ISBN 0-07-066150-2, 621–646. 14

[54] F. J. Bueche, *Introduction to physics for scientists and engineers.* McGraw-Hill, Singapore, 1986. ISBN 0-07-066150-2, 647–689. 14

[55] D. A. Agard, Y. Hiraoka, P. Shaw, and J. W. Sedat, "Fluorescence microscopy in three dimensions," *Methods in Cell Biology*, no. 30, pp. 353–377, 1989. 14

[56] J. R. Swedlow and M. Platani, "Live cell imaging using wide-field microscopy and deconvolution," *Cell Struct Funct*, vol. 27, pp. 335–341, 2002. 14

[57] D. J. Stephens and V. J. Allan, "Light microscopy techniques for live cell imaging," *Science*, vol. 300, pp. 82–86, 2003. 14

[58] G. Sluder and D. E. Wolf, *Digital Microscopy.* Elsevier Science, 3rd ed., 2007. 14, 42

[59] J. G. McNally, T. Karpova, J. Cooper, and J. A. Conchello, "Three-dimensional imaging by deconvolution microscopy," *Methods*, vol. 19, pp. 373–385, 1999. 16, 124

[60] D. Taylor and Y. Wang, *Fluorescence Microscopy of Living Cells in Culture.* Academic Press, San Diego, California, 1989. ISBN 0-12-684755-x, kap.1. 17

[61] J.-A. Conchello and J. W. Lichtman, "Optical sectioning microscopy," *Nature Methods*, vol. 2, pp. 920–931, 2005. 20, 106

[62] G. J. Brakenhoff, E. A. Spronsen van, H. T. M. Voort van der, and N. Namminga, "Three-dimensional confocal fluorescence microscopy," *Methods in Cell Biol*, vol. 30, pp. 379–398, 1989. 21

[63] R. O. Duda, P. E. Hart, and D. G. Stork, *Pattern Classification.* The Atrium, Southern Gate, Chichester, West Sussex PO19 8SQ, UK: John Wiley & Sons, 2nd ed., 2001. 23

[64] J. A. Hartigan and M. A. Wong, "A k-means clustering algorithm," *Applied Statistics*, vol. 28, no. 1, pp. 100–108, 1979. 23

[65] R. A. Johnson and D. W. Wichern, *Applied multivariate statistical analysis.* Englewood Cliffs, NJ, 07932 USA: Prentice-Hall, 3rd ed., 1992. 24

[66] D. A. Langan, J. W. Modestino, and J. Zhang, "Cluster validation for unsupervised stochastic model-based image segmentation," *IEEE T Image Process*, vol. 7, no. 2, pp. 180–195, 1998. 25

[67] R. Wehrens, A. Simonetti, and L. Buydens, "Mixture modelling of medical magnetic resonance data," *J Chemometr*, vol. 16, pp. 274–282, 2002. 25

[68] R. Ferrari, R. Rangayyan, R. Borges, and A. Frre, "Segmentation of the fibroglandular disc in mammograms using gaussian mixture modelling," *Med Biol Eng Comput*, vol. 42, no. 3, pp. 378–387, 2004. 25

[69] M. Turk and A. Pentland, "Eigenfaces for recognition," *J Cog Neurosci*, vol. 3, no. 1, pp. 71–86, 1991. 26

[70] I. T. Jolliffe, *Principal Component Analysis.* 233 Spring St, New York, New York 10013, U.S.A.: Springer-Verlag, 2nd ed., 2002. 27

[71] P. Geladi, H. Isaksson, L. Lindqvist, S. Wold, and K. Esbensen, "Principal component analysis of multivariate images," *Chenmometrics and Intelligent Laboratory Systems*, vol. 5, pp. 209–220, 1989. 27

[72] A. Witkin, "Scale space filtering.," in *Proc. 8th Int. Joint Conf. on Artificial Intelligence (IJCAI83)*, pp. 1019–1021, Aug 1983. 29, 74, 75

[73] J. J. Koenderink, "The structure of images," *Biol Cybern*, vol. 50, pp. 363–370, Aug 1984. 29, 96

[74] T. Cavanna, E. Pokorna, P. Vesely, C. Gray, and D. Zicha, "Evidence for protein 4.1b acting as a metastasis suppressor," *J Cell Sci*, vol. 120, pp. 606–616, 2007. 52, 133

[75] D. Wright, "Getting to the bottom of it: Tools, techniques, and discoveries of deep ocean geography," *Professional Geographer*, vol. 51, no. 3, pp. 426–439, 1999. 52

[76] T. F. Cootes, C. J. Taylor, D. H. Cooper, and J. Graha, "Active shape models-their training and application," *Comput Vis Image Und*, vol. 61, no. 1, pp. 38–59, 1995. 61

[77] T. F. Cootes and C. J. Taylor, "Statistical models of appearance for medical image analysis and computer vision," in *SPIE Medical Imaging*, pp. 236–248, Jul 2001. 61

[78] C. V. Carman and T. A. Springer, "A transmigratory cup in leukocyte diapedesis both through individual vascular endothelial cells andbetween them," *Journal of Cell Biology*, vol. 167, no. 2, pp. 377–388, 2004. 61, 150

[79] W. A. Muller, "Leukocyte endothelial-cell interactions in leukocyte transmigration and the inflammatory response," *TRENDS in Immunology*, vol. 24, no. 6, pp. 326–333, 2003. 61

[80] S. Hägglund, A. Hoppe, D. Aubyn, T. Cavanna, P. Jordan, and D. Zicha, "Novel shear flow assay provides evidence for non-linear modulation of cancer invasion," *Front Biosci*, vol. 14, pp. 3085–3093, 2009. 61

[81] A. P. Dempster, M. Laird, and D. B. Rubin, "Maximum likelihood from incomplete data via the em algorithm," *Journal of the Royal Statistical Society Series B (Methodological)*, vol. 39, no. 1, pp. 1–38, 1977. 65

[82] J. S. Taur and C. W. Tao, "Medical image compression using principal component analysis," in *International Conference on Image Processing (ICIP 96)*, pp. 903–906, Sep 1996. 69

[83] J. J. Sychra, P. A. Bandettini, N. Bhattacharya, and Q. Lin, "Synthetic images by subspace transforms i. principal components images and related filters," *Med Phys*, vol. 21, no. 2, pp. 193–201, 1994. 69, 71

[84] E. Pedersen, M. Bergström, E. Bengtsson, and B. Långström, "Principal component analysis of dynamic positron emission tomography images," *Eur J Nucl Med*, vol. 21, no. 12, pp. 1285–1292, 1994. 71

[85] A. Nijssen, T. C. Bakker Schut, F. Heule, P. J. Caspers, D. P. Hayes, M. H. A. Neumann, and G. J. Puppels, "Discriminating basal cell carcinoma from its surrounding tissue by raman spectroscopy," *J Invest Dermatol*, vol. 119, no. 1, pp. 64–69, 2002. 71

[86] N. Bonnet, "Multivariate statistical methods for the analysis of microscope

image series: an application to material sciences," *J Microsc*, vol. 190, no. 1/2, pp. 2–18, 1998. 71

[87] T. Lehmann, C. Gonner, and K. Spitzer, "Survey: interpolation methods in medical image processing," *IEEE T Med Imaging*, vol. 18, pp. 1049–1075, Nov 1999. 79

[88] T. Lehmann, C. Gonner, and K. Spitzer, "Addendum: B-spline interpolation in medical image processing," *IEEE T Med Imaging*, vol. 20, no. 7, pp. 660–665, 2001. 79

[89] H. Hoppe, T. DeRose, T. Duchamp, J. McDonald, and W. Stuetzle, "Surface reconstruction from unorganized points," in *SIGGRAPH 92'*, (New York, NY, USA), pp. 71–78, ACM Press, 1992. 79

[90] T. S. Yoo, B. Morse, K. R. Subramanian, P. Rheingans, and M. J. Ackerman, "Anatomic modeling from unstructured samples using variational implicit surfaces," in *SIGGRAPH '05: ACM SIGGRAPH 2005 Courses*, (New York, NY, USA), p. 245, ACM, 2005. 79

[91] S. Ilic and P. Fua, "Implicit meshes for surface reconstruction," *IEEE T Pattern Anal*, vol. 28, no. 2, pp. 328–333, 2006. 80

[92] M. Bertalmio, G. Sapiro, V. Caselles, and C. Ballester, "Image inpainting," in *SIGGRAPH 2000*, (New Orleans, LA; USA), pp. 417–424, July 2000. 83, 85

[93] D. King, *The Commissar Vanishes.* Metropolitan Books, 1st ed., 1997. 83

[94] S. Walden, *The Ravished Image.* St Martins Pr, 1985. 83

[95] G. Emile-Male, *The Restorers Handbook of Easel Painting.* Van Nostrand Reinhold, 1976. 83

[96] G. Sapiro, "Image inpainting," *SIAM NEWS*, vol. 35, pp. –, May 2002. 84

[97] A. Criminisi, P. Prez, and K. Toyama, "Region filling and object removal by exemplar-based image inpainting," *IEEE T Image Process*, vol. 13, no. 9, pp. 1200–1212, 2004. 84, 86

[98] M. Bertalmio, L. Vese, G. Sapiro, and S. Osher, "Simultaneous structure and texture image inpainting," *IEEE T Image Process*, vol. 12, no. 8, pp. 882–889, 2003. 85

[99] L. Vese and S. Osher, "Modeling textures with total variation minimization and oscillating patterns in image processing," *Journal of Scientific Computing*, vol. 19, no. 1-3, pp. 553–572, 2003. 85

[100] K. A. Patwardhan, G. Sapiro, and M. Bertalmio, "Video inpainting of occluding and occluded objects," in *Image Processing, 2005. ICIP 2005. IEEE International Conference on*, pp. 69–72, Sep 2005. 85

[101] H. Q. Dinh, G. Turk, and G. Slabaugh, "Reconstructing surfaces by volumetric regularization using radial basis functions," *IEEE T Pattern Anal*, vol. 24, pp. 1358–1371, Oct 2002. 88

[102] Y. Ohtake, A. Belyaev, and H. P. Seidel, "A multi-scale approach to 3d scattered data interpolation with compactly supported basis functions," in *Shape Modeling International*, pp. 153–161, May 2003. 88

[103] J. C. Carr, R. K. Beatson, J. B. Cherrie, T. J. Mitchell, W. R. Fright, M. C., and T. R. Evans, "Reconstruction and representation of 3d objects with radial basis functions," in *SIGGRAPH '01: Proceedings of the 28th annual conference on*

Computer graphics and interactive techniques, (New York, NY, USA), pp. 67–76, ACM Press, 2001. 88

[104] B. Morse, T. Yoo, D. Chen, P. Rheingans, and K. Subramanian, "Interpolating implicit surfaces from scattered surface data using compactly supported radial basis functions," in *International Conference on Shape Modeling and Applications*, 2001. 88

[105] A. Chirokov, *Scattered Data Interpolation and Approximation using Radial Base Functions.* Matlab File Exchange, accessed 2008-08-20. 88, 91

[106] J. C. Carr, R. W. Fright, and R. K. Beatson, "Surface interpolation with radial basis functions for medical imaging," *IEEE Trans. Med. Imag.*, vol. 16, pp. 96–107, Feb 1997. 88, 90

[107] J. C. Carr, R. K. Beatson, B. C. McCallum, W. R. Fright, T. J. McLennan, and T. J. Mitchell, "Smooth surface reconstruction from noisy range data," in *GRAPHITE '03: Proceedings of the 1st international conference on Computer graphics and interactive techniques in Australasia and South East Asia*, (New York, NY, USA), pp. 119–126, ACM Press, 2003. 88

[108] M. D. Buhmann, *Radial Basis Functions: Theory and Implementations.* The Edinburgh Building, Cambridge, CB2 2RU, UK: Cambridge University Press, 2003. ISBN 0521633389. 88

[109] M. J. D. Powell, "The theory of radial basis function approximation in 1990," in *Advances in Numerical Analysis 2: Wavelets, Subdivision Algorithms and Radial Basis Functions*, (Great Clarendon Street, Oxford OX2 6DP, UK), pp. 105–210, Oxford University Press, 1992. 88

[110] X. Chen, X. Zhou, and S. T. C. Wong, "Automated segmentation, classification, and tracking of cancer cell nuclei in time-lapse microscopy," *IEEE T Bio-Med Eng*, vol. 53, no. 4, pp. 762–766, 2006. 92

[111] M.-O. Baradez, C. P. McGuckin, N. Forraz, R. Pettengell, and A. Hoppe, "Robust and automated unimodal histogram thresholding and potential applications," *Pattern Recognition*, vol. 37, pp. 1131–1148, Jun 2004. 96, 98

[112] J. J. Koenderink and A. van Doorn, "Dynamic shape," *Biol Cybern*, vol. 53, pp. 383–396, Apr 1986. 97

[113] D. L. Donoho and I. M. Johnstone, "Adapting to unknown smoothness via wavelet shrinkage," *J. Amer. Statistical Assoc.*, vol. 90, pp. 1200–1224, Dec 1995. 98

[114] L. Sigal and M. Black, "Humaneva: Synchronized video and motion capture dataset for evaluation of articulated human motion," Tech. Rep. CS-06-08, Brown University, 115 Waterman St, Providence, RI 02912, USA, 2006. 105

[115] G. Cinamon, V. Shinder, and R. Alon, "Shear forces promote lymphocyte migration across vascular endothelium bearing apical chemokines," *Nature Immunol*, vol. 2, no. 6, pp. 515–522, 2001. 128, 149, 150, 151

[116] G. M. Cooper, *The Cell: A molecular approach.* AMS Press, 2nd ed., 2000. 140

[117] G. V. Cinamon, V. Shinder, R. Shamri, and R. Alon, "Chemoattractant signals and beta2 integrin occupancy at apical endothelial contacts combine with shear stress signals to promote transendothelial neutrophil migration1," *J Immunol*, vol. 173, pp. 7282–729, 2004. 149, 150

[118] M. Coughlin and G. Schmid-Schönbein, "Pseudopod projection and cell spreading of passive leukocytes in response to fluid shear stress," *Biophys J*, vol. 87, pp. 2035–2042, 2004. 149

[119] B. Wojciak-Stothard and A. Ridley, "Shear stress-induced endothelial cell polarization is mediated by rho and rac but not cdc42 or pi 3-kinases," *Journal of Cell Biology*, vol. 161, no. 2, pp. 429–439, 2003. 149

[120] K. Lawler, E. Foran, G. O'Sullivan, A. Long, and D. Kenny, "Mobility and invasiveness of metastatic esophageal cancer are potentiated by shear stress in a rock- and ras-dependent manner," *Am J Physiol-Cell Ph*, vol. 291, pp. C668–C677, 2006. 149

[121] A. Bershadsky, N. Balaban, and B. Geiger, "Adhesion-dependent cell mechanosensitivity," *Annual Review of Cell and Developmental Biology*, vol. 19, pp. 677–695, 2003. 149

[122] E. Krepela, P. Vesely, A. Chaloupkova, D. Zicha, P. Urbanec, R. D, and J. Vicar, "Cathepsin b in cells of two rat sarcomas with different rates of spontaneous metastasis," *Neoplasma*, vol. 36, no. 5, pp. 529–540, 1989. 149

[123] C. A. Hart, L. J. Scott, S. Bagley, A. Bryden, N. W. Clarke, and S. H. Lang, "Role of proteolytic enzymes in human prostate bone metastasis formation: in vivo and in vitro studies," *Br J Cancer*, vol. 86, pp. 1136–1142, 2002. 149

[124] K. Wolf, I. Mazo, H. Leung, K. Engelke, U. von Andrian, E. Deryugina, A. Strongin, E.-B. Bröcker, and P. Friedl, "Compensation mechanism in tumor cell migration: mesenchymalamoeboid transition after blocking of pericellular proteolysis," *J Cell Biol*, vol. 160, no. 2, pp. 267–277, 2003. 149

[125] R. Viley, *Cancer Metastasis: From mechanisms to therapy*, pp. 47–70. John Wiley, 1995. 150

[126] K. Schlüter, P. Gassmann, A. Enns, T. Korb, A. Hemping-Bovenkerk, J. Hölzen, and J. Haier, "Organ-specific metastatic tumor cell adhesion and extravasation of colon carcinoma cells with different metastatic potential," *American Journal of Pathology*, vol. 169, pp. 1064–1073, 2006. 150

[127] J. Millan, L. Hewlett, M. Glyn, D. Toomre, P. Clark, and A. Ridley, "Lymphocyte transcellular migration occurs through recruitment of endothelial icam-1 to caveola- and f-actin-rich domains," *Nature Cell Biology*, vol. 8, no. 2, pp. 113–123, 2006. 150

[128] G. Cinamon and R. Alon, "A real time *in vitro* assay for studying leukocyte transendothelial migration under physiological flow conditions," *J. Immunol. Methods*, vol. 273, pp. 53–62, Feb 2003. 150